A MULTI-ANATOMICAL RETINAL STRUCTURE SEGMENTATION SYSTEM FOR AUTOMATIC EYE SCREENING USING MORPHOLOGICAL ADAPTIVE FUZZY THRESHOLDING

Jasem Almotiri

Under the Supervision of Dr. Khaled Elleithy

DISSERTATION
SUBMITTED IN PARTIAL FULFILMENT OF THE REQUIREMENTS

FOR THE DEGREE OF DOCTOR OF PHILOSOPHY IN COMPUTER SCIENCE

AND ENGINEERING

THE SCHOOL OF ENGINEERING

UNIVERSITY OF BRIDGEPORT

CONNECTICUT

SEPTEMBER, 2018

A MULTI-ANATOMICAL RETINAL STRUCTURE SEGMENTATION SYSTEM FOR AUTOMATIC EYE SCREENING USING MORPHOLOGICAL ADAPTIVE FUZZY THRESHOLDING

Jasem Almotiri

Under the Supervision of Dr. Khaled Elleithy

Approvals

Committee Members

Name	Signature	Date
Supervising: Dr. Khaled Elleithy		10/5/18
Member 2: Dr. Miad Faezipour		10-5-2018
Member 3: Dr. Navarun Gupta		10/5/18
Member 4: Dr. Xingguo Xiong		10/05/2018
External Examiner: Dr. Syed Rizvi		10/08/2018.

Ph.D. Program Coordinator

Dr. Khaled M. Elleithy — 10/5/2018

Chairman, Computer Science and Engineering Department

Dr. Ausif Mahmood — 10-5-2018

Dean, School of Engineering

Dr. Tarek M. Sobh — 10-5-2018

A MULTI-ANATOMICAL RETINAL STRUCTURE SEGMENTATION SYSTEM FOR AUTOMATIC EYE SCREENING USING MORPHOLOGICAL ADAPTIVE FUZZY THRESHOLDING

A MULTI-ANATOMICAL RETINAL STRUCTURE SEGMENTATION SYSTEM FOR AUTOMATIC EYE SCREENING USING MORPHOLOGICAL ADAPTIVE FUZZY THRESHOLDING

ABSTRACT

Eye exam can be as efficacious as physical one in determining health concerns. Retina screening can be the very first clue to detecting a variety of hidden health issues including pre-diabetes and diabetes. Through the process of clinical diagnosis and prognosis; ophthalmologists rely heavily on the binary segmented version of retina fundus image; where the accuracy of segmented vessels, optic disc and abnormal lesions extremely affects the diagnosis accuracy which in turn affect the subsequent clinical treatment steps. This thesis proposes an automated retinal fundus image segmentation system composed of three segmentation subsystems follow same core segmentation algorithm. Despite of broad difference in features and characteristics; retinal vessels, optic disc and exudate lesions are extracted by each subsystem without the need for texture analysis or synthesis. For sake of compact diagnosis and complete clinical insight, our proposed system can detect these anatomical structures in one session with high accuracy even in pathological retina images.

The proposed system uses a robust hybrid segmentation algorithm combines adaptive fuzzy thresholding and mathematical morphology. The proposed system is validated using four benchmark datasets: DRIVE and STARE (vessels), DRISHTI-GS (optic disc), and DIARETDB1 (exudates lesions). Competitive segmentation performance is achieved, outperforming a variety of up-to-date systems and demonstrating the capacity to deal with other heterogenous anatomical structures.

AKNOWLEDGEMENT

At First, I would never have been able to finish my dissertation without the guidance and help of my God, I began this journey in his name and I have finished this thesis in his name: *Lord of Mercy …The Giver of Mercy*.

I would like to express my sincere gratitude to my supervisor Prof Khaled Elleithy for his patience, knowledge, advice, comments, valuable time and for his continuous support along my Ph.D. study. I could not have imagined having a better advisor and mentor for my Ph.D. study. I would not be able to finish this work without his advice and support.

I also would like to thank my committee, Dr. Miad Faezipour, Dr. Navarun Gupta, Dr. Xingguo Xiong and Dr. Syed Rizvi for their deep feedback in our committee meetings and the comments that help enhance this thesis.

Finally, I would like to thank my father, mother, family and friends for their constant love and support, their encouraging to strive for the best.

TABLE OF CONTENTS

LIST OF TABLES

LIST OF FIGURES

CHAPTER 1: INTRODUCTION

1.1 Introduction

Although the retina resides in a peripheral location, it is a part of the central nervous system, representing the neural portion of the eye [1]. The morphological variation in retinal anatomical structures is of great diagnostic value since it contains crucial information for the detection and diagnosis of a variety of retinal pathology such as Diabetic Retinopathy (DR), glaucoma, hypertension, Age-related Macular Degeneration (AMD), and Retinopathy of Prematurity (RoP) and for diagnosis of heart- and brain-related diseases. One of the major diseases that can hit the health of eye in particular and the overall health in general, the diabetes.

Diabetic retinopathy is one of the most common causes of vision loss among people of working age. Diabetes can cause various abnormalities including diabetic retinopathy if it affects retina, nephropathy if affect kidneys and diabetic neuropathy if it affects the nervous system. Moreover, diabetes is considered a critical risk factor in diseases related to heart and blood vessels [2].

Approximately half of blindness cases can be prevented through early diagnosis and periodic retinal screening. These diseases represent leading sources of retina-associated vision impairment and blindness in the United States of America Retinal screening is a way of detecting diabetic retinopathy early before any changes to your vision are noticed [3]. In early stages of diabetic retinopathy, no radical symptoms can be noted, however, over the time, many symptoms begin to appear and its severity increased

monastically with time [4].Typically, diabetic retinopathy begins as a small change in retinal blood vessels; thus, the first abnormality can be detected is the existence of Microaneuryms. Then, it affects the optic disc (optic nerve head) leading to changes in the optic disc shape. Further diabetes complication of diabetic retinopathy development is the increasing of vessels' walls permeability of the retinal which allows leaking of lipid formations through weak wall of blood vessels leading to Hard Exudates. If retinopathy is detected early enough, treatment can cease it getting worse. Otherwise, symptoms become noticeable with time passing, besides, it can be much more difficult to treat [2].

Retinal screening performed through imaging instruments such as fundus camera, scanning laser ophthalmoscope (SLO) [5], where the ophthalmologists use both the 2D retinal yielded image and the segmented version of it in the process of diagnosis of pre-diabetes, diabetic retinopathy, and other health concerns that may be deduced. Retinal image segmentation is challenging; the normal and abnormal retinal anatomical structures has low contrast with their background, including vascular structures, the macula, and Microaneuryms. In contrast, other structures have high contrast with background tissues but are difficult to distinguish from challenges make classical segmentation techniques such as Sobel operators [6], Prewitt operators [7], gradient operators [8], and Robert and Krish differential operations [9] inefficient and inaccurate.

1.2 Motivations

Although segmentation via these methods has been shown to be superior to other available methods, it is incapable of detecting and extracting all anatomical structures in one system; rather, to be fully identified and segmented; each anatomical structure

requires a separate stand-alone system built on a stand-alone algorithm. Another disadvantage of previously reported schemes consists of their incapability to address retinal images containing pathologies; this inability is demonstrated by performance degradation in terms of false positive rates and reduced accuracy, chiefly due to the presence of abnormal structures such as hemorrhages, exudates, and other lesions. Identification and extraction of multiple anatomical structures in retinal fundus images is thus a complicated problem and a potential minefield. These limitations have motivated us to develop a system that can extract multiple retinal anatomical structures at one session with high accuracy without the need for texture analysis or synthesis. This research exploits and combines fuzzy sets, mathematical morphology theories, and their capability for fast, accurate segmentation system.

1.3 Contributions

From a research point of view, our work makes two major contributions. First, our proposed system eliminates the need for designing a separate system for detecting each retinal anatomical structure; one compact novel system was used to extract three different anatomical structures with various features and textures. Building upon this system, a hybrid framework for performing detection and extraction tasks for other anatomical structures either inside the retina or other organs can be developed. Second, the proposed system is highly robust and accurate as well, as it has been shown to perform better than the state-of-art on the public DRIVE, STARE, DRITSHTI-GS, and DiaRetDB1 retinal datasets.

In addition, it performs well at extracting vessels and optic disc from pathological retinal images. Therefore, it can be considered ideal for real-life diagnosis applications.

1.4 Thesis Outline

In this thesis, a novel technique is proposed to improve segmentation performance of retinal anatomical structures in *noisy* conditions, and will be discussed in the upcoming chapters as follows.

Chapter 2 reviews the existing literature related to the research work presented in this thesis. In Chapter 3, we propose our hybrid retinal segmentation system and describes the different phases of the proposed hybrid system. Chapter 4 evaluates and discuss the system results and compares them with other techniques and methods. Finally, Section Chapter 5 summarizes the conclusions and recommendations and proposed future directions of this work.

CHAPTER 2: BACKGROUND THEORY

The identification and localization of different retinal anatomical structures aim to separate the different retinal vasculature structure tissues either normal or abnormal from the fundus image background. Identification studies are attracting more and more attention in recent years due to non-invasive fundus imaging and the crucial information contained in the anatomical structures of retina; which is helpful for the detection and diagnosis of a variety of retinal pathologies included but not limited to: Diabetic Retinopathy (DR), glaucoma, hypertension, and Age-related Macular Degeneration (AMD). With the development of almost two decades, the innovative approaches applying computer-aided techniques for segmenting retinal anatomical structures are becoming more and more crucial and coming closer to routine clinical applications. In this chapter, a brief introduction to retinal fundus photography and imaging modalities of retinal images is given. Then, the preprocessing operations and the state-of-the-art methods of anatomical retinal identification are introduced along with an objective assessment and future developments and trends.

2.1 Retinal Structures Anatomy

As shown in Figure 2.1 Retinal fundus image: 2D and 3D view.

Figure 2.1, the fundus of the human eye is the back portion of the interior of the eye ball. The optic nerve resides at the center of retina, which can be seen as a white area of circular to oval shape and measuring about 3×3 mm across diameter. The major

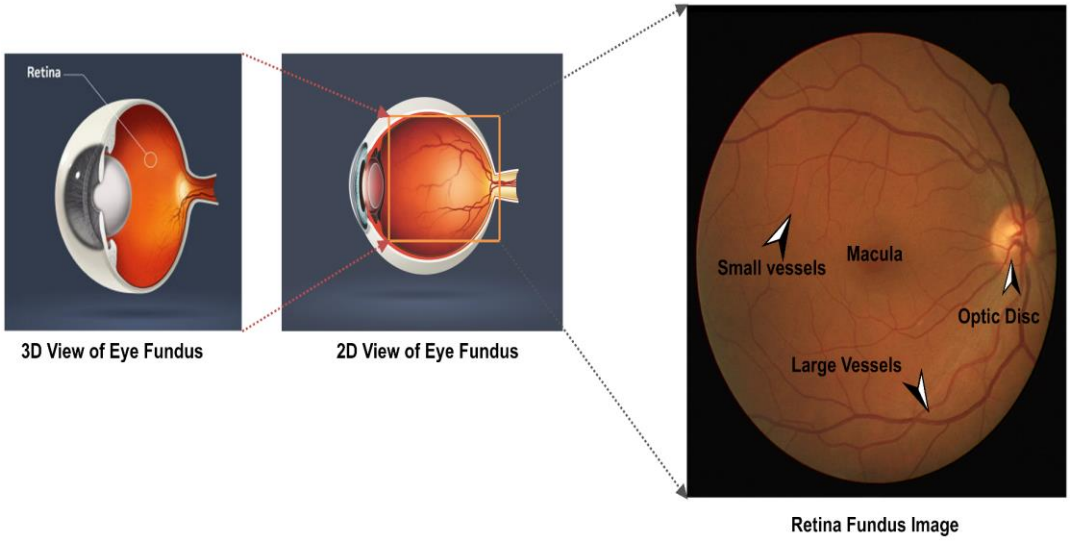

Figure 2.1 Retinal fundus image: 2D and 3D view.

blood vessels of the retina radiate from the center of the area of optic nerve and then radiate and branched to fill the entire area excepting the fovea zone, which is a blood-vessel free reddish spot with an oval-shaped lies to the left of the optic disc directly and it resides the center of an area that is known by the ophthalmologists as the "macula" region [10].

The optic disc as defined by [11] is "The optic disc is shaped like a doughnut with a pink neuroretina rim and a central white depression called the physiologic cup where further details related to optic disc anatomy was discussed thoroughly in *chapter 3*.

One of the major diseases that can hit the health of eye in particular and the overall health in general, the diabetes. Diabetes can cause various abnormalities including

diabetic retinopathy if it affects retina and it affect kidneys and, in this case, it called diabetic nephropathy, or even it affects the nervous system, where it called diabetic neuropathy. Moreover, diabetes is considered a critical risk factor in diseases related to heart and blood vessels [12].

The diabetic retinopathy is considered one of the microvascular complications that associated with diabetes, leading to abnormalities manifest in retina in subsequent way with respect to time, where it may lead in worst case to complete blindness.

Many changes occurred and developed in the retinal anatomical structures due to diabetes; majorly can be categorized into five major types: (1) Microaneuryms, (2) Hemorrhages (3) Hard Exudates (4) Soft Exudates (5) Neovascularization.

In early stages of diabetic retinopathy, no radical symptoms can be noted, however, over the time, many symptoms begin to appear and its severity situation increased monastically with time. Typically, diabetic retinopathy begins as a small change in retinal blood vessels; thus, the first abnormality can be detected is the existence of *Microaneuryms.*

Microaneuryms are defined as local distensions of retinal vessels which, in turn, leads to intraretinally *Hemorrhage*. When it exploded, then, the severity of diabetic retinopathy is classified as mild non-proliferative state.

The next stage of diabetic retinopathy development is the permeability increasing of the retinal vessels' walls which allows leaking of lipid formations through weak wall of blood vessels leading to *Hard Exudates* (or He and the severity of this state is described as moderate non-proliferative retinopathy, and if it appeared in the macula region it is called maculopathy.

As time proceeds, the retinopathy advances, some of blood vessels become almost blocked leading to microinfarcts in retina. This situation is categorized as *Soft Exudates***.** When a considerable number of hemorrhages, hard excaudate and soft exudates are created, the severity of retinopathy is described as sever nonperformative diabetic retinopathy, then this state of severity can turn into proliferative diabetic retinopathy as an appreciable lack of oxygen lead to creation of new fragile vessels. This situation is known as neovascularization, which in turn can leads to permanent blindness [2, 13] All these severity situations development versus time is depicted and summarized in Figure 2.2.

In this thesis, we deal with retinal vessels, optic disc, and hard exudates as target anatomical structures for our proposed segmentation system.

2.2 Retinal Fundus Imaging

Retina photography is typically conducted via an optical apparatus called fundus camera as shown in Figure 2.3. Fundus camera can be viewed as a low power microscope that specialized in retina fundus imaging, where the retina is illuminated and imaged via the attached camera. In particular, fundus camera is designed to capture an image for the interior surface of human eye which composed of major parts including: macula, optic disk, retina and posterior pole [14].

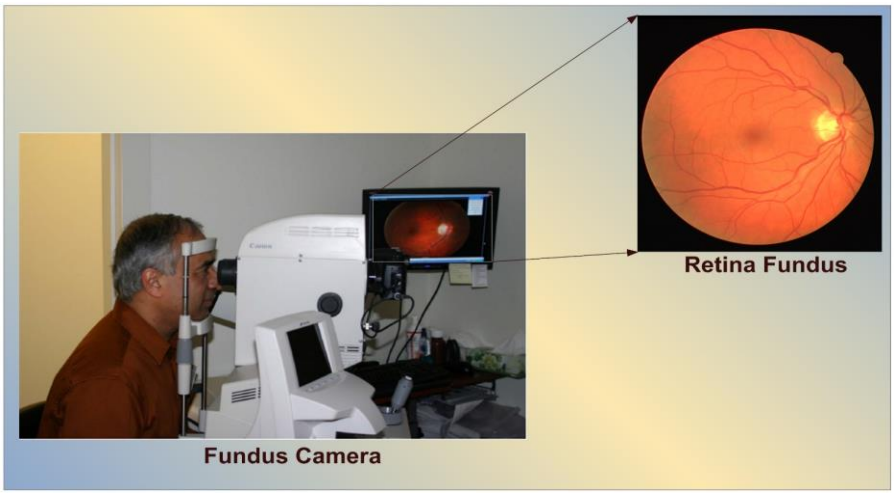

Figure 2.3 Retinal fundus camera.

Fundus photography can be viewed as a sort of documentation process for the retinal interior structure and retinal neurosensory tissues. The retinal neurosensory tissues convert the optical images reflection, that we see, into electrical signals in form of pulses sent to our brain where it decoded and understood. Retina photography can be conducted based on the idea that the eye pupil is utilized as both an entrance and exit for the illuminating and imaging light rays that used by the fundus camera. During the fundus photography, patients' foreheads are placed against the bar and their chins placed in the chin rest as shown in Figure 2.3. After the oculist aligns the fundus camera, the camera shutter is released so a flash light is fired and a two-dimensional picture for retina fundus has been taken [15] as anatomically illustrated in Figure 2.4.

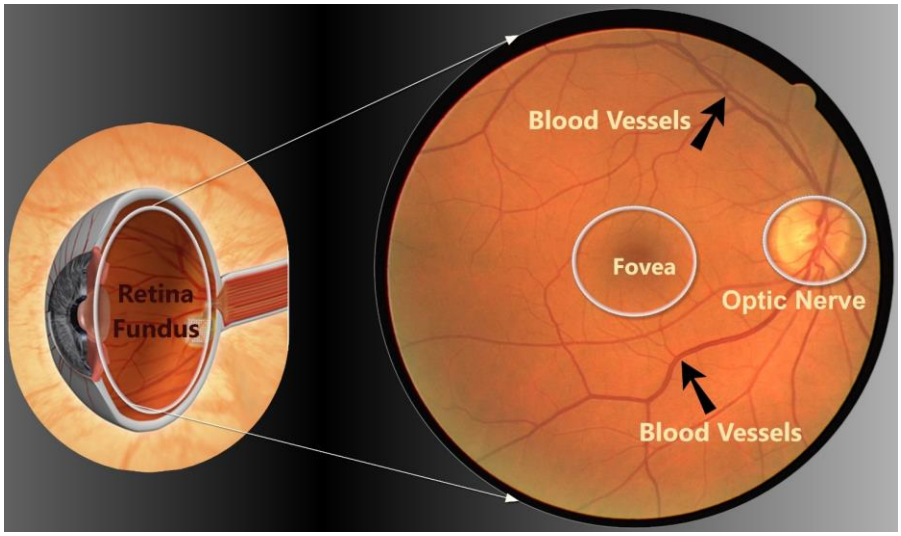

Figure 2.5 Retina fundus as seen through fundus camera.

In General, the photographic process involves grasping the light that reflected off the subject under consideration. In our case, the subject is the fundus of retina. Since the internal room of the eye has no light source of its own, in the retina photography, we need to flash or shine a light into eye room in order to capture a good photograph. The ocular fundus imaging has three major photography modes as elaborated in Figure 2.5:

- Full-color Imaging.
- Monochromatic (Filtered) Imaging.
- Fluorescence Angiogram.

In case of full-color photography mode, no light-filtration is used and it is totally non-invasive in contrary to other modes of fundus imaging. The resultant retina fundus image looks as two-dimensional full color image as illustrated in Figure 2.5.a. On the other hand, if the fundus is imaged via a monochromatic filter or via particular colored illumination; then the fundus photography is called "monochromatic" as shown in Figure 2.5.b.

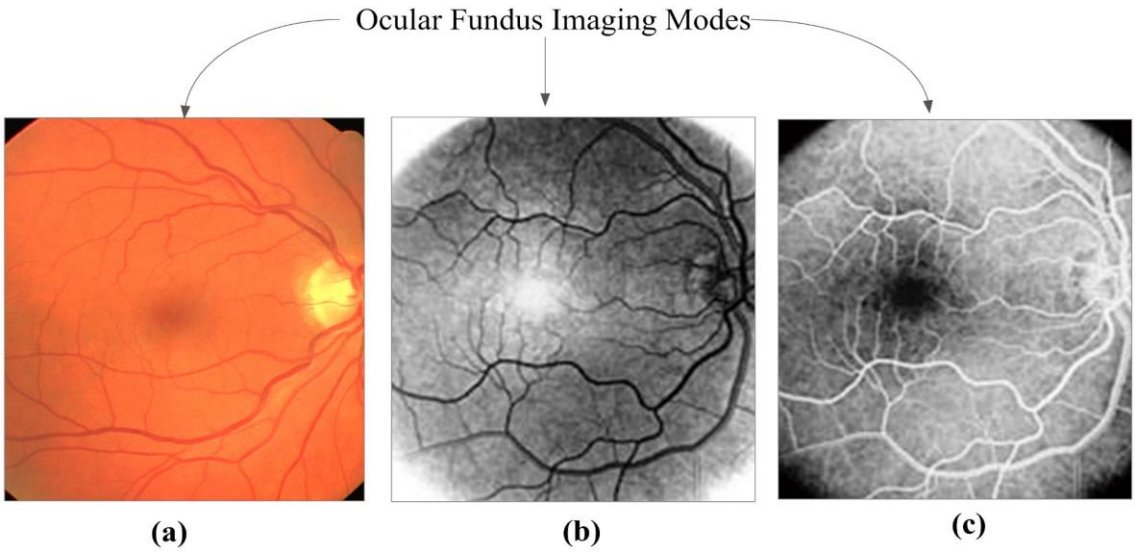

Figure 2.7 Imaging modes of ocular fundus photography. (a) Full color retinal fundus image (b) Monochromatic (filtered) retinal fundus image. (c) Fluorescence angiogram retinal fundus image.

This type of fundus photography is built based on the idea that the visibility of different structures in a retinal image is enhanced if the spectral range of illumination is changed correspondingly. In another word, instead of using white light of a broad scale of wavelengths, we use a light of a specified wavelength that corresponding to a specific color, for example, a red object in an image would appear lighter if the image is taken through a red filter and it would appear darker if it is taken through green filter.

As the white light can be divided into red, green and blue lights, the ocular fundus can be photographed via one of these gradient lights where each light has the capability to enhance the visibility of specific retinal anatomical structures based on their colors. For example, blue filter (filter with blue light) enhances the visibility of the interior layers of retina, which in full-color photo (taken by white light) appears almost transparent. On the other hand, we can get the best overall view of retina fundus and the most enhanced contrast if we used the green filter. Moreover, green filters have the capability to enhance the visibility of common lesions such as exudates, hemorrhage and drusen.

Another alternative to monochromatic filters is to split the full-color fundus image into its basic components, namely, Red, Green and Blue. It equally operates as colored filters, except we lose the resolution, which represents a way adopted in a variety of retinal vessel identification approaches in the stage of image preprocessing framework [16].

Fundus angiography is the most invasive fundus imaging where it involves injecting a tiny amount of fluorescein dye into a vein of patient's arm, then the dye takes its way towards main blood stream leads it to retina vessels; then, the retina fundus is photographed. Originally, the word "angiography" is derived from the Greek words: Angeion which means "vessels" and "graphien" which means to record or to write. Once the sodium-fluorescein has been injected, and reached retina; retina fundus is illuminated with a blue light, then it is flashed in a yellow-green color. Later, specialized filters in the fundus camera allow the fluorescent light to be imaged leading to a high contrast (gray-scaled) retinal vascular structure images as shown in Figure 2.5.c [17].

Retina angiography is considered the photography mode that highly revolutionized the ophthalmologists' capabilities in understanding both of retina physiology and pathology. Moreover, it used in the process of diagnosing, treatment of choroidal diseases [17]. However, this mode is considered the most invasive one among other, due to injecting dyes in the human veins directly. Thus, as recently reported in, it is important to consider the potential risk associated with using such mode of retina fundus photography especially for neonatal people [18].

2.3 Retinal Image Processing

The oculists scan the retina of patients using fundus camera with high resolution. Accordingly, the situation of retina blood vessels, optic disc and possible existing abnormal anatomies are probed in order to diagnose the retinal diseases.

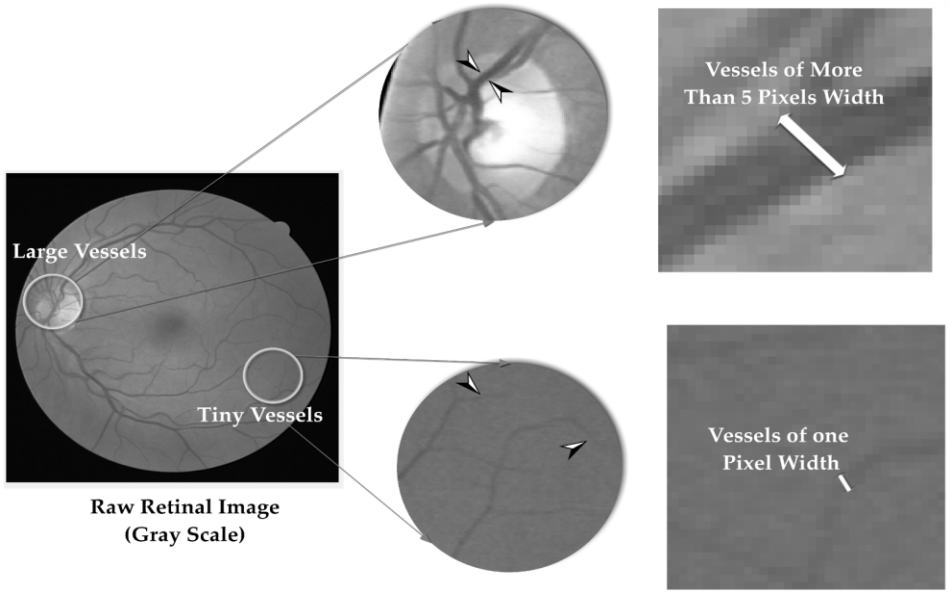

Figure 2.9 Pixel width variation of retinal vessels (in pixels).

In many cases, it is found that the retinal vascular structure has low contrast with regard to their background in contrary to optic disc and exudates abnormalities. In other cases, optic disc and exudates may have same appearance on the surface of retina image. Moreover, Retina vessel identification and extraction faces many challenges that may be outlined as follows: (1) The retinal vessels' widths take a wide range of color intensity range from less than one pixel up to more than five pixels in the retinal image, as shown in Figure 2.6, which requires an identification technique with high flexibility.

For further elaboration to this challenge, a snippet of MATLAB® code has been developed for sake of grey levels substitution in retinal image; the different gray levels of a raw retinal image have been replaced by color ones, as shown in Figure 2.7.

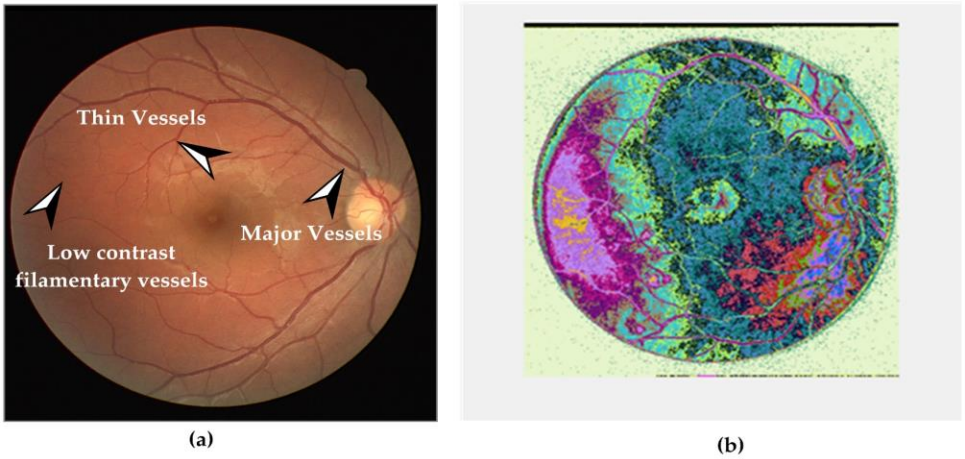

Figure 2.11 First challenge of retinal image segmentation. (a) Description of what is contained in the first panel. (b) Different sizes of retinal vessels.

It can be noted that many of retinal vessels, either large or tiny ones, take the same background color intensities. This reveal the broad range of color that may be taken by the retinal vasculature structure making the identification process more complicated rather than that found in other identification problems.

This challenge opens the room for a field of research specialized in detecting and segmenting thin (filamentary) retinal vascular structures as in [19-26]. (2) Vessels identification in pathological retinal images faces a tension between accurate vascular structure extraction and false responses near pathologies (such as hard and soft Exudates, Hemorrhages, Microaneuryms and cotton wool Spots) and other nonvascular structures (such as Optic disc and Fovea region). The retinal blood vasculature is a tree-like structure disperses across the fundus image surface including pathologies. Thin and filamentary retinal vessels melt in the retinal abnormal regions burden the task of accurate vessel segmentation as shown in Figure 2.8.

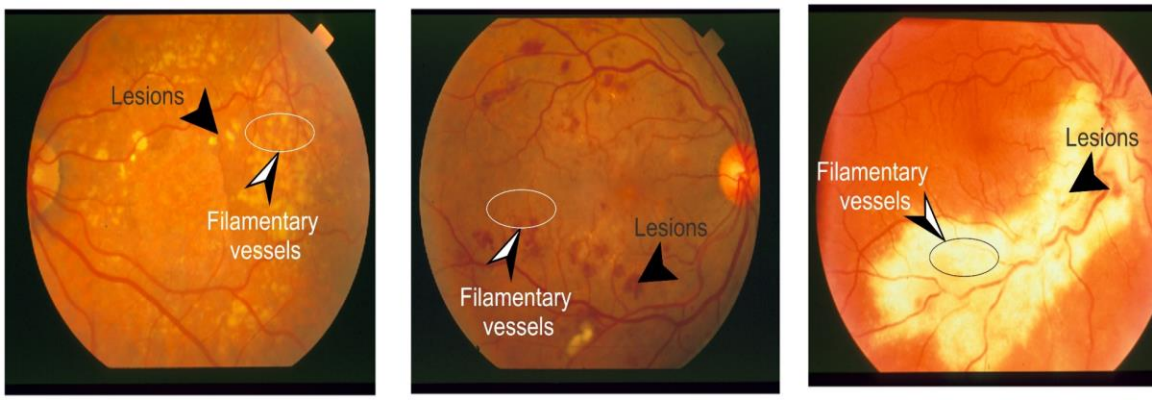

Figure 2.13 Effect of retinal lesions on filamentary vessel structures appearance.

In summary, retinal vascular structure, either, inside normal or abnormal retina images has low contrast with respect to the retinal background. Whereas, other retinal anatomical structures have high contrast to other background tissues but with indistinct features in comparison with abnormal structures; optic disc and exudates lesions represent typical examples.

All these challenges, in terms of medical image processing, make the classical segmentation techniques such as Sobel operators[6], Prewitt operators[7], gradient operators[8], Robert and Krish differential operations [9] inefficient and inaccurate. As a consequence, a variety of algorithms and methodologies have been developed and implemented for sake of automatic identification, localization and extraction of retinal anatomical structures and can be broadly divided into: Rule-based and Machine learning techniques as elaborated as shown in Figure 2.9 and elaborated in subsequent sections.

In general, the capability of retinal segmentation algorithm to extract different retinal anatomical structures is evaluated in terms of many metrics. The most common ones are: average True Positive Rate (TPR), average False Positive Rate (FPR), average Sensitivity (recall, TPR), average Specificity(1-FPR), average Accuracy, average Precision. Sensitivity and specificity represent the most widely used metrics in medical researches; the higher the specificity and sensitivity values, the better diagnosis. The sensitivity reflects the capability of the algorithm to detect the vessels' pixels whereas the specificity determines the ability of the algorithm to detect non-vessel pixels.

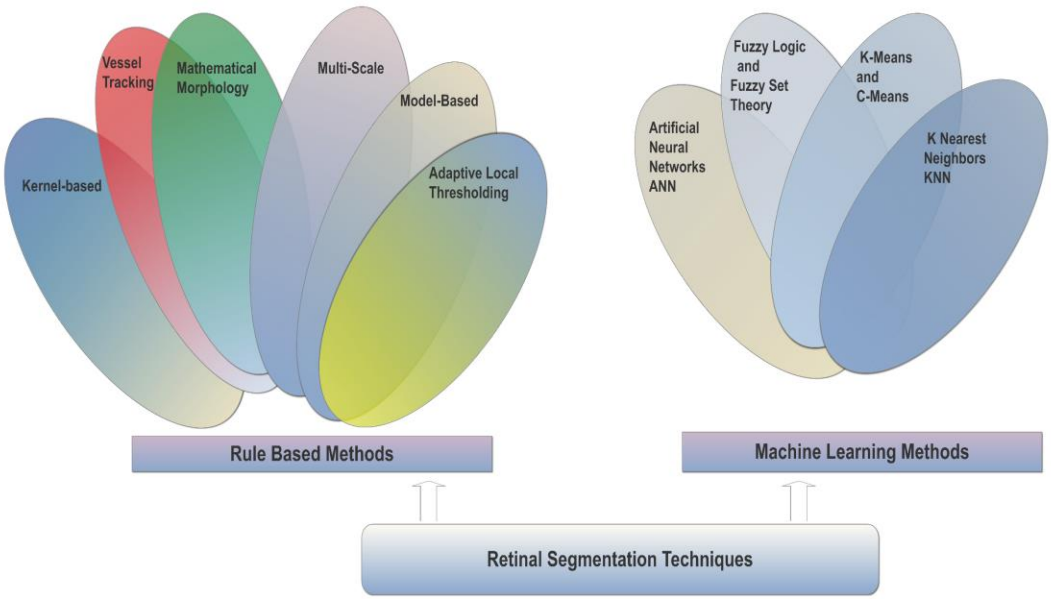

Figure 2.15 Retinal segmentation techniques.

Sensitivity and Specificity represent the features of the algorithm and they associated with the accuracy metric in many medical image processing fields including retinal vessel segmentation [27] as given by the following equations [28] (2.1(2.4) :

$$\text{Sensitivity(Recall)} = TP/(TP + FN) \quad (2.1)$$

$$\text{Specificity} = TN/(TN + FP) \quad (2.2)$$

$$\text{Accuracy} = (TP + TN)/(TP + FN + FP + TN) \quad (2.3)$$

$$\text{Precision} = TP/(TP + FP) \quad (2.4)$$

Where TP (True Positives), FP (False Positives), FN (False Negatives), and TN (True Negatives).

On the other hand, many papers use the area under the Receiver Operating Characteristic (ROC) curve [29, 30] in order to evaluate their works especially for methods that highly depend on specific parameters during the segmentation execution. ROC curve is a non-linear function between TPR and FPR values. Optimal area under ROC is 1 for an optimal performance.

Most of retinal vessels segmentation techniques and algorithms used the most popular datasets in this field: (1) Digital Retinal Image for Vessel Extraction (DRIVE) [31, 32] and (2)Structuring Analysis of the Retina (STARE) [33]. Both datasets are well-considered and popular in the field of retinal vessels segmentation to the extent that almost every research performance involves vessels segmentation is evaluated via these datasets. The popularity of these datasets is due to the good resolution of the retinal fundus images and to the availability of manually labelled ground truth images prepared by two experts.

The DRIVE dataset consists of 40 retinal images were evenly divided into a training set and a test set whereas the STARE dataset consists of 20 images, 10 of which are normal retinal images and the other 10 images are abnormal ones. Nevertheless, many researchers use other datasets less common in contract to DRIVE and STARE datasets,

for sake of validation and performance evaluation, such as: Automated Retinal Image Analyzer (ARIA) dataset [34], DIAbietes RETina Data Base (DIARETDB) dataset [27], Methods for Evaluating Segmentation and Indexing techniques Dedicated to Retinal (Messidor) dataset [35, 36], High Resolution Fundus (HRF) [37].

2.4 Kernel-based Techniques

This type of retinal vessels segmentation depends on the intensities distribution of vessel pixels in order to build a filter kernel, which in turn, can detect the retinal vasculature structure boundaries. The kernel can either follows a pre-specified form based on the cross-section profile of retinal vessel, or it can be deformable according to vessels boundaries especially when they lie in or in neighbor of hemorrhages, Microaneuryms lesions. Most often, kernel-based approaches are used as preprocessing image enhancement step for other retinal vessels segmentation methodologies, since it enhances the map for vessels boundaries.

The profile-based kernels use one of varieties of models that have been proposed and implemented in retinal vessels profiling that built based on the idea that intensity distribution of retinal vessel is capable to describe retinal vessels characteristics which can be turn into maps for sake of vessels detection. The basic idea of kernel-based techniques (*or as called matched filtering-based*) techniques is to compare the pixels' intensity variations along with the cross-section profile of the retinal vessel with a prefigured template works as a kernel. Therefore, most of typical matched filter-based techniques detect retinal vessels by applying a matched filter kernel on the original gray retinal image followed by a thresholding step.

Retinal vessel profiling has many applications in the fields of vascular width measurement [38] or in the field of vessels type classification [39]. In case of vessels detection and extraction, it used to create the map for process of detection which pave the way for vessels extraction through region growing or filtering based approaches. Generally speaking, retinal vascular matched kernels can fall in one of two major categories : Gaussian-shaped or non-Gaussian shaped [40].

Early work in this direction was performed by Chaudhuri *et al.*[41] who observed the high similarity of the intensity variations of the cross-section profile of the retinal image with a Gaussian function as illustrated in Figure 2.10 Cross-section intensity profile of the region marked by a straight line between point A and point B on retina image.

Since first time when Chaudhuri et al. [41] published his well-known paper which stated that the cross section profile of retinal vascular structure has approximate Gaussian shape. Hence matched filters with Gaussian kernels are emerged and reported in literature later on for purpose of retinal vessel tree detection.

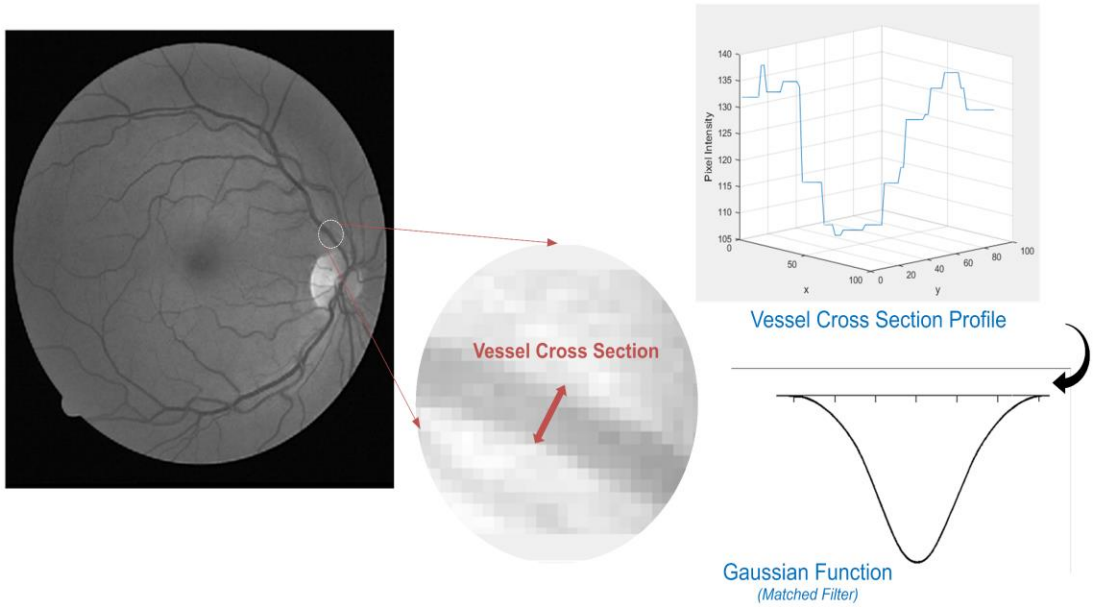

Figure 2.17 Cross-section intensity profile of the region marked by a straight line between point A and point B on retina image.

According to the fact that the cross section of retinal vessels can be modeled as a Gaussian function, a series of Gaussian shaped filters (different in Gaussian parameters values μ and σ) can be used in order to match different vessel sizes simply and efficiently. However, matched filters have strong response to both: vessels and non-vessels structures like red lesions and bright blobs which result in degradation in the performance in terms of false detection rate.

Three important aspects should be taken into consideration through designing a matched filter kernel: (1) limited curvature of retina vascular structure; where the curvature of vessel segments can be approximated by bell-shape piecewise linear segments. (2) vessels' width: the width of the retinal vessels decreases in gradual way when one makes a move from optical disk towards Fovea region as shown in Figure 2.4 (3) Accurate cross-section profile of pixel intensities distribution of the retinal blood vessels [42].

The same idea of Chaudhuri *et al.* [41] was followed and re-implemented by [43] via DRIVE dataset. The regenerated segmentation results have reported an average accuracy of 0.9387 and 0.9647 and 0.6721 for average specificity and average sensitivity respectively. Zhu and Schaefer [44] proposed a profile kernel-based algorithm for retinal vessel extraction based on profiling the cross-section of retinal vessels using piece-wise Gaussian scaled model. Once the profile has been modeled, a phase alignment function based on data obtained from oriented log-Gabor wavelet was applied. After boundary areas map of retinal vascular structure has been produced, cross-sections were extracted by following an approach was proposed by same author in [45].

A notable vessel extraction performance has been achieved by Villalobos-Castaldi *et al.* [46], where matched filter in a conjugation with entropy-based adaptive thresholding algorithm was employed. The methodology was applied on DRIVE dataset where it used matched filter in sake of piecewise linear segments enhancement of the retina vascular structure. Later, a co-occurrence matrix [47] that record the number of transitions between all pairs of gray-retinal levels was captured where the gray-level changes were depicted. Then, the entropy of the image gray levels distribution was exploited through second-entropy thresholding in order to segment the background pixels from the foreground (vessels) ones. The time consumed in the process of obtaining vascular structures approximated 3 seconds besides the high detection accuracy that has been achieved where it reached up to 0.9759, sensitivity and specificity of 0.9648 and 0.9480 respectively.

In comparing to performance that achieved in [46], Chanwimaluang and Fan [48] followed same procedure that was proposed in [46] in order to extract both : retinal vessel as well as the optic disk using STARE dataset. However, the time that consumed approximates 2.5 minutes per each retina image; most of it was consumed in matched filtering and local entropy thresholding steps. Moreover, it required post-processing steps were not required by [46] including long filtering stages for sake of isolated pixels removal. Then, filtering steps were followed by morphological thinning used to identify the retinal vascular intersection/crossovers. In the other hand, the optic disk identification proceeded into two major stages: (1) optic disk center identification through maximum local variance detection. (2) optic disk boundary identification through snake active contour. Even though the same methodology steps have been followed by both [46, 48]; they are extremely different in terms of achieved performance.

Singh *et al.* [43] have noted the important effect of Gaussian kernel parameters on the subsequent image processing stages. Singh *et al.* [43] followed same procedure that was proposed in [46, 48] as well. However, the parameters of Gaussian function have been modified in a way that enhances the overall performance that reached up to 0.9459 for accuracy and 0.9721, 0.6735 for specificity and sensitivity respectively using DRIVE dataset in comparison with average ROC area of 0.9352 was reported by Al-Rawi *et al.* [49] applied on DRIVE dataset, where they used different set of modifications for Gaussian-kernel parameters.

On the same procedure that have been reported in [43, 46, 48], Kaur and Sinha [50] employed Gabor filter instead of Gaussian one in the early stages of vessel

extraction. The enhanced vessels were obtained via banks of 12 different oriented Gabor filters in range of 0 to 170 degree. Gabor-filter based approach outperforms the Gaussian one in terms of both area under ROC curve and in terms of specificity. The overall achieved sensitivity is less than that achieved by [43, 46] , on the other hand ; the performance of [43, 46] was evaluated via DRIVE dataset whereas the performance of [43] was evaluated on both DRIVE and the challengeable (*pathologies bearing*) STARE dataset where it shown a high specificity of 96% in the presence of lesions in abnormal retinal images.

Based on the fact that retinal vessels have symmetric Gaussian cross-section profile while the cross-section profile for the non-vessels is asymmetric one; a couple of matched filters one constructed with symmetric Gaussian (zero-mean) kernel and the other with first-Order Derivative Of Gaussian (FDOG) kernel were applied to retina images by Zhang *et al.* [51]. The response of matched filter that has Gaussian kernel was used to detect vessels while the local mean of the response of first-order derivative of Gaussian kernel was used to establish and adjusting a "dynamic threshold "which, in turn, was used in the thresholding phase that followed the matched filter phase. The proposed technique exploits the difference between FDOG kernel responses for both vessels and non-vessels regions (such as bright blobs, lesions, and optic disk) to vary thresholding level according to local mean signal. The experimental results that obtained via both DRIVE and STARE datasets, demonstrated that applying hybrid matched filtering kernels can reduce the false detection dramatically to less than 0.05 rather than that inherently generated with Gaussian kernel even for thin vessels with average accuracy of 0.9510 for normal cases retina images and 0.9439 for pathological ones.

According to techniques reported and discussed above, most of conventional matched filters-based approaches enhance the performance of matched filter-based methodology by enhancing the performance of the thresholding techniques rather than improving the matched filter kernel itself. Zolfagharnasab *et al.* [52], on the other hand, replaced the Gaussian kernel of matched filter by Caushy Probability Density Function (CPDF), where it has reported an overall accuracy of 0.9170 with 3.5% of false positive rate via DRIVE dataset.

The inherent zero-crossing property of Laplacian of Gaussin (LoG) filter was exploited in an algorithm was proposed by Kumar *et al*. [53] where two-dimensional matched filters with LoG kernel functions are applied to fundus retinal images in order to detect retinal vasculature structure which are firstly enhanced by Contrast Limited Adaptive Histogram Equalization (CLAHE) method. The proposed algorithm has achieved average accuracy of 0.9626, and sensitivity and specificity of 0.7006, and 0.9871 via DRIVE dataset and average accuracy of 0.9637 and 0.7675 and 0.9799 for sensitivity and specificity, respectively via STARE dataset in comparison with average accuracy of 0.9340 and 0.7060 and 0.9693 for sensitivity and specificity respectively on DRIVE dataset achieved by Odstrcilik *et al.* [37] using improved two dimensional matched filter with two-dimensional Gaussian kernel. The method was applied on STARE dataset as well, where it has achieved an overall accuracy of 0.9341 and 0.7847, 0.9512 for sensitivity and specificity respectively.

As a novel matched filter kernel improvement, Singh and Strivastava [42] suggested the Gumbel PDF as a kernel function, where they noted the slight skewness of vessel-cross section profile which is most likely approximate Gumble PDF with respect to Gaussian and Caushy PDF functions that proposed in [41] and [49]. In the thresholding phase, entropy-based optimal thresholding was used in a companion of length filtering as post-processing step in order to remove isolated pixels. The proposed technique shown an improved performance in terms of average detection accuracy 0.9522 for DRIVE dataset and 0.9270 for STARE dataset and the value of area under ROC curve was 0.9287 and 0.9140 for DRIVE and STARE datasets respectively. Since the performance metrics used in reported papers are not common, Figure 2.11and Figure 2.12 illustrate a graphical comparison between some of reviewed kernel-based methodologies for DRIVE and STARE datasets based on accuracy, sensitivity and specificity metrics for retina vasculature segmentation.

Roychowdhury et al. [54] presented a novel classification-based optic disc segmentation algorithm that detects and extract the OD boundary as well as the location of vessel origin pixel. The proposed algorithm consists of three major stages. In the first stage, the green layer of each retina fundus image is extracted and resized. Then using a disc structuring element, the green layer is reconstructed morphologically where the bright islands of the optic disc that lie in the neighborhood of the major blood vessels are extracted. In the second stage, Gaussian mixture model classifier with six region-based features is used to classify the bright regions that obtained in first stage into bright probable OD regions and non-OD regions where the maximum vessel-sum and solidity factors are used to classify the probable OD-regions into best candidate OD regions and

remaining candidate OD regions. Convex hull transform was used to gather all candidates OD regions where a best-fit ellipse shape across the convex hull gives the final segmented OD region. The centroid of major blood vessels within the segmented OD boundary that obtained in previous stage is detected and assigned as the location of vessel origin.

The proposed algorithm has been validated using six public datasets of DRIVE, DIARETDB1, DIARETDB0, CHASE_DB1, MESSIDOR, and STARE where it showed high robustness against image illumination, imaging angles, and retinal abnormalities within competitive low computational time complexity (less than 2.14 s per image). The algorithm reported high segmentation performance reached up to 98.8%–100% for optic disc and overlap score lied in the range of 72%–84%.

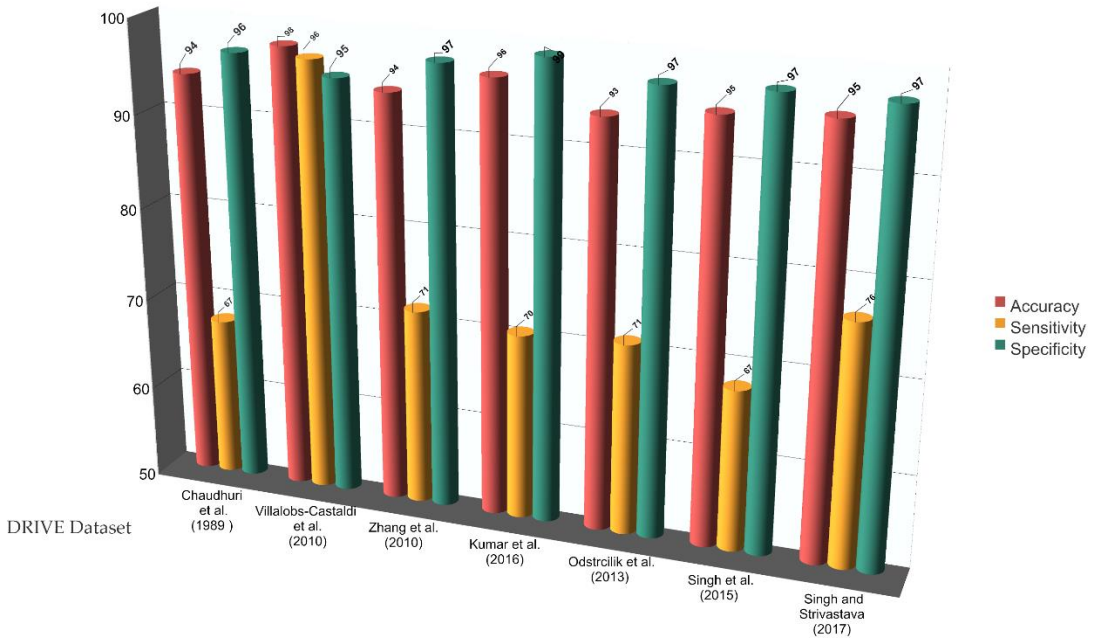

Figure 2.19 Summarized graphical comparison between some of kernel-based methods performance (Accuracy, Sensitivity and Specificity) based on DRIVE dataset.

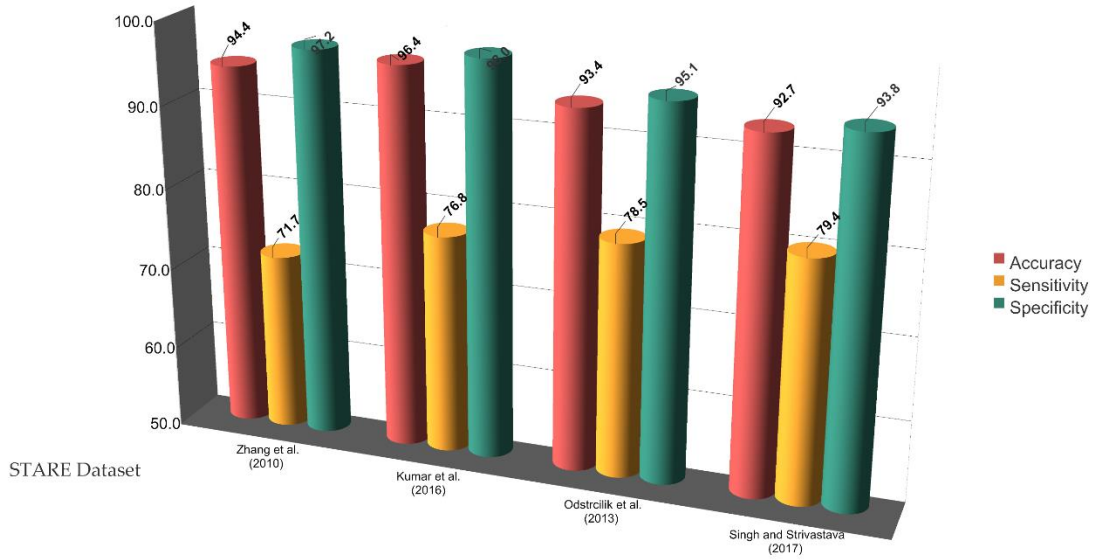

Figure 2.21 Summarized graphical comparison between some of kernel-based methods performance (Accuracy, Sensitivity and Specificity) based on STARE dataset.

2.5 Vessel Tracking/Tracing Techniques

The heart of vessel tracking algorithms is to trace the ridges of retina fundus image based on a set of starting points. Graphical representation of ridges of retina image can be noticed in Figure 2.13. Any tracking algorithm involves seeds selection as a preliminary step, where seeds can be defined either manually or automatically.

The ridges of vessels are detected by inspecting zero-crossing of the gradient and curvature. However, 'clean-limbed' ridges detection needs a pre-processing phase involves complicated steps of vessel enhancement for all vessels sizes and orientations. As a consequence, one of the major drawbacks of vessel tracking is the extreme dependency on the pre-processing steps that proceed the phase of tracing.

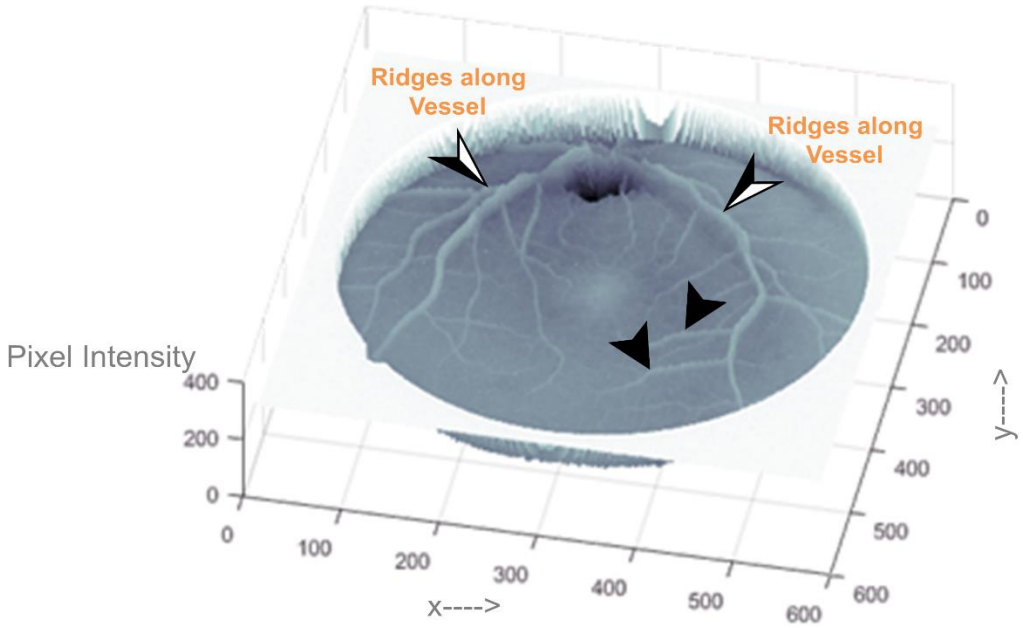

Figure 2.23 Graphical representation of ridges along retinal vasculature tree.

In tracing techniques, it is not an essence for seed points (*starting points of tracking process)* to be located at the center of retinal vessels, Chutatape *et al.* [55] ,for instance, have extracted seed points from the circumference of the optic disc, then the centers of vessels were traced using an extended Kalman filter. a semi-ellipse was defined around the optic disk as a searching region for starting points of vascular structure which was later used by [56]. As the candidate pixels locations for next vessel edge points were selected on the semi-ellipse, vessel tracking took place based on Bayesian theory.

Wu et al. [57] proposed a vessel tracking methodology for retinal vasculature structure extraction combines Hessian and matched filters and an idea of exploiting the edge information at the vessels parallel boundaries that first proposed by Sofka and Stewar [58] for retinal vessels extraction. Once the contrast between vessels and other retina tissues are enhanced and the information of sizes and the orientations of enhanced

vessels are available, the ridges are used to trace vessel via their center lines along ridge seeds that have been already selected automatically. The tracking performance was tested via DRIVE dataset, where 84.4% of retinal vasculature skeleton was successfully detected with 19.3% false positive rate, where the majority of false tracked vessels were the small ones and the researchers considered it as a subject of further ongoing research.

In contrast to [57], Yedidya and Hartley [59] proposed a tracking methodology trace the retinal vessels centers through Kalman filter, where it has the capability to detect both wide and thin vessels even in noisy retinal images by defining a linear model. The proposed model proceeds into four stages: (1) firstly, set of seed points all over the image were found by convolving the whole retina image with a set of matched filters at different scales and orientations in aim of finding at least one seed point at each vessel which, in turn, remove the need to follow all branches. (2) secondly, Kalman filter was used to trace blood vessels' centers starting from seed points that found in first stage. (3) thirdly, tracing process was ceases once the probability of vessel tracing is small for a number of back-to-back moves or once tracing hit previously segmented vessel. (4) finally, the segmentation results were traced in case of tracking failure in less than minimum number of steps. The proposed tracking methodology managed to detect retinal vessels with true positive rate reached up to 85.9% and false negative of 8.1% via DRIVE dataset.

Making use of mathematical graph theory, De *et al.* [24] designed a novel technique to extract the filamentary retinal structure. Their technique was built based on connecting the tracing problem and the digraph matrix-forest theorem in algebraic graph theory with a primary goal to address the vessel cross-over issue. The proposed technique composed of two main stages: (1) *Segmentation step*: the main skeleton of the retinal

vasculature structure was extracted. (2) *Tracing step:* the first step was used to construct the digraph representation which enabled tracing task to cast as digraph-based label propagation using Matrix-forest theorem. The proposed technique was used for both retinal and neural tracing where the empirical evaluation of the proposed technique showed high achievable performance in both cases.

Yin *et al.* [60] presented a statistical based tracking method as an improved version of a work suggested by [61]. This method detects edge points iteratively based on a Bayesian approach using local grey levels statistics and continuity properties of blood vessels. Then, it combines the grey level profile and vessel geometric properties for sake of both: accuracy improvement and tracking robustness. Experiments on both synthetic and real retinal images (DRIVE dataset) shown promising results where the true positive rate that obtained was 0.73 whereas the obtained false positive rate was 0.039. However, due to relatively low attained detection rate (TPR), a deeper evaluation on retinal images is needed to make the proposed method widely usable for vessel detection technique.

2.6 Mathematical Morphology-based Techniques

Originally, mathematical morphology belongs to set theory of *mathematics* science, where it is considered an application of lattice theory to spatial structures. Mathematical morphology concerns about the shapes that exists inside the image frame instead of pixels' intensities. That means it ignores the details that regard image content where the pixel intensities are viewed as topographical highs as shown in Figure 2.14.

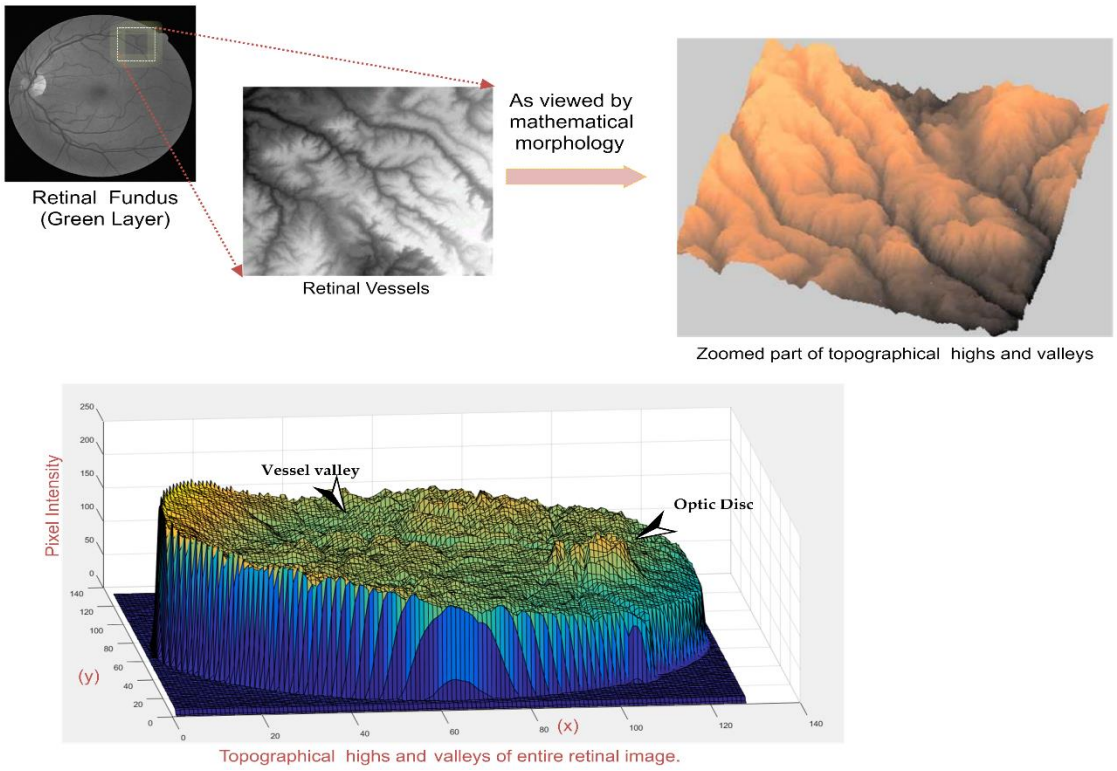

Figure 2.25 Topographic highs of retinal vessels.

Typically, mathematical morphology was used to binary images, then it has been extended to gray and colored ones, as a general processing framework, through morphological operators. In terms of mathematical morphology, the image I is represented as a set of $I \subseteq \Re^2$where foreground pixels are the members that belong to I whereas the background ones belong to the complement I^c. The image I undergoes a transformation by another set known as structuring element. Typically, the morphological operations can be applied to binary images and then can be extended to gray images. Majorly, morphological operations can be divided into: erosion, dilation, opening and closing operations. Erosion operation is used to lessen the objects in the image whereas the dilation one is used to boost it.

On the other hand, morphological openings are used to remove the unwanted structures in the image by applying an erosion followed by a dilation whereas in case of morphological closing, some of structures in image are filled or merged by applying dilation operation followed by erosion one.

In aim of retinal vessel segmentation, a Morphological Angular Scale-Space (MASS) technique was proposed by [62]. The basic idea of the proposed technique was to rotate a varying length (multiscale) linear structuring element at different angles in order to determine the connected components and assuring the connectivity across vessels where the scale-space created through the variation in the length of linear structuring elements. Gradual evolution to higher scales lessens the non-vessel like elements out of the processed retinal image where the extracted information from lower scales was used to build the retinal image of higher scales. At a certain scale (determined by authors experimentally) and using a vessel-ness measure was proposed by [63], the proposed method reported a lowest mean square error value of 0.0363 which have been averaged over 50 retinal images taken from DRIVE dataset.

In addition to morphological operations, morphological tools are used in retinal vessel segmentation tasks including: gradient, watershed transform, top-hat transform, distance function and geodesic distance. Watershed transform has been developed in the framework of mathematical morphology by Digabel and Lantu´ejoul [64]. The principal idea underlying this method was inspired from geography when a landscape is flooded by water, then watersheds appear as divide lines of the domains of rain falling over the entire region [65]. A watershed-based segmentation algorithm was used by Frucci *et al.* [66] to segment retinal vasculature structure.

The proposed algorithm combines watershed transform and both contrast and directional information extracted from retinal image. First, watershed transform was used to segment the image into multi-regions. Then, a unique gray-level value was assigned to each single region. A contrast value was computed for each region through calculating the difference in gray-level with respect to its adjacent regions. A 9×9window was applied to each pixel in order to attain the directional map that composed of 16 directions. The standard deviation of pixels' gray levels is aligned along these directions. Then, based on the occurrences of directions within watershed region, pixels locating in same region are assigned same direction. Once the contrast and directional maps had been obtained for each watershed region, a precursory segmentation of retinal vascular structure was acquired where the regions with highest contrast (positive difference) were most likely considered as non-vessel regions. Otherwise, they were considered as vessel ones. The proposed algorithm has been developed using DRIVE dataset and has achieved a detection precision of 77% and accuracy of 95%.

Jiang *et al.* [67] presented a novel work to extract the retinal vasculature structure, by using global thresholding based on morphological operations. The proposed system was tested via DRIVE and STARE datasets and has achieved an average accuracy of 95.88% for single dataset test and 95.27% for the cross-dataset test. In terms of time and computational complexity, the system has been designed to minimize the computing complexity and processes multiple independent procedures in parallel, thus having an execution time of 1.677 seconds per each retinal image on CPU platform.

2.7 Multi-scale Techniques

The core idea behind the multi-scale representation is to represent the image at multiple scales(levels) where the data contained in a given image is embedded into one-parameter family of derived images at multiple scales [68] as shown in Figure 2.15.

This representation is constructed provided that the structures at coarse scales (levels) are the simplified versions of the corresponding structures at fine scales by convoluting with smoothing kernels. The only possible smoothing kernels that meet the linearity and spatial shift invariance are the *Gaussian* and its *derivatives* kernels that have increasing widths (scales σ) [69].

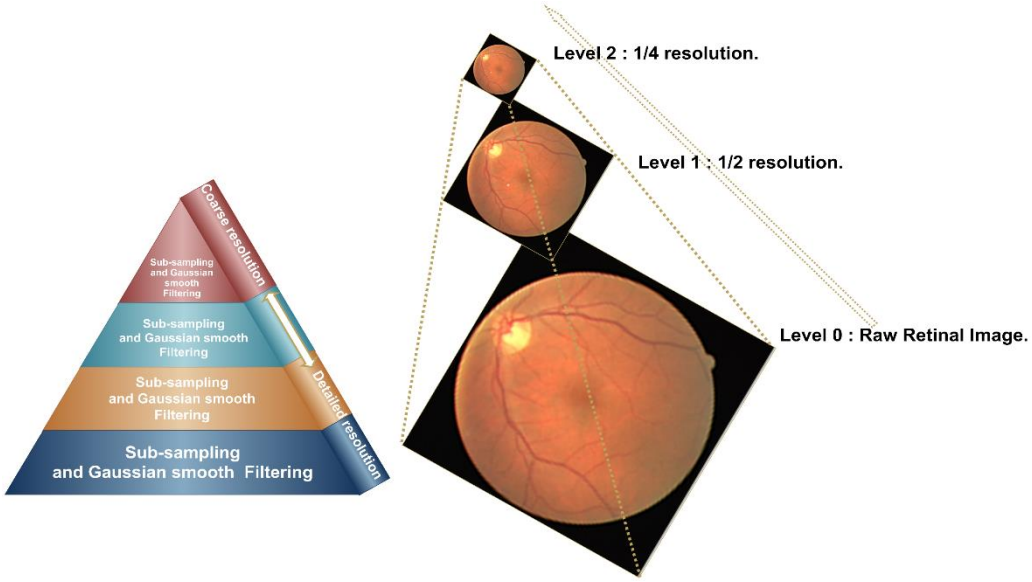

Figure 2.27 Level scaling idea of multi-scale method.

Originally, the scale-space is the framework of the multi-scale image representation [70], two widely-used types of multi-scale representation are : pyramid [71], [72] and Quad-tree [73]. Most of retinal vessels segmentation methodologies are built based on the pyramid multi-scale type, where the grey-level data is represented in

such a way that combines sampling operations with successive smoothing steps conducted by Gaussian kernels with different scales gives rise to a response that is represented by 2D Hessian matrix [74]. The eigen values of Hessian matrix determine the vessel-likeness which, in turn, result in retinal vasculature structure enhancement. Hessian matrix processing through eigen values analysis aims to obtain the principal directions of vessels where the decomposition of local second order structures in retinal image can be performed in order to attain the direction of the smallest curvature along the retinal vessels [75].

The retinal image size decreases exponentially with scale level as illustrated in Figure 2.15, as a consequent result, the amount of required computation too. However, it shows weakness in extracting fixed-size structures such as optic disc and nonuniform structures such as retinal lesions. Thus, multiscale approaches can be best suited for structures have varying width and length (coarse and fine) in the same image.

A typical multi-scale based technique for retinal vessel segmentation was proposed by Budai *et al.* [76]. The proposed technique composed of three major phases: (1) Gaussian pyramid generation, (2) Neighborhood analysis and (3) Images fusion. After the green channel of raw retinal image was extracted, Gaussian pyramid of resolution hierarchy was generated. The hierarchy composed of three levels (level 0, level 1, and level 2 as shown in Figure 2.15). The original retinal image (green channel) has the highest resolution (level 0), the width and height of image begin reducing as we move towards further levels (fine to coarse levels).

In the second phase, for each level, an 3×3 neighborhood window analysis for each pixel was analyzed by calculating Hessian matrix followed by calculation of a couple of eigenvalues $\lambda_l \; and \;\; \lambda_h$ of Hessian matrix which reflect the scale of lowest curvature λ_l and the highest one λ_h in the neighborhood window of the target pixel. Then, the ratio of these values was used to calculate a vessel likeness measure $P_{vessel} = 1 - \frac{\lambda_l}{\lambda_h}$; the value of P_{vessel} determines whether target pixel belongs to vessel tree or not. If P_{vessel} value is close to one, it means it most likely a vessel pixel since $\lambda_l \; and \;\; \lambda_h$ are similar to each other. This analysis was applied to each pixel in every scale (level). At the final stage, segmentation results from different levels were undergone binarization using two hysteresis thresholds, then they merged together using pixel-wise OR operation, which yielded the final segmented image. The methodology has achieved an accuracy, specificity, and sensitivity of 93.8%, 97.5% and 65.1% on STARE dataset, and 94.9% ,96.8% and 75.9% on the DRIVE dataset.

Abdallah *et al.* [77] proposed a two-step multi-scale retinal vessel detection algorithm. As a first step, the noise-corrupted retinal image (gray layer) was denoised against the additive Gaussian noise by applying a flux based anisotropic diffusion technique; a multi-scale response of multi-level resolution of retinal image was computed. Then, as a second step, a vessel model was established in order to analyze the eigenvalues and the eigenvectors of Hessian matrix for each scale. Final result of multi-level analysis represents the pixel-wise maximum of the results were obtained over all scales. The proposed algorithm reported area under ROC curve of 0.94514 on STARE dataset.

Rattathanapad *et al.* [78] presented an algorithm to segment the blood vessel in retinal images based on multilevel line detection and connection of line primitives. Multilevel line detection is used for extracting the retinal vessels at multiple values of Gaussian smoothing parameters. Then the line primitives that extracted at different scales were merged into one single vessel extraction result. The proposed algorithm was validated using DRIVE dataset where it proved the capability to detect most of the major part of vessel skeleton with false positives.

A new approach based on a multi-scale method for segmentation of retinal vessel was proposed by Moghimirad *et al.* [79] where it used weighted Medialness function along with the eigenvalues of the Hessian matrix. The proposed approach consists of two phases. In the first phase, the medial axis of retinal vessels was extracted using a two-dimensional Medialness function in multiple scales and sum of smoothed eigenvalues of the image. The second phase is for vessel reconstruction where centerline of vessels was extracted and radius of vessels was estimated simultaneously in order to obtain the final segmented results. The proposed approach was validated using DRIVE and STARE datasets where it showed high performance in terms of accuracy and area under the ROC curve where it has achieved accuracy of 0.9659 with area under ROC of 0.9580 via DRIVE dataset and accuracy of 0.9756 with area under ROC curve of 0.9678.

2.8 Model-based Techniques

The concept of deformable model is used to describe a set of computer vision techniques and algorithms that abstractly model the variability of a certain class of objects in an image (vessels in retina image). The most basic versions of these algorithms concern with shape variations modeling where the shape is represented as flexible curve or surface, then it can be deformed to match specific instance of the object class [80]. The deformation is not an arbitrary process, rather it is performed based on two powerful theories: *Energy Minimization* and *Curve Evolution* which have roots in physics ,geometry and approximation theories [81]. Deformable models can be divided into two main categories: parametric and geometric ones [82].

2.8.1 Parametric Deformable Models

Parametric deformable modeling or as it called snakes or active contours, are parametrized curves that depend inherently on particular parameter in order to create it. The major goal of active contour modeling is to segment objects in retinal images by fitting the curve to objects' boundaries in the image. It is called dynamic contour modeling since it initialized at a place in the neighborhood of target object, then the model can evolve dynamically to fit the shape of object by an iterative adaption. The major idea of snakes is to represent a curve via parametric curve, however, since it depends on a parameter that control the movement of curves (when slithering as snakes) during fitting process, it is rigid topologically, namely, it has not the flexibility to represent objects that composed of variable number of independent parts [80]. Moreover, another widely-recognized issue associated with snake-based segmentation technique is the incapability

of snakes to converge to the correct vessel edges in the presence of high level noise or if the vessels were "empty" or have relatively low contrast levels [83].

A novel segmentation algorithm built on snake contours was developed by Jin *et al.* [83]. The proposed technique consists of three major steps: (1) First, parameter initialization technique that based on Hessian feature boundaries, where the Hessian feature was used to extract all darker linear structures in retinal image, then, the retinal image was divided into (N) segmentation regions (R), based on the seeds of extracted linear structure. (2) In the second step, each segmentation region R was represented as image through utilizing pixels' average intensity influence, then, the snake energy function was constructed on this image representation in order to realize the snake's locations from the neighborhood of vessel edges to real ones. (3) Finally, as all model-based methodologies end, a region growing technique was used in order to get the final vessels' area, then the grown area was post-processed via context feature. The proposed methodology validated on DRIVE dataset and has reported a competitive performance reached up to 95.21% (accuracy), 75.08% (sensitivity), 96.56% (specificity).

An efficient and effective infinite perimeter active contour model with hybrid region terms for vessel segmentation was proposed by Zhao *et al.* [84]. The proposed model used hybrid region information of the retinal image the proposed model used various types of region information, such as the combination of intensity information and local phase-based enhancement map. For its superiority; the local phase-based enhancement map was used to preserve vessel edges whereas the given information of image intensity guaranteed a correct feature's segmentation.

The proposed method was applied to DRIVE and STARE datasets where the methodology has achieved sensitivity, specificity and accuracy of 0.780, 0.978 and 0.956, respectively on STARE whereas for DRIVE, the measures are reported to be 0.7420, 0.9820 and 0.9540, respectively.

2.8.2 Geometric Deformable Models

Fast Marching methods and level sets methods are considered numerical techniques devised to track the propagating interfaces, the starting point for geometric deformable methods comes from the evolution analysis of the curves and surfaces, as it considered *interfaces*, that firstly proposed by the mathematician Sethian, J. A. in both references [85, 86]. Afterwards, Caselles *et al.* [82] suggested to represent the curve depending on Euclidian distance rather than parameters-dependency by representing a curve as a level set; that means, the contour is represented as zero-level set of an auxiliary distance function $\emptyset$; level sets theory paved the way to represent contours in flexible manner, where it can join or break apart without the need of reparameterization.

Gong *et al.* [87] used a novel level set technique does not need level set function initialization, by using local region area descriptor. The proposed technique involves two major steps: (1) First, a contour C was found, then it was used to divide the entire retinal image into several parts based on whether the pixel position is inside the contoured area or not. (2) Then, a clustering algorithm was applied on the sub-regions were resulted in first step, which in turn, yielded local cluster value, namely, a new region information that used to redefine an energy functional in the first step until the algorithm converged. Second step represents key contribution of this paper, since it eliminates the effect of

inhomogeneity of retinal image pixels' intensities, moreover, it gives more information about the local intensity information at level of image pixel, this eliminates the need for level set function re-initialization that is considered a major drawback of level sets-based techniques. The proposed technique was tested on DRIVE dataset and an accuracy of 0.9360, sensitivity of 0.7078 and specificity of 0.9699 are reported.

A novel modification to level set based retinal vessels segmentation was presented by Dizdaro *et al.* [88] in terms of initialization and edge detection phases that needed as a pre-requirement for level set based techniques. In the initialization phase, the seed points were determined by sampling centerlines of vessels based on ridge identification, then accurate boundaries of the retinal vessel tree were determined through phase map built based on ridge detection technique. The proposed algorithm was tested on both DRIVE dataset and a dataset created by paper's authors. The algorithm has achieved the values of 0.9412, 0.9743, and 0.7181 for accuracy, specificity and sensitivity, respectively for DRIVE and 0.9453,0.9640 and 0.6130 accuracy, specificity and sensitivity, respectively on the proposed dataset. As a conclusion, both deformable models either parametric or geometric share a common problem, both require, as essential step, a set of seed points that are determined either manually or automatically.

2.9 Adaptive Local Thresholding Techniques

Thresholding is considered one of the most well-known, plain and direct methodologies to image segmentation in general and to medical image segmentation in particular. Whereas the objects arrangement in the natural scene images looks relatively

undistinguishable, the arrangement of objects including the organs and tissues in the medical image is usually more discernible.

Therefore, thresholding segmentation techniques are used extensively in the researches that involve the medical image segmentation where different tissues and organs represented in different gray levels. Typically, thresholding techniques, in its basic framework, search for a global value (level), that optimally maximizes the separation between different classes (different tissues in our case) in the image. The effectiveness of thresholding with a global level manifests if the objects in the image under consideration have well-defined areas and if the gray levels can be congregated around values with minimum interference.

Uneven illumination, inferior quality of source material, camera artifacts/distortions, and anatomical objects with multi-classes and hybrid features make the global thresholding for the entire retinal image a major source for segmentation errors. Moreover, since retinal image shows soft transition between different gray levels, uneven illumination or noise distortions, the principal segmentation errors begin to appear due to pixel-wise approach that adopted by global thresholding, namely, the pixels that have same gray levels (pixel intensity) will be segmented into the same anatomical object; which is considered a long-standing issue of global thresholding with a single hard value. In order to resolve these issues, region-wise thresholding methodologies have been suggested for case of retinal vessels identification, developed and implemented via different techniques which can be classified into three major categories: statistical, knowledge-based and fuzzy-based adaptive thresholding as shown in Figure 2.16.

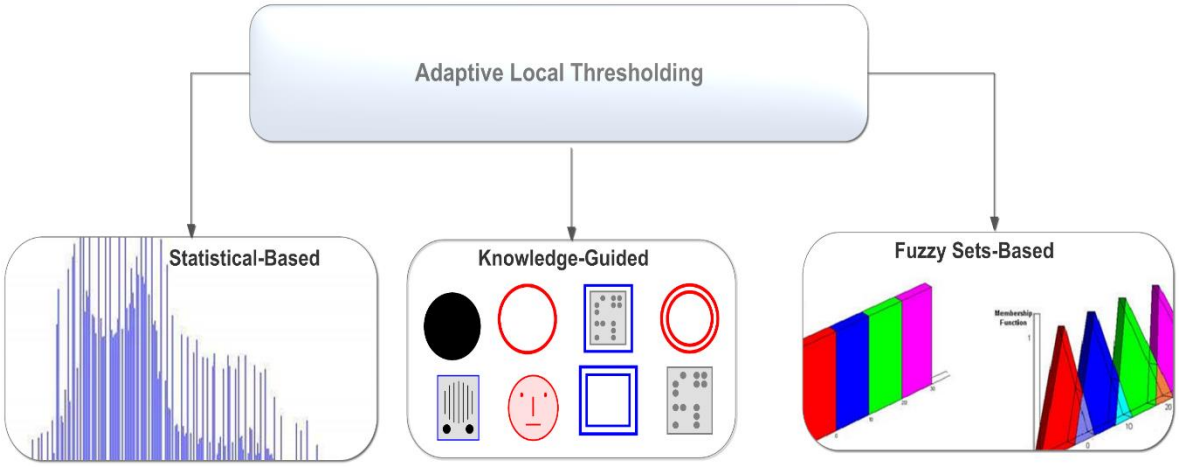

Figure 2.29 Adaptive local thresholding taxonomy.

A novel work by Christodoulidis *et. al* [89] focused on segmenting small thin vessels through Multi Scale Tensor Voting (MTVF) scheme, based on the fact that small vessels represent nearly 10% of the total surface of vascular network [90] which , in turn, represents the framework of statistical-based adaptive thresholding. The proposed technique consists of four major stages: pre-processing and multiscale line detecting vessel enhancement, adaptive thresholding and MTVF processing, and post-processing stage. In the pre-processing stage, the green channel of raw retina image was extracted. Then, image contrast was enhanced by applying a contrast correction approach proposed by [91]. Dual-tree complex wavelet transform [92] was used to remove noise. Following the pre-processing stage, retinal vessels were enhanced via multi-scale line detection approach proposed by [93]. The output of multi-scale line detector was fed into adaptive thresholding processer in order to isolate vessels.

In order to obtain various levels of adaptive thresholding, authors have fitted the histogram of MSLD response to a simple Gaussian function and modified the optimum global threshold [94] by varying the distance from the mean of Gaussian function through following equation :

$$T = |\mu_{Gaussian}| + \alpha|\sigma_{Gaussian}| \quad (2.5)$$

where $\mu_{Gaussian}$ and $\sigma_{Gaussian}$ are the mean and standard deviation of the fitted Gaussian function. Then, various thresholds revealed through experimentally changing α parameter which is considered the heart of adaptive thresholding. Once the adaptive thresholding step has been performed, many smaller vessels stayed apart. Thus, a multi-scale tensor voting framework inspired by [95, 96] have been used to reconnect them.

In summary, adaptive thresholding was used to extract large and medium-sized retinal vessels, while MTVF was used to extract the smallest ones. Finally, as a post-processing step, morphological cleaning was used to remove the non-vasculature components remaining after applying adaptive thresholding. The proposed methodology was tested on a recently available Erlangen dataset [37] where it has achieved average accuracy of 94.79% and 85.06% ,95.82% for sensitivity and specificity respectively.

Akram *et al.* [97] used adaptive thresholding technique to locate and extract retinal vessels automatically. The statistical-based adaptive thresholding was used to create the binary vascular mask by selecting points that isolate vessels from the rest of image. The proposed method has two major phases; pre-processing and adaptive thresholding phases.

In the first phase, the monochromatic RGB retinal image was fed into Gabor wavelet filter in sake of vasculature pattern enhancement, more specifically, thin and less visible vessels, based on an image analysis technique proposed by [98].

The yielded enhanced retinal image has maximum gray values occur for background whereas pixels belong to vessels have a slightly greater intensity values rather than that belong to background. The proposed technique has been tested using DRIVE dataset where it has achieved an average accuracy of 0.9469 with area under ROC curve approximate value of 0.963.

A knowledge-guided local adaptive thresholding was proposed by Jiang and Mojon [99] where a verification-based multi-thresholding probing scheme was used. In its most basic form, given a binary image I_{binary} results from thresholding process at a threshold level T; then, a classification procedure is used to decide if any region in I_{binary} can be defined as an object. The operation is carried out on a series of different thresholds. The final image segmentation is set by combining different results of different thresholds. In summary, the objects hypotheses in an image are generated by binarization via some hypothetic thresholds and then according to a particular classification procedure, the object is accepted or rejected. The classification procedure represents the core of this proposed algorithm, where any piece of information related to object under consideration is incorporated, such as shape, color intensity and contrast. This is why it is called *knowledge-guided* technique since during segmentation, thresholding levels varying according to the knowledge available about the target object.

A novel two-approaches adaptive algorithm was proposed by Sharma et al. [100] for automatic optic disc localization and detection. The first approach used the directional

features of vessel structure and a set of optic nerve head features as the key detection factors to the segmented vascular structure such as image variance, density of vessel pixels, number of connected components, vessel intersection points, maximum intensity regions and angle of intersection between vessel segments. In the second approach, the parabola fitting to the segmented vessels was used to identify a mask that contains 40%-100% portion of the optic disc. Then, searching for a point inside the selected OD mask is performed through iterative steps where keeping the search area limited to the selected mask area instead of searching for OD point in the whole retinal image highly affected the algorithm robustness against pathological lesions that may exist in retina images. The algorithm performance has been evaluated using six public databases containing both normal and abnormal retina images. The Optic disk mask was successfully identified in 1642 images out of 1650 images with accuracy of (99.77%).

2.10 Machine Learning Techniques

While pattern recognition has its roots in engineering, machine learning was developed in computer science [101]. Pattern recognition has become more well-known and active research field since 1960s' [102], and has undergone a considerable development for many years which yields a variety of paradigms and methods have important applicability in many fields; retinal vascular structure is such a one. Machine learning algorithms are typically divided into three major categories: *supervised*, *unsupervised* and *reinforcement learning*. This categorization is mostly based on the availability of responses y for input data x.

Supervised learning addresses the problems where for each input x, there is a corresponding observed output y, whereas in case the latter two categories this correspondence cannot be found due to the lack of data.

Unsupervised learning explores interesting patterns in the input data without a need for explicit supervision [103]. On the other hand, reinforcement learning assumes that the dynamics of the system under consideration follows a particular class of model [104].

A back propagation artificial neural network vessel classifier was designed by Nekovei and Ying [105] to identify the blood vasculature structure in angiogram images. The proposed technique uses the raw gray-intensity values of pixels instead of feature extraction. Each pixel in the image is processed by creating a window around it which covers number of pixels, then the raw gray intensities of these pixels are fed into the neural network as input. In order to cover the entire image, a process of sliding windows, pixel by pixel takes place. Training dataset consists of manually selected patch samples of angiogram where the distribution of vessel and background pixels kept roughly equal in order to prevent neural network biasing towards background pixels' classification. The proposed method has avoided the complexity of feature extraction. besides, the method has achieved vessel detection performance of 92% performed on angiograms.

The transfer learning and domain adaptation [106] has been investigated in the field of retinal vessels segmentation by [107] where a denoised stacked auto-encoder neural network was trained with ample labeled mini-patches of retinal images taken from DRIVE dataset. DRIVE dataset represents the source domain where the auto-encoder was adapted to deploy on STARE dataset which represent target domain. The stacked auto

encoder consists of two encoding layers with 400 and 100 nodes per layer respectively, then it is followed by a SoftMax regression layer. Due to power of knowledge transfer, the proposed technique exhibited an accelerated learning performance with area under ROC curve of 0.92.

For an exhaustive detection of fine retinal vessels, Maji *et al.* [108] designed a hybrid framework of deep and ensemble learning where a Deep Neural Network (DNN) was used for unsupervised learning of vesselness via denoising auto-encoder, utilizing sparse trained retinal vascular patches. the learned representation of retinal vasculature patches was used as weights in the deep neural network, then the response of deep neural network was used in supervised learning process with a random forest for sake of vasculature tissues identification. The high capability of denoising auto encoder to learn feature representation was furiously exploited. The method was trained and tested via DRIVE dataset. Although the achieved average accuracy was 0.9327, it is considered marginally weak in contrast with state of art approaches, the performance consistency of the method and the capability to identify both coarse and fine retinal vascular structures are considered its unique ambience.

Invigorating by the success of [107, 108], Lahiri *et al.* [109] has presented an ensemble of two parallel levels of stacked denoised auto-encoder networks. Each kernel is accountable for distinguishing a particular orientation of vessel. First level of the ensemble is composed by training (n) parallel stacked denoised autoencoders have the same architecture, whereas second level is implemented by parallel training of two stacked denoised autoencoders, then the final architecture was fine-tuned until a satisfied accuracy has been achieved. The decisions of individual members of the ensemble are

combined by a simple SoftMax classifier. The method proves to be reliable and consistent in addition to high average detection accuracy that reached up to 0.953.

Contemporaneous research proposed by Maji *et al.* [110] uses deep neural network technique ensemble of twelve convolutional neural networks to distinguish vessel pixels from non-vessel ones. Each convolutional neural network has three convolutional layers; each one was trained separately using a set of 60000 randomly selected $31 \times 31 \times 31$-sized patches taken from 20 raw color retinal images of DRIVE dataset. At the time of deduction; the probabilities of vesselness were produced by each convolutional network in a separate manner. Then, the individual responses were averaged in order to form the final vesselness probability of each pixel. Although the method has not achieved the highest detection accuracy 0.9470 among other methods, it exhibited superior performance in terms of learning vessel presentation from data due to the fact that multiple experts represented by ensemble of conventional networks are more powerful and accurate than one neural network.

Detecting and restoring small foreground retinal filamentary structure was handled by Gu and Cheng [23] using an iterative two-step approach built based on Latent Classification Tree (LCT) model. After the confidence map has been constructed, a sufficiently high thresholding was placed on it, yielded a partial segmented image contains the main (thick and long) vessels. Using latent classification tree, the remaining low confidence map (filamentary filaments) was obtained. The filamentary structure was re-connected to main filaments (large vessels) via novel matting and completion field technique. These steps performed iteratively until the whole retina surface was scanned. The proposed method has achieved high detection accuracy reached up to 97.32% for

DRIVE dataset and 97.72% for STARE dataset, which is considered an expected result due to the noticeable degradation in the false positives produced by false detection of fine retinal filaments. Although the proposed method has achieved encouraging performance, it has a broad range of applications in the fields other than retinal vessels extraction such as 3D magnetic resonance angiography and neural tracing.

A fast and accurate automated segmentation method for retinal and optic disc structures was proposed by Maninis *et al.* [25]. Their method uses deep Conventional Neural Networks (CNNs) as supervised segmentation methods. As all neural networks, the layers of CNN were trained in a specialized manner in order to address both retrial and optic disc segmentation. The proposed method was validated using DRIVE and STARE dataset for retinal vessel segmentation task where the area under recall-precision curve has reached up to 0.822 for DRIVE dataset and 0.831 for STARE dataset. In context of CNN-based approaches, remarkable performances have been achieved by Liskowski *et al.* [111] with supremum area under curve(AUC) of 0.99 and accuracy of 95.33% and AUC of 0.974 have been achieved by Dasgupta and Singh [112] for automated retinal vessel segmentation.

A novel enhancement applied on the classic K-nearest neighbor (KNN) clustering algorithm for retinal vessel segmentation has been demonstrated by Salem *et al.* [113]. Each pixel was represented by a feature vector composed of green channel intensity, local maxima of the gradient magnitude and the local maxima of the largest eigenvalue. Based on these features, image pixels were clustered using the modified version of KNN without using training set. The segmentation algorithm was evaluated on the STARE dataset resulting in an average sensitivity and specificity of 77% and 90% respectively for three

features vector and 76% and 93% respectively using only one-feature (maximum eigenvalue) vector.

A fuzzy-based retinal vessel segmentation methodology proposed by Sharma and Wasson [114] used the difference between low-pass filtered and high-pass filtered version of retinal image as input for fuzzy-logic based processing. The fuzzy logic consists of different sets of fuzzy rules; each fuzzy rule was built based on different thresholding values. Thresholding values were used to select and discard pixels values according to fuzzy rules; which in turn, led to vessel extraction. The methodology has attained an average accuracy of 95% on DRIVE dataset.

Two-stages combination between vessel tracking and fuzzy logic techniques was proposed by Akhavan and Faez [115]. In first stage, the centerlines of enhanced retinal image were detected whereas retinal vessels were filled using Fuzzy C-Means (FCM) clustering technique in second stage. The final segmented result was obtained by combining centerlines images with fuzzy segmented images. Centerlines are used as initial points for a FCM-based region growing algorithm. The evaluation of the technique resulted in an average accuracy of 72.52% on DRIVE dataset and 77.66% on STARE dataset.

A novel scheme based on combination of genetic algorithm and fuzzy c-means clustering algorithm was proposed by Xie and Nie [116]. In pre-processing stage, the green channel of raw retinal image was extracted and enhanced by histogram equalization. Then, the retinal image was divided into two major layers: texture layer and smooth layer. Texture layer was directly fed as input to the processing stage due to the amount of information that contains. The features data that obtained in first stage were

clustered via fuzzy c-means algorithm in conjunction with genetic algorithm where firstly, the genetic algorithm is used to obtain the approximate solution of the global optimal solution. Secondly, the approximate solution was used as initial value of the fuzzy c-means algorithm. Genetic algorithm eases and enhances the duty of fuzzy c-means in finding the optimal solution without falling into issue of local detection of optimal solutions.

In order to overcome the issues related to the objective function of the classic fuzzy c-means classifier, Emary *et al*. [117] utilized the possibilistic version of fuzzy c-means algorithm optimized by Cuckoo search algorithm. They used the new clustering methods, possibilistic c-means proposed by [118] and possibilistic fuzzy c-means proposed by [119] to establish an optimal version of fuzzy c-means that were used accordingly for retinal vessels segmentation. The optimality of the proposed method was examined by the heuristic search algorithm; Cuckoo Search (CS). The evaluation on the STARE dataset indicated an average accuracy, specificity and sensitivity of 0.94478, 0.987 and 0.586, respectively, whereas for DRIVE dataset, the measures reported to be 0.938, 0.984 and 0.628, respectively.

Bhargavi et al. [120] designed a four stage computer aided system for detecting exudates lesions in pathological retina images. The proposed screening system stages consists of: pre-processing, retinal anatomical structures (background and foreground structures) segmentation, features extraction and regions classification stages. In the pre-processing stage, the green layer of raw retina image was extracted and histogram equalization and contrast enhancement has been applied; followed by bilateral filter which removes remaining unwanted noise and obstacles. In the second stage, the optic

disc and the major vessels (background objects) are masked out due to high similarity between these structures and the exudates ones. The optic disc is segmented through morphological operations whereas the vascular structure through multi-scale hessian matrix. Then twenty features of both normal and abnormal regions of foreground objects are extracted. These extracted features are used in the process of candidate regions classification into exudates and non-exudates using SVM classifier. The proposed system showed satisfactory segmentation results in terms of AUC (0.966) and average accuracy reached up to (96.66%) obtained using DIARETDB1 and MESSIDOR datasets.

2.11 Summary

The existing retinal segmentation methodologies are categorized, and described in the last section. We discussed various techniques used in these methodologies for the segmentation of different anatomical structures in retinal image and compare performance result of the methods.

These methodologies were evaluated using publicly available datasets. Various retinal segmentation methodologies follow almost common procedures; each methodology initiates by *pre-processing* step where the green layer (or gray) is extracted of the raw color retinal image, then the contrast of the image is enhanced. *Processing* step represents the heart of algorithm where the different techniques that categorized in last section is used. Finally, in the *post-processing* step, the initial segmented image undergoes steps of smoothing and edges preserving and enhancement. Regarding retinal segmentation categories that shown in Figure 2.9, there is neither a best technique or

algorithm to face all performance metrics in high segmentation achievement nor a best mathematical scheme to do so.

Deciding whether the methodology is best or not depends on a set of factors including: (i) *Achieved accuracy*, which in turn, depends on the achieved specificity and sensitivity, where segmentation is considered the best if it achieves the highest possible sensitivity value (or shows low false detection to other retinal structures) at the same time, maintain the specificity at optimal level. On the other hand, the optimality of the method increases as detection capability of the method records high performance in pathological retinal images. (ii) *Time and computational complexity*: The time and computational power that required by the methods tends to be low as the accuracy has increased tendency on the condition that high performance of high accuracy has achieved. (iii) *Robustness*: the method is considered to be best if it shows robustness against method parameters variation.

The accurate detection and segmentation of the retinal structures forms the backbone of a variety of automated computer aided systems for screening and diagnosis of ophthalmologic and cardiovascular diseases. Despite of the massive number of promised methodologies have been developed and implemented, there is still room for research improvement in retinal structures methodologies especially for noisy and pathological retinal images outside the limited number of retinal images available in the public datasets. In real-life applications, retinal segmentation systems will not replace the experts' role in diagnosis; rather they will enhance the diagnosis accuracy and reduce the workload of the ophthalmologists. Therefore, large volume of patients' images can be processed with high diagnosis accuracy and comparable time.

CHAPTER 3: RETINAL SEGMENTATION SYSTEM

Although segmentation methods that mentioned in *chapter 2* have been shown to be superior to other available methods, they show incapability of detecting and extracting all anatomical structures in one system; rather, to be fully identified and segmented; each anatomical structure requires a separate stand-alone system built on a stand-alone algorithm.

Another disadvantage of previously reported schemes consists of their incapability to address retinal images containing pathologies; this inability is demonstrated by performance degradation in terms of false positive rates and reduced accuracy, chiefly due to the presence of abnormal structures such as hemorrhages, exudates, and other lesions. Identification and extraction of multiple anatomical structures in retinal fundus images is thus a complicated problem and a potential minefield.

In this thesis, we developed a system that can extract multiple retinal anatomical structures at one session with high accuracy without the need for texture analysis or synthesis. Our work exploits and combines fuzzy sets, mathematical morphology theories, and their capability for fast, accurate segmentation system.

The general prism framework of the proposed multiobject soft thresholding segmentation system is shown in Figure 3.1. The proposed system consists of three subsystems work within general framework based on hybrid combination of mathematical morphology and fuzzy set theory.

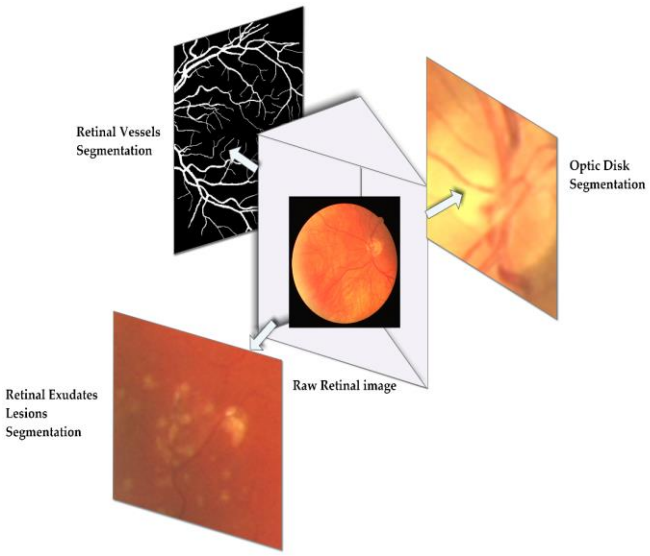

Figure 3.1 Prism of our proposed system segmentation results.

Broadly speaking, thresholding is one of the most well-known, straightforward methodologies used for image segmentation tasks generally and for medical image segmentation tasks in particular [121]. Typically, thresholding techniques search for a global value (level) that maximizes the separation between different classes (different tissues, in our case) in the image. Thresholding at a global level is effective if the objects in the image under consideration have well-defined areas and if the gray levels are clustered around values with minimum interference.

While objects in natural scenes are relatively undistinguishable, objects in medical images, including organs and tissues, are typically more distinct. Therefore, thresholding segmentation techniques are used extensively in studies where different tissues and organs are represented by different gray levels. However, when images exhibit soft transition between different gray levels, uneven illumination or noise distortions, principal segmentation errors arise due to the pixel-wise approach adopted by global thresholding: namely, pixels that have the same gray levels (pixel intensity) will be

segmented into the same object which is considered a long-standing issue in global thresholding with a single hard value. Since retinal images are a typical example of such situations, a region-wise thresholding methodology is adopted in this work. We utilize a hybrid of rule-based and machine learning techniques, where the adaptive local fuzzy thresholding represents the hard segmentation phase of proposed methodology, while morphological operations represent the soft segmentation.

To our best knowledge, only a very limited number of existing systems have focused on extracting multiple anatomical structures with high achievable performance. Furthermore, there is no record in the literature of the use of hybrid combinations of adaptive fuzzy and morphology to solve this kind of problem. In summary, in this thesis, we develop a stand-alone compact segmentation system that can identify, localize and extract multiple retinal anatomical structures that have highly distinct features in a single segmentation session, while maintaining comparably high segmentation accuracy.

In this work, we propose a system that involves new hybrid thresholding algorithm combines two powerful techniques: adaptive local fuzzy thresholding (coarse segmentation) and mathematical morphology (soft segmentation). The general flowchart of the proposed system, without regarding the acquired anatomical retinal structure, is illustrated in Figure 3.2.

Morphological operators are used in the pre-and post-processing phases of system algorithm, whereas adaptive local fuzzy thresholding is used in the processing phase, which means that it represents the core of the segmentation algorithm, even though morphological operators are considered more than complement steps.

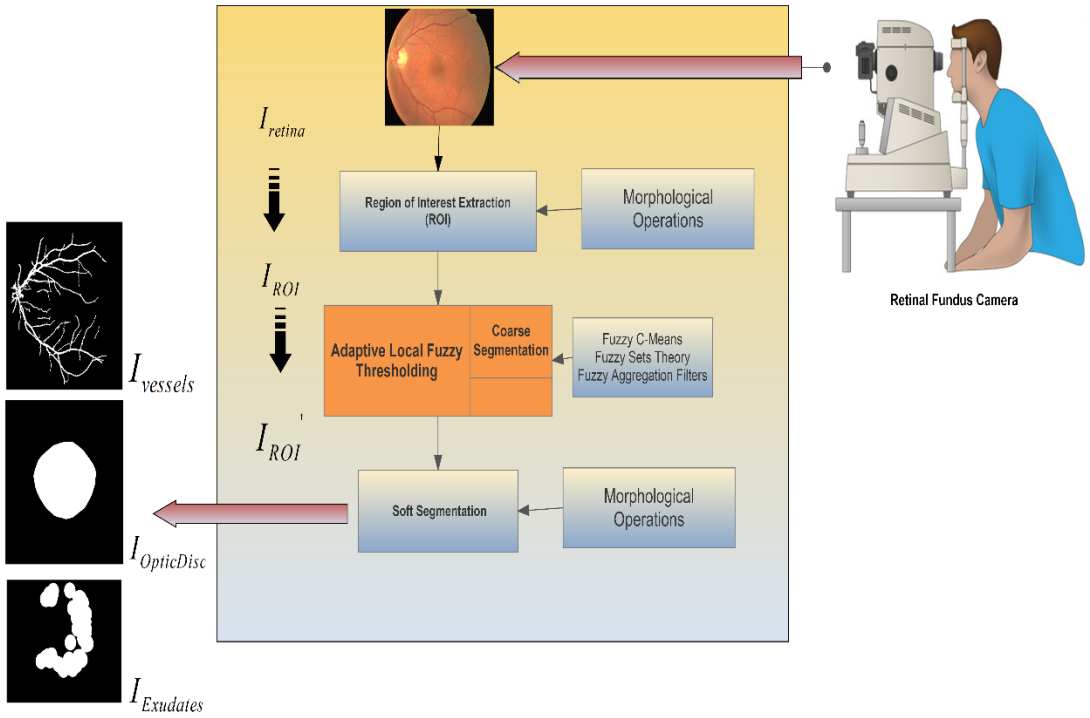

Figure 3.3 General flowchart of the proposed hybrid system.

Referring to Figure 3.2, irrespective of the target anatomical structure, our proposed system involves three major phases: Region of Interest (ROI) extraction, coarse segmentation and soft segmentation. In the first phase, the target region of interest is extracted out of the raw retina image I_{retina} in order to enhance the segmentation accuracy of the target retinal anatomical structure (vessels, optic disc or exudates lesions) and lower the computational cost, then I_{ROI} image undergoes a set of pre-processing steps involving major morphological operations that lead to initial identification of the target area. Although this phase is a preliminary one, it has a dramatic effect on the final segmentation accuracy of the fuzzy processing phase. The I_{ROI} forms the input for local adaptive fuzzy thresholding, which yields the I'_{ROI} hard-segmented image.

Another set of morphological operations are applied on I'_{ROI} in the soft segmentation stage followed by binarization and convex-hull transform smoothing steps produced the final segmented image: I_{vessel}, $I_{Optic\ Disc}$, or $I_{exudates}$, depending on the target retinal anatomical structure. The common phases involved in our proposed system are graphically illustrated in Figure 3.3 and detailed in the following subsections.

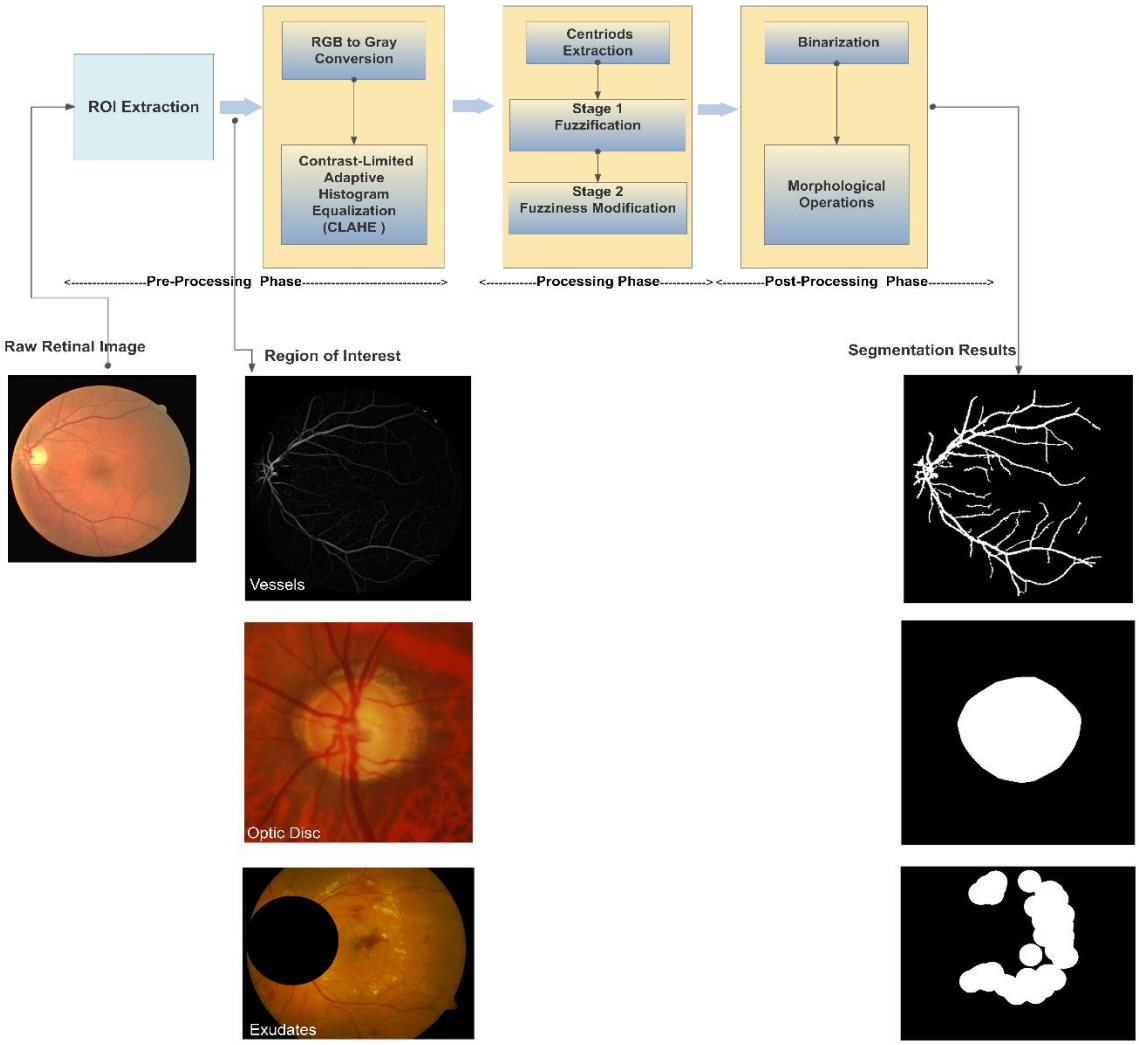

Figure 3.5 Pipeline of proposed hybrid segmentation system.

3.1 Phase I: Image Pre-Processing

The major goal of this phase as it called ROI extraction is to extract the retinal anatomical structure of interest in order to reduce the computational cost and to enhance the overall performance; where a window around the target anatomical structure region of the raw retinal image is extracted, then the pre-processing steps are applied on it.

Each anatomical structure has its own characteristics and features, thus, some of pre-processing steps may be different. However, the pre-processing general framework keep unchanged. Since the pre-processing steps are quite dependent on the challenges created by the nature of target anatomical structure, a brief description of each anatomical structure is presented, followed by the corresponding required pre-processing steps.

3.1.1 Retinal Vessels ROI Extraction

Vessel segmentation in retinal images involves a tension between accurate vascular structure extraction and false responses near sites of pathology or other nonvascular structures such as optic disc or macula. In one hand, this tension arises from the low contrast nature of retinal vessels in comparison to the fundus image background. On the other hand, retinal vasculature structure exhibits dynamic change in size and contrast and broad distributed branching on the whole surface of retinal fundus image. For example, the width of retinal vessels ranges widely, from less than one pixel up to more than five pixels in a typical retinal image, as illustrated in Figure 3.4.

Based on a work proposed by [122], Heneghan *et al.* [123] proposed two stages retina vessels segmentation approach, where they used a set of initial morphological filters to emphasizes the linear structures in first stage.

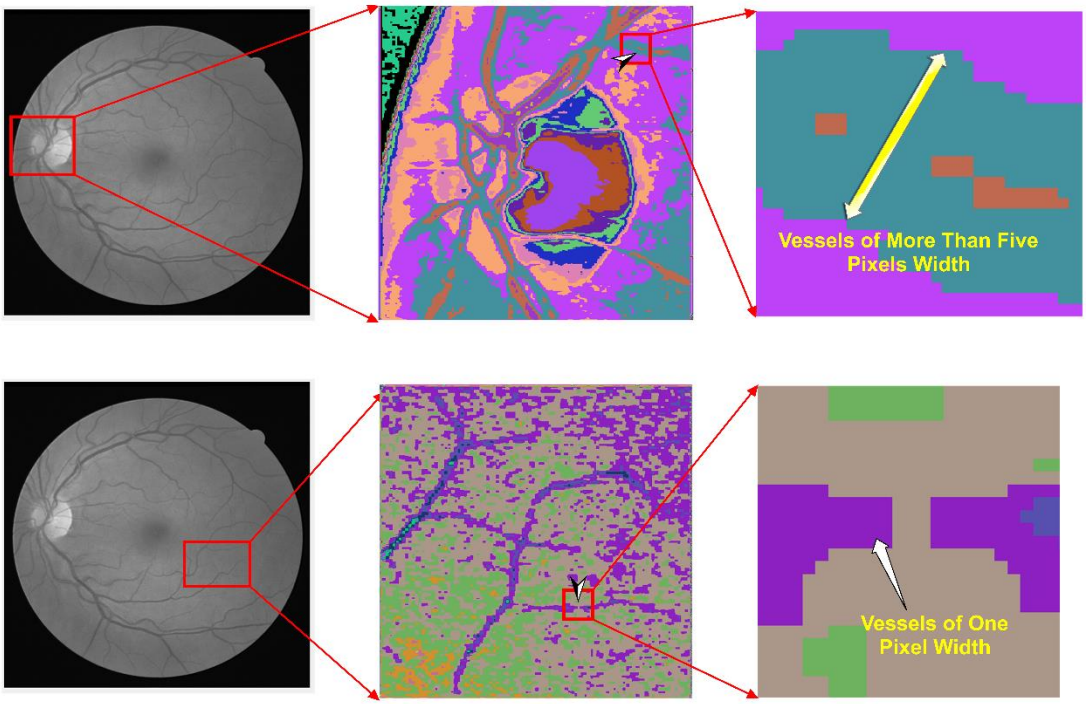

Figure 3.7 Difference in widths between retinal vascular structures.

Additional morphological operations and hysteresis thresholding was used to generates the binary vessel image as a second stage. In our system, we utilize the first stage of this approach to generate our vessels region of interest I_{ROI}^{vessel} as follows.

First, the raw retina image was converted into grayscale through green layer as it presents the higher contrast between vessels and fundus background among other layers as in (3.1):

$$I_{retina}^{G} = \Im^{G}\left(I_{retina}^{RGB}\right) \tag{3.1}$$

where $\Im^{G}(.)$ denotes the green layer extracting operator and I_{retina}^{G} is the green layer of raw RGB fundus image. Then the I_{retina}^{G} image was complemented as a preliminary step for morphological filtering as in (3.2):

$$I_{retina}^{comp} = \Im^{imcomplemment}\left(I_{retina}^{G}\right) \quad (3.2)$$

where $\Im^{imcomplement}$ denotes the image complementing operator and I_{retina}^{comp} is the complement version of I_{retina}^{G}.

The supremum and infimum of morphological openings were performed in aim of generating two images:

- Image with emphasized linear structures represent the vessels tissues.
- Image with homogenous emphasized flat structures represent fundus background and other tissues.

In these operations, the conventional morphological opening was replaced with radial opening as in (3.3):

$$\hat{I}_{retina}^{\alpha} = \alpha\left(I_{retina}^{comp}\right) = \bigvee_{\theta} I_{retina}^{comp} \circ \mathcal{L}_{\theta} \quad (3.3)$$

Where $\circ$ denotes morphological opening and $\bigvee_{\theta}(.)$ denotes supremum operator. $\mathcal{L}_{\theta}$ represents the set of structuring linear segments of $\mathcal{L}$ pixels length and are rotated at multiple angles $\theta \in [0, 2\pi)$. All linear shapes with length greater than or equal to $\mathcal{L}$ should be preserved by at least one rotation θ. By such an operation, all other non-vessel tissues that have not the structuring element at any rotation will not preserved. In our experiments, the value of $\mathcal{L}$ was set to 11 pixels rotated in 12 rotations.

However, morphological opening $\alpha\left(I_{retina}^{comp}\right)$ caused many of filamentary and small vessels to be lost, therefore, a morphological reconstruction was applied afterwards as in (3.4) :

$$I_{retina}^{\alpha} = \Im^{imreconstruct}\left(\hat{I}_{retina}^{\alpha}\right) \quad (3.4)$$

where $\Im^{imreconstruct}$ denotes morphological image reconstructing operator. Image reconstruction can be thought conceptually as a sort of repeated morphological dilations applied on the *marker image* $\hat{I}^{\alpha}_{retina}$ until the contour of the marker image fits under the *mask image* I^{comp}_{retina} where the peaks (highest intensity pixels) spreading out.

Other radial morphological opening was applied on retina image in goal of generating homogenous background does not contain vessels structures as in (3.5):

$$I^{\beta}_{retina} = \beta(I^{comp}_{retina}) = \bigwedge_{\theta} I^{comp}_{retina} \circ \mathcal{L}_{\theta} \tag{3.5}$$

where $\bigwedge_{\theta}(.)$ denotes infimum operator. Unlike to values of $\mathcal{L}_{\theta}$ and θ parameters were set by [123]. In this system, infimum parameters were of same values as of supremum case because the major goal of this stage is to roughly vessels enhancement against background, deep infimum or supremum may affect the quality of vessels appearance in region of interest image which, in turns, reflects in a segmentation performance degradation of proposed processing system.

The target vessel region of interest I^{vessel}_{ROI} was generated by a subtraction operation between I^{β}_{retina} and I^{α}_{retina} as in (3.6)

$$I^{vessel}_{ROI} = I^{\beta}_{retina} - I^{\alpha}_{retina} \tag{3.6}$$

Figure 3.5 shows a closer look for supremum, infimum and resultant subtraction operations applied on fundus image. As can be shown from Figure 3.5, despite of vessel emphasis in I^{vessel}_{ROI}, the issues of vessel segmentation still exist. Many small vessel branches melt in the fundus background. On the other hand, large vessels exhibit multiple gray scaling.

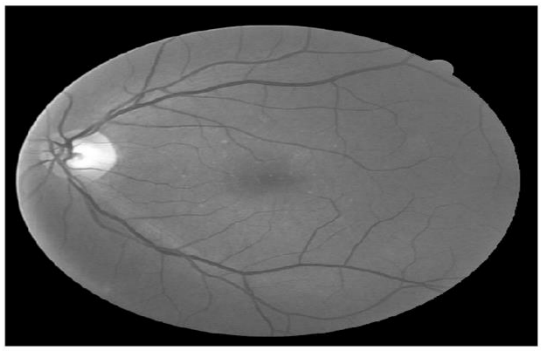

Raw Retina Image

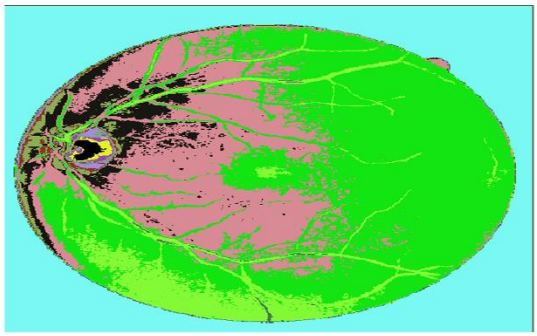

Supremum Result

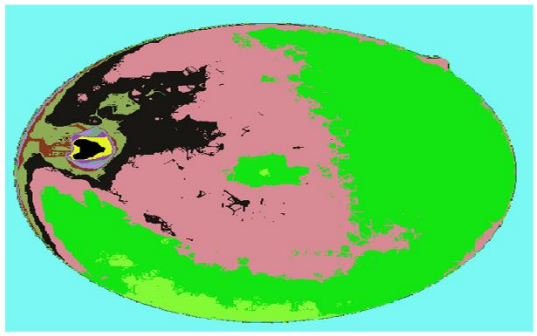

Infemum Result

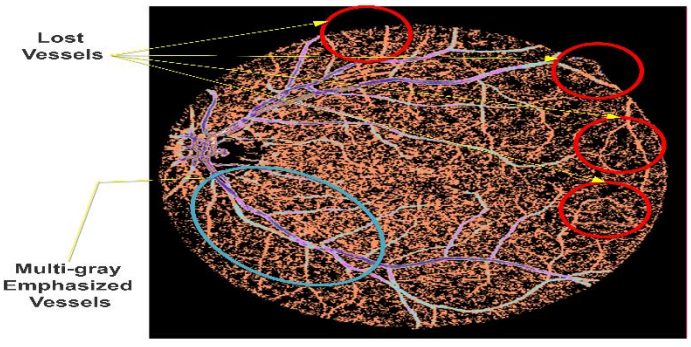

Vessel ROI

Figure 3.9 Output of supremum I_{retina}^{α} , infimum I_{retina}^{β} and I_{ROI}^{vessel} images respectively. All of these images are originally in gray-scale, MATLAB® has been used to substitute colors values instead of gray ones for sake of clarification.

3.1.2 ROI of optic disc

The optic nerve head is defined as the region of the retina where all retinal nerve fibers converge to form the start of the optic nerve [124]. The optic nerve head, or optic disc, is usually round or approximately oval in shape and contains a central brighter region called the cup or pallor. The tissue between the cup and the disc margin is called the neural rim or neuroretina rim, as illustrated in Figure 2.6.

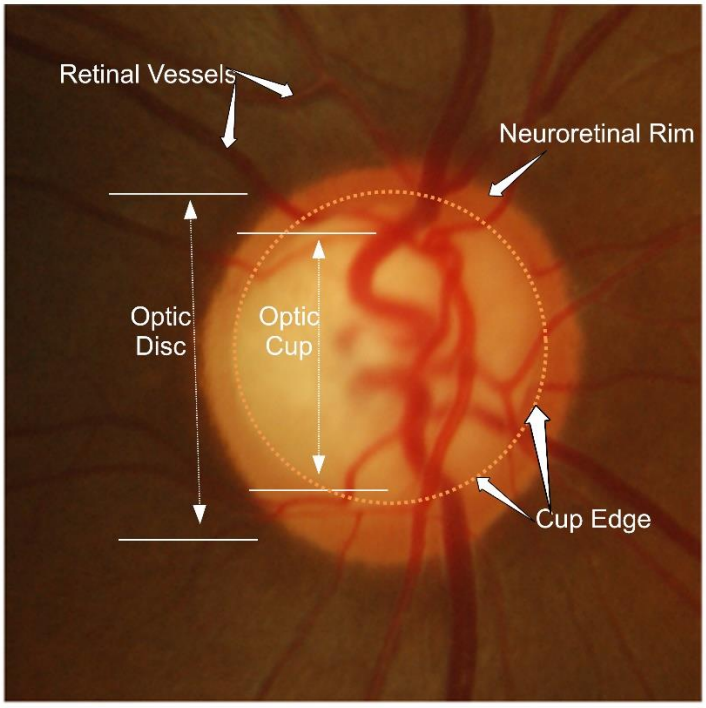

Figure 3.11 Anatomical structure of optic disc.

All optic nerve diseases lead to structural changes in the parapapillary and intrapapillary regions of the optic nerve head. These changes can be described quantitatively by many variables such as shape and size of the optic disc, shape and size of pallor, the ratio of cup and disc diameters, and the ratio of cup and disc areas [125].

To derive these variables, the first step is to extract the optic disc region from the raw retinal image. The optic disc region of interest is almost of rounded shape; therefore, we use the Hough transform to extract the center of the neuroretinal rim of the optic disc, and we subsequently extract the square window around the optic disc, which represents the optic disc region of interest that involves the following steps:

3.1.2.1 Edge detection

Edge detection is often applied as preprocessing step to Hough transform. Therefore, the input image fed into Hough transform is an edge map composed of a set of pixels partially describe the boundaries of optic disc. The efficiency and accuracy of Hough transform in finding the center of optic disc circle can be demonstrated by employing accurate edge detection technique. Fuzzy C-Means (FCM) clustering algorithm was applied for this purpose. Before applying FCM algorithm, retina image underwent a set of preprocessing steps in goal of achieving accurate edge map as following:

First, the red layer of retina image was extracted as in (3.7):

$$I_{retina}^{R} = \Im^{R}\left(I_{retina}^{RGB}\right) \tag{3.7}$$

where $\Im^{R}(.)$ denotes red layer extracting operator. In contrast to vessels extraction, red layer is the layer where optic disc tissues have the higher contrast with other objects on fundus image. Then, I_{retina}^{R} was enhanced as in (3.8) :

$$I_{retina}^{enhanced} = \Im^{CLAHE}\left(I_{retina}^{R}\right) \tag{3.8}$$

where $\Im^{CLAHE}(.)$ denotes the Contrast-Limited Adaptive Histogram Equalization (CLAHE) operator, it locally operates on small data regions of image rather

than the entire area yields contrast-enhanced image. For further enhancement, we apply median filtering of 9×9-sized window and fed as input to FCM algorithm as shown in Figure 3.7. As a first step towards edge map generation is to apply a 25-clusters FCM algorithm on filtered $I_{retina}^{enhanced}$ image with a goal of roughly aggregating OD pixels into

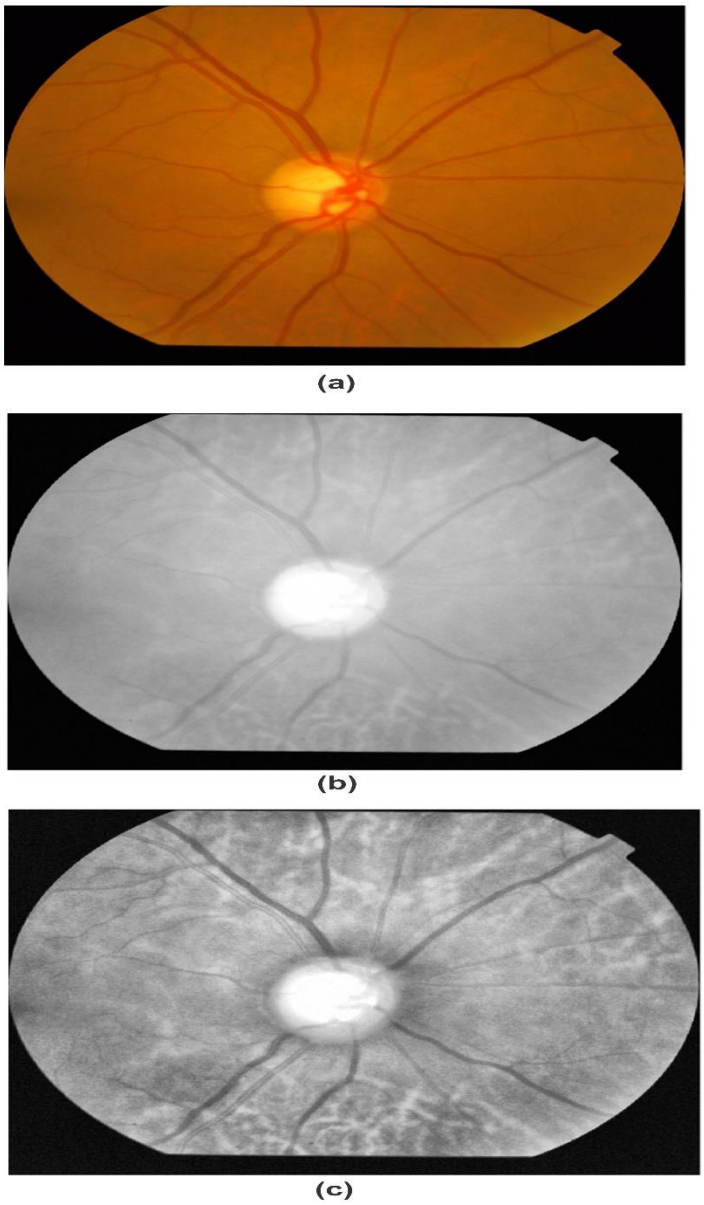

Figure 3.13 (a) Raw retina image. (b) Corresponding red layer I_{retina}^{R}. (c) CLAHE-enhanced image $I_{retina}^{enhanced}$.

one cluster and the other 24 clusters were dedicated for other surrounding tissues. This operation yields a 25-gray scaled image I_{FCM} as shown in Figure 3.8.

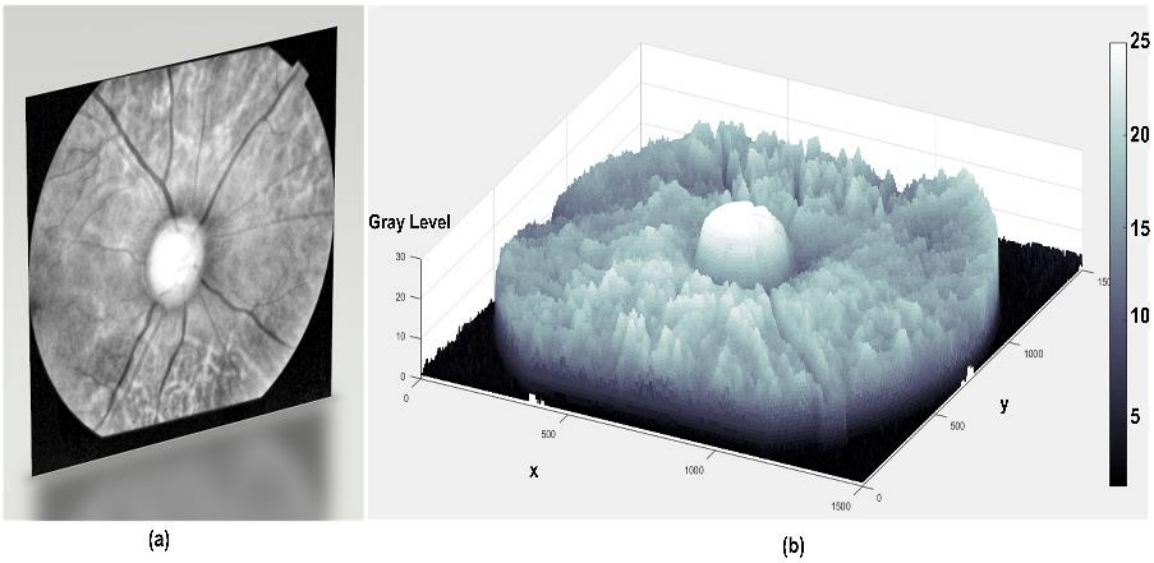

Figure 3.15 (a) Fuzzy c-means output image I_{FCM} for c= 25. (b) corresponding clustered 3D of I_{FCM}image shows a gray level for each cluster (colorbar) where optic disc pixels have c= 25.

The binarized version of I_{FCM} was then obtained via simple thresholding as in (3.9):

$$I_{FCM}^{bw} = \begin{cases} 1, & I_{FCM} = c \\ 0, & Otherwise \end{cases} \quad (3.9)$$

where I_{FCM}^{bw} represents the binarized version of I_{FCM} image setting $c = 25$ clusters. Although the binary image I_{FCM}^{bw} forms the seed for our target edge map, some noises (binarization residuals corresponding to non-optic disc tissues) are likely to be introduced into the result during this process. To solve this, we used a morphological opening of size *P* pixels, which keeps only the connected components (objects) of I_{FCM}^{bw} image whose areas are $\geq P$ and eliminates the rest as illustrated mathematically as follows:

Consider I_{FCM}^{bw} as a union of disjoint connected components as in (3.10)-(3.11):

$$I_{FCM}^{bw} = \bigcup_{i} b_i \qquad (3.10)$$

Then,

$$I_{FCM}^{smoothed} = \alpha\left(I_{FCM}^{bw}\right) = I_{FCM}^{bw} \circ \mathcal{B} \qquad (3.11)$$

where $\mathcal{B}$ denotes disc morphological opening smoother.

Then morphological dilation followed by morphological removal was applied on $I_{FCM}^{smoothed}$ leaving only boundary pixels that define our target edge map image $I_{EdgeMap}$ as elaborated in Figure 3.9.

3.1.2.2 Hough transform

The core idea behind Hough transform (point to curve transform) is that the perpendicular lines to edge point of a circle cross (coincide) in the center of the circle. Thus, if we draw perpendicular lines to every edge pixel of our edge map, then regions of circles centers will appear as bright '*hot spot*' due to accumulative perpendicular lines there. Hough transform can be calculated using different approaches: directional information (gradients), error compensation (smoothing) and voting in parameter space. Since we have only one optic disc per each retina fundus image, our circle-searching problem reduces to one circle. Thus, we use the last approach.

Parametric space voting approach proceeds as follows: Optic disc can be defined as a circle-shaped object in the xy plane of fundus image parametrically specified in (3.12):

$$(x-a)^2 + (y-b)^2 = r^2 \qquad (3.12)$$

where a and b are the coordinates of a candidate circle center corresponds to optic disc circle, and r is the radius. Hough transform is a point $\rightarrow$ curve transform, it is applied on edge pixels (intensities at (x, y) pixel) in order to establish a circle curve.

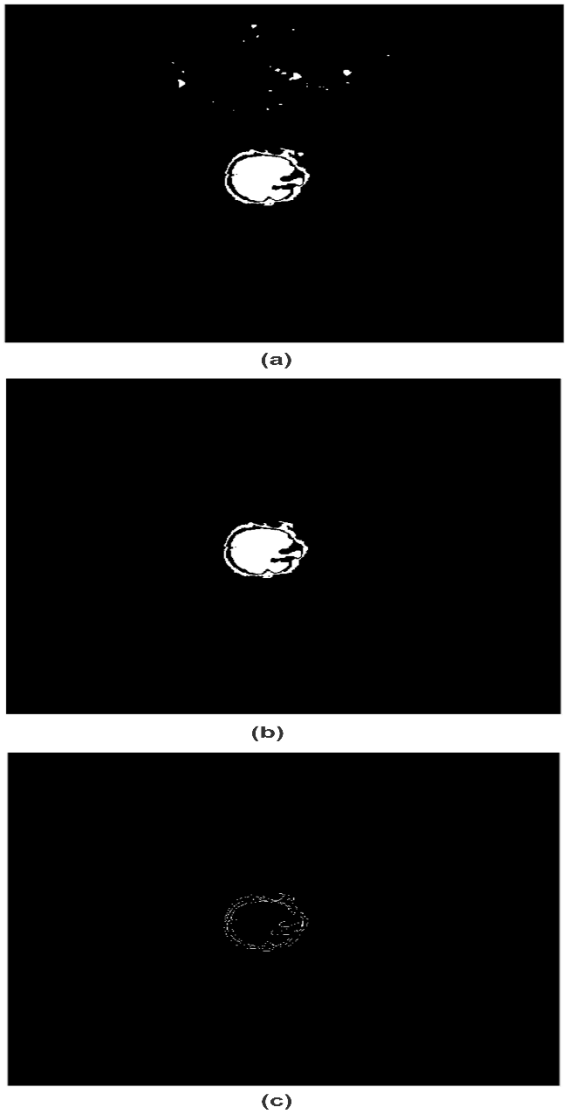

Figure 3.17 (a) Binarized I_{FCM}^{bw} image. (b) $I_{FCM}^{smoothed}$ image. (c) Edge image $I_{EdgeMap}$ after successive steps of dilation and morphological removal filtering.

Edge points yielded by edge detector are considered points lie on the curve of sought-after circle defined in (3.12). For each edge pixel (x, y), a candidate circle of $\hat{r} \in (R_{min}, R_{max})$ can be defined in (3.13) and (3.14).

$$a = \hat{r} \cdot sin(\theta) \qquad \forall\theta \in [0,2\pi] \tag{3.13}$$

$$a = \hat{r} \cdot cos(\theta) \qquad \forall\theta \in [0,2\pi] \tag{3.14}$$

identifying circle curve that best fit edge points proceeds through defining an accumulator array $\mathcal{A}(\hat{r}, \theta)$ as in (3.15).

$$\mathcal{A}(\hat{r}, \theta) = \mathcal{A}(\hat{r}, \theta) + 1 \tag{3.15}$$

In our work, we specified R_{min} and R_{max} to 75 and 85 pixels long respectively; this range corresponds to radii range of candidate circles that are taken into consideration during searching for OD circle. This range may vary from one dataset to another depending on the fundus image resolution, however, it is constant for the one dataset due to uniform nature of optic disc location and size.

A circle curve generated in polar $(\hat{r}, \theta)$ space for each edge pixel (x, y) in cartesian xy plane of retina fundus image. Candidate generated circles intersect in peaks $(\hat{r}, \theta)$ in Hough transform space. Thus, spots with higher brightness (accumulates ones) in places where centers of circles should be found.

Since we have one circle, we have one hot spot ($\max(\mathcal{A}(\hat{r}, \theta))$) corresponds to OD circle as can be illustrated in Figure 3.10.

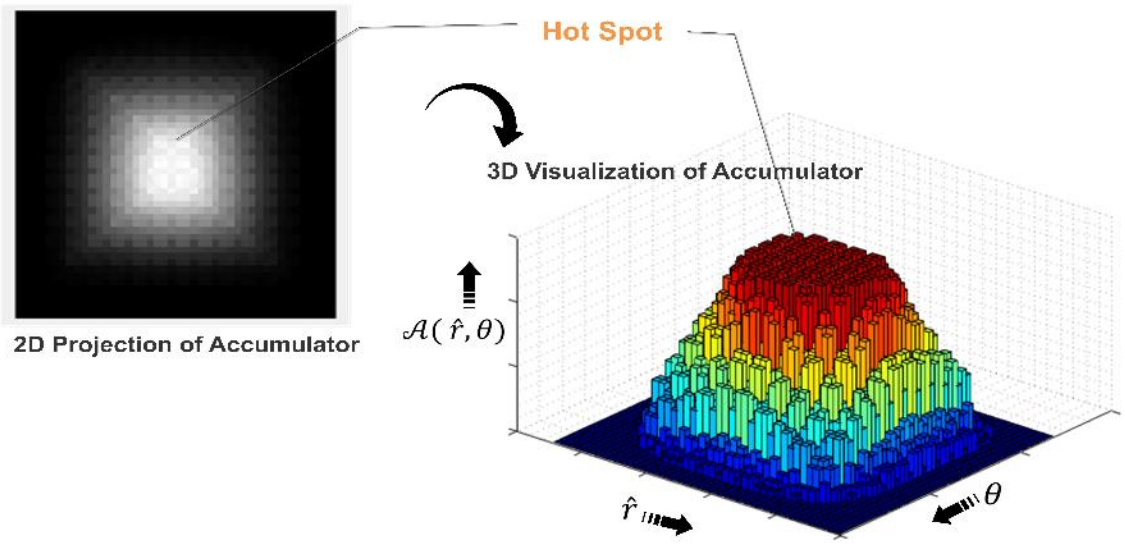

Figure 3.19 Accumulation function A (r^, θ) in 3D view and associated 2D projection where hot spot corresponds to where the centers of circles should be found in 2D view and the maximum accumulation in 3D view.

3.1.2.3 OD ROI window

Since Hough transform detects the coordinates (x_{center} , y_{center}) of optic disc circle, a perfect circle can be synthesized given a radius r.Choosing radius value depends on the validation dataset used; because each dataset produced via fundus camera is of particular specifications in terms of image size and pixel resolution.

Radius value r was used in our system to establish the square widows' borders of optic disc region as it equals = $2 \cdot r$ pixels width. Then, using MATLB ® image cropping function, final I_{ROI}^{OD} image has been extracted as shown in Figure 3.11.

3.1.3 ROI of exudates lesions

One of the major indicators of the presence of diabetic retinopathy is the existence of exudate regions. Figure 3.11.a show a typical example of a color retinal fundus image

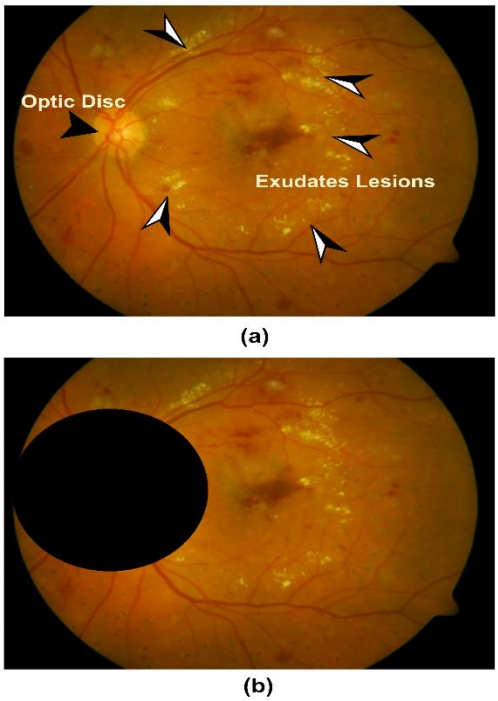

Figure 3.21(a) Raw retina image contains white spots represent hard exudates lesions. (b) Exudates ROI.

for a patient that has different distributed exudate islands along with pixel level annotations made by expert ophthalmologists. As shown in Figure 3.11.a, exudate lesions appear as either white or yellow soft abnormal regions of different sizes, nonuniform shapes and fuzzy divergence on the surface of retinal fundus images. Although retina exudates follow neither uniform sizing nor a uniform intensity distribution, the optic nerve head and bright reflections within empty retinal vessels exhibit a similar appearance. The exudate lesions represent both the most challenging type of retinal lesions to identify and extract and the most challenging of all retinal anatomical structures to segment. The extraction of exudate region of interest follows the same procedure used in optic disc extraction. However, the region of the optic disc is replaced with black region; thus, exudate islands cannot be misclassified as the optic disc region during segmentation phase, as shown in Figure 3.11.b.

3.2 Phase II: Image Processing

This section elaborates the fuzzy theory-dependent coarse segmentation phase of our proposed hybrid system. This phase was inspired by a local fuzzy thresholding open methodology proposed as a general framework by Aja-Fernández *et al.* [126].

This segmentation methodology combines two powerful thresholding techniques: adaptive local thresholding and spatial local information-based thresholding. This phase basically consists of three stages: *fuzzy modeling*, *fuzzy model aggregation* (fuzziness spatial filtering) and *binarization* as illustrated in the following subsections.

3.2.1 Stage I: fuzzy modeling

In this stage, the pixel values (intensities) of our retinal image are converted to fuzzy membership values based on properly defined membership functions. Our fuzzy model was built through four basic steps: image fuzzification, fuzzy sets composition, fuzzy relations (functions) composition and defuzzification.

3.2.1.1 image fuzzification

One can look at image fuzzification as sort of image coding; where the input for this step is I_{ROI} , that can be viewed as composed of fuzzy sets assemblage illustrated in in Figure 3.12, as an example, for optic disc case. Each fuzzy set *A* corresponds to a particular zone of I_{ROI}. For more precise and accurate extraction of target anatomical structure, most of zones were set to belong to the target object (vessels, optic disc and exudates lesions) whereas one zone was used to represent fundus background as shown in Figure 3.12.

Without loss of generality to other anatomical parts, as can be shown in Figure 3.12, the optic disc has multiple intersected zones, most of them represent optic disc, other represent vessels exist in optic disc region and the rest represents background.

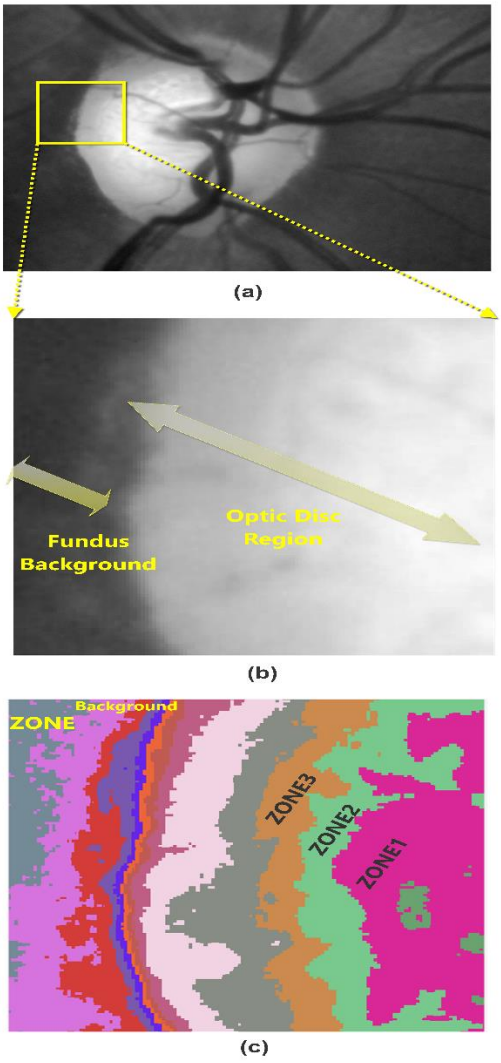

Figure 3.23 Image fuzzification. (optic disc as example) (a) Optic disc ROI. (b) A cropped section of I_{ROI}^{OD} image. (c) The corresponding section of I_{ROI}^{OD} obtained after applying color substitution via MATLAB ®. Note the multiple representative gray levels of optic disc tissues and the interference between them and background tissues.

3.2.1.2 fuzzy sets composition

The entire region of interest I_{ROI} produced in the preprocessing phase represents the universe of discourse U_{ROI} through the process of fuzzy model formulation.

As shown in Figure 3.12, U_{ROI} consists of multiple overlapped zones, each zone defines a fuzzy set $\mathrm{A}_{zone}^{traget}$, where $target$ denotes the target anatomical structure specified in I_{ROI} image which includes: vessel, optic disc and exudates lesion whereas zone denotes the region of pixels belong either to anatomical structure or fundus background.

Therefore, the fuzzy model of our work can be specified mathematically as in (3.16):

Let $$U_{ROI}^{target} = \{ \mathrm{A}_{zone1}^{traget}, \mathrm{A}_{zone2}^{traget}, \cdots, \mathrm{A}_{zone\,n}^{traget} \} \quad (3.16)$$

is the representative universe of discourse of I_{ROI}^{target}. Then, a fuzzy set $\mathrm{A}_{zone}^{traget}$ in U_{ROI}^{target} ($\mathrm{A}_{zone}^{traget} \subset U_{ROI}^{target}$) is defined as set of ordered pairs as in (3.17):

$$\{ (p_i, \mu_{\mathrm{A}}(p_i)) \} \quad (3.17)$$

where i^{th} pixel $p_i \in U_{ROI}^{target}$, μ_{A}: $U_{ROI}^{target} \longrightarrow [0,1]$ is the membership function of μ_{A} and $\mu_{\mathrm{A}}(p) \in [0,1]$ is the degree of membership of p in $\mathrm{A}_{zone}^{traget}$.

Each fuzzy set is identified through a set of characteristic indices (parameters): the support and the core of fuzzy set are graphically illustrated in Figure 3.13 for case of vessel region of interest U_{ROI}^{vessel}. Without loss of generality, irrespective of the target anatomical structure, the support of fuzzy set represents the crisp subset of the set U_{ROI} whose pixels all have non-zero membership grades in the set A_{zone} as in (3.18):

$$Supp(A_{zone}) = \{ p: \mu_{A_{zone}}(p) > 0, p \in U_{ROI} \} \quad (3.18)$$

Where $Supp$ denotes the support of fuzzy set A_{zone}.

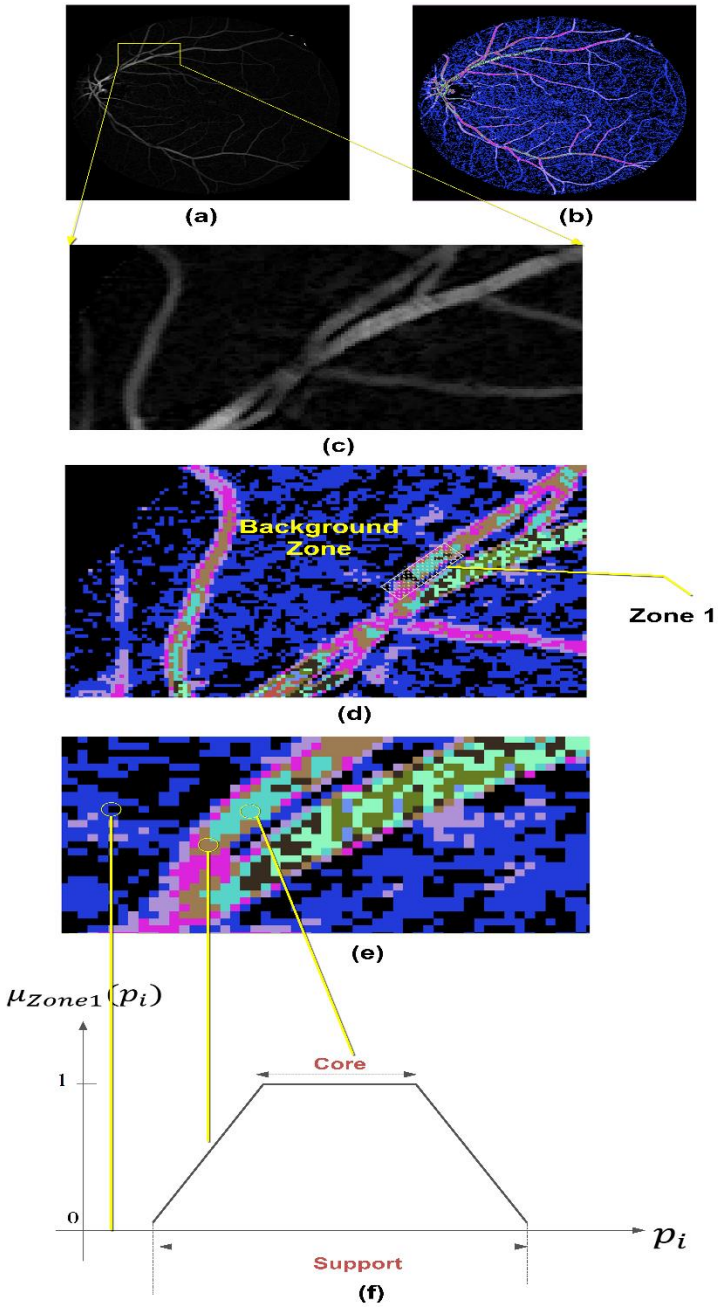

Figure 3.25 (a) Vessel region of interest U_{ROI}^{vessel}. (b) Corresponding color-substituted U_{ROI}^{vessel}. (c) A zoomed section of U_{ROI}^{vessel}. (d) Corresponding color-substituted of (c) shows two zones one corresponds to background and the other for vessel. (e) A zoomed section of vessel zone1. (f) membership function parameters corresponding to vessel zone1.

The core of fuzzy set is the crisp subset of pixels belong to A_{zone} region in the universe of discourse U_{ROI} consisting of all pixels with a membership grade equal to one as in (3.19):

$$Core(A_{zone}) = \{p: \mu_{I_{zone}}(p) = 1, p \in U_{ROI}\} \quad (3.19)$$

where $Core$ denotes the core of fuzzy set A_{zone}.

3.2.1.3 fuzzy relations (functions) composition

In order to compose the mathematical representation of membership functions, we used fuzzy c-means algorithm for sake of generating the cores of representative membership functions through clustering the I_{ROI} into clusters and then centroids of these clusters were extracted and used as initial cores of membership functions, then, the support regions were determined empirically.

The centroids extracted were ordered in ascending manner easing the process of parameters assignment of membership functions and can be expressed mathematically as follows:

The centroids of zones that composed U_{ROI} can be represented as a vector of zones centroids as in (3.20).

$$\boldsymbol{C}_{zone} = [c_{zone}^1, c_{zone}^2, \cdots, c_{zone}^n] \quad (3.20)$$

where c_{zone}^n denotes the centroid of n^{th} zone of U_{ROI}.

The objective function of standard FCM is given as in (3.21) :

$$J_m(U, v) = \sum_{k=1}^{N} \sum_{i=1}^{c} (U_{ik})^m d_{ik} \quad (3.21)$$

where,

U_{ik} : $Fuzzy\ i^{th} partition\ of\ Data\ P, \quad i = 1,2, \ldots N.$

$m : fuzzy\ weighting\ exponent, 1 \leq m \leq \infty$

d_{ik}: $squared\ distance\ between\ k^{th} pixel\ p\ and\ i^{th}\ , centriod$

$where\ d_{ik} = \|p_k - v_i\|^2$

$$v = \begin{bmatrix} v_1 \\ v_2 \\ \vdots \\ v_n \end{bmatrix} : vector\ of\ cluters' centroids.$$

v_i: $centroid\ of\ i^{th}\ cluster$. where v_i for standard FCM is mathematically specified in (3.22):

$$v_i = \sum_{k=1}^{N} \frac{({U_{ik}}^m) p_k}{\sum_{k=1}^{N} ({U_{ik}}^m)} \quad i = 1,2,\cdots,c \tag{3.22}$$

where U_{ik} is given as in (3.23):

$$U_{ik} = \frac{1}{\sum_{j=1}^{c} (\frac{d_{ik}}{d_{jk}})^{2/m-1}} \tag{3.23}$$

However, one disadvantage of the standard FCM is that it requires a large amount of computations if we use it for high number of clustering demand. Therefore, we inspired a histogram-based technique was suggested by [127] for MRI image processing.

This technique deals with all pixels of same intensity value as one pixel then it includes the occurrence frequency in (3.24) as follows:

$$v_i^H = \sum_{k=1}^{N} \frac{({h_k U_{ik})}^m p_k}{\sum_{k=1}^{N} {(h_k U_{ik})}^m} \tag{3.24}$$

where; $h_k = k^{th}\ histogram\ value\ of\ k^{th}\ pixel.$

$H = [h_1, h_2, \cdots h_p]$ h_p : $histogram\ value\ corroponds\ to\ p^{th}\ pixel\ of\ image.$

Since U_{ROI} composed of two major regions: *background* and *target* anatomical object, and the anatomical structure composed of multiple zones we deal with each of it as a fuzzy set A_{zone} belongs to the universe of discourse U_{ROI}. In this system, we used six clusters in the case of vessels and 30 and 40 in the cases of the optic disc and exudates, respectively. The optimum number of centroids is anatomical structure-dependent, and it is tuned to the number that yields optimal performance. Once the centroids are set and extracted, the membership functions are created. Two groups of defined membership functions are created:

- a group of zones used to represent pixels of the target anatomical structure, where each membership function represents one area in the target anatomical structure, leading to a corresponding high-accuracy fuzzy model.
- a group that represents the background, which includes all structures other than structure in the first group.

Thus, for background zone $A_{background}$, we established a separate Z-shaped membership function μ_{BG} dealing with it as specified in (3.25) and depicted in Figure 3.14.

$$\mu_{BG}(p) = \begin{cases} 1, & p \le a \\ 1 - 2\left(\frac{p-a}{b-a}\right)^2, & a \le p \le \frac{a+b}{2} \\ 2\left(\frac{p-a}{b-a}\right)^2, & \frac{a+b}{2} \le p \le b \\ 0, & p \ge b \end{cases} \qquad (3.25)$$

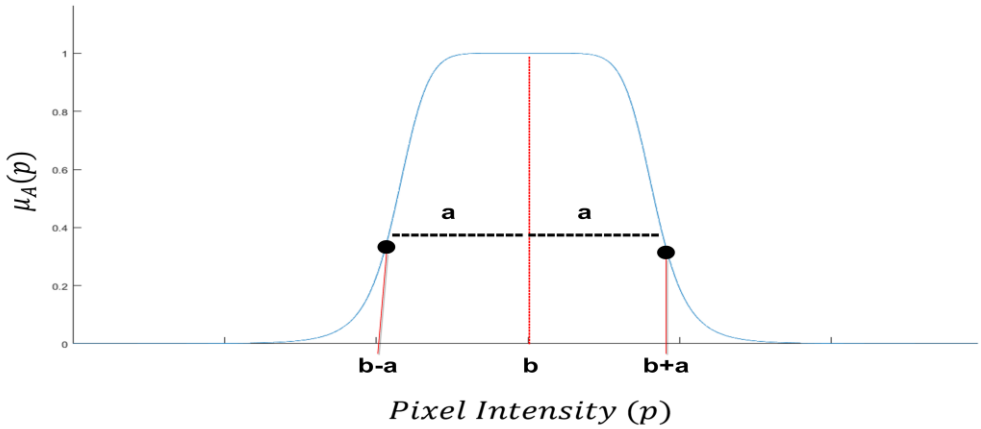

Figure 3.27 Gaussian bell membership function.

As depicted in Figure 3.14, the shape of z-shaped membership function is defined using two parameters a and b; where a parameter specifies the rightmost point at which $\mu_{BG}(p) = 1$ whereas b specifies the leftmost point at which $\mu_{BG}(p) = 0$. At the midpoint between a and b, membership grade $\mu_{BG}\left(\frac{a+b}{2}\right)$ equal to 0.5.

As shown in Figure 3.12 and Figure 3.13, the representative zones of anatomical tissues are of continuous overlapped nature, therefore, we chosen Gaussian functions as representative membership functions for these target zones.

Gaussian function is expressed by the formula as in (3.26).

$$\mu_A(p) = \exp(-(\frac{p-b}{a})^2) \tag{3.26}$$

The shape of Gaussian function as shown in Figure 3.15, sometimes called the Gauss bell, where it is determined by two parameters a and b, where the parameter a determines its width whereas the parameter b determines the modal value of the function. In this system, the centroids that obtained via histogram-based FCM were used as modal parameters whereas a parameter was set using a mathematical relation of the centroids as in (3.27):

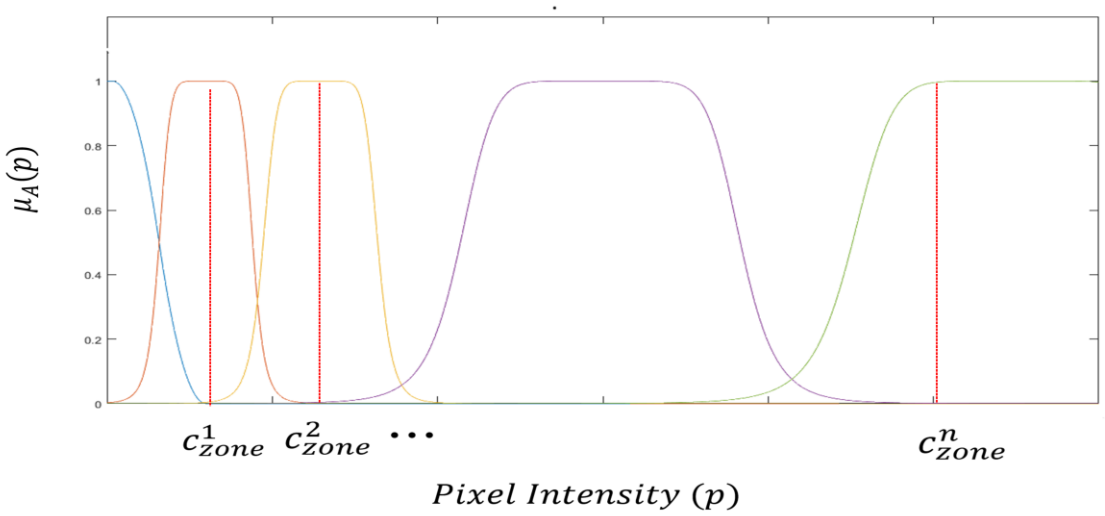

Figure 3.29 Set of Gaussian bell membership functions corresponding to different zones of I_{ROI}^{target} *image.*

$$a = (c^n_{zone} - c^{n-1}_{zone})/2 \qquad (3.27)$$

where c^j_{zone} denotes the centroid of n^{th} zone of U_{ROI} in an ordered centroids vector $\boldsymbol{C}_{zone} = [c^1_{zone}, c^2_{zone}, \cdots, c^n_{zone}]$. Figure 3.15 shows corresponding Gauss bell membership functions that were generated using these parameters. The pixel intensities range that shown in Figure 3.14 and Figure 3.15 is the entire pixels that compose I_{ROI}^{target} image. One membership function was applied at a time yields a fuzzy plane of fuzzy membership values corresponding to pixel intensities as in (3.28):

$$FP_A = \mu_A(p) \qquad p \in I_{ROI}^{target} \qquad (3.28)$$

where FP_A denotes fuzzy plane that generated due to applying $\mu_A(p)$ function on each pixel belongs to I_{ROI}^{target}, where the corresponding fuzzy membership grades of pixels lie outside support region of A_{zone} are set to zero.

In summary, the major objective of fuzzy modeling is to convert pixel intensities into membership values, where each pixel has a vector of membership values of length L, as in (3.29):

$$\overrightarrow{L_p} = [\mu_A^{BGzone}(p), \mu_A^{zone1}(p), \mu_A^{zone2}(p), \cdots, \mu_A^{zonen}(p)] \qquad (3.29)$$

where L_p denotes the vector of corresponding membership values of pixel p in I_{ROI}^{target} image.

3.2.2 Stage II: fuzzy model aggregation

In this stage of processing, the vector of fuzzy membership values that was assigned in (3.29) was modified based on spatial filters applied on each fuzzy plane FP_A defined in (3.28). The basic idea behind this stage is instead of applying spatial filters on pixel intensities (image space), rather they are used on the corresponding membership values (fuzzy membership space) as mathematically assigned in (3.30).

$$\acute{FP}_A = \Im^h\,(\,\mu_A(p)\,), \quad p \in I_{ROI}^{target} \qquad (3.30)$$

where $\acute{FP}_A$ represent the modified version of FP_A generated due to applying special filter of kernel h operates on the neighborhood of membership degrees $\mu_A(p)$ at pixel location (x, y) of I_{ROI}^{target}. Different filtering kernels can be used based on the nature of target anatomical structure. In our system, we used median filter in case of vessels and exudates structures as in (3.31):

$$\acute{FP}_A(x_i, y_i) = median^{\mu_i}_{(S,\mu_i)\in S_{xy}}\{FP_A(S, \mu_i)\,\} \qquad (3.31)$$

where $median^{\mu_i}_{(S,\mu_i)\in S_{xy}}$ denotes to median filter operator on a set of coordinates in a rectangular subplan window S_{xy} forms the neighborhood of a reference membership value μ_i located at (x_i, y_i) of fuzzy plane FP_A.

The output $\acute{FP}_A$ is based on ordering (ranking) the membership values in a sub-window of FP_A plane; where it replaces the value of membership μ_i by the median of membership values in the neighborhood S_{xy} of that value. In our system, the size of S_{xy} window was set to 3×3.

Since optic disc occupies a large region of ambiguous boundaries and divided by large vessels, we used linear filtering instead of median one, where we replaced each membership value μ_i belongs to FP_A plane by a linear combination of its neighbors using the cross-correlation specified in (3.32):

$$\acute{FP}_A = \boldsymbol{H} \otimes FP_A \qquad (3.32)$$

where $\otimes$ denotes the cross-correlation operation with 3×3-size kernel $\boldsymbol{H}$ specified in (3.33):

$$\boldsymbol{H} = \frac{1}{\vartheta}\begin{bmatrix} 0 & 1 & 0 \\ 1 & 1 & 1 \\ 0 & 1 & 0 \end{bmatrix} \qquad (3.33)$$

Therefore, the cross-correlation can be detailed as in (3.34):

$$\acute{FP}^{t}_{\mu_i(x_i,y_i)} = \sum_{u=-k}^{k}\sum_{v=-k}^{k} \boldsymbol{H}(u,v)\, FP(x+u, y+v) \qquad (3.34)$$

In this system, we set ϑ to 5 and k was set to 1. By this filtering modification of fuzzy membership values, each pixel has a modified vector of membership values of length L, as in (3.35):

$$\overrightarrow{L_p'} = [\mu_A^{BG\acute{z}one}(p), \mu_A^{z\acute{o}ne1}(p), \mu_A^{z\acute{o}ne2}(p), \cdots, \mu_A^{z\acute{o}nen}(p)] \quad (3.35)$$

where $\overrightarrow{L_p'}$ denotes the vector of corresponding modified membership values of pixel p in I_{ROI}^{target} image. As a defuzzification step, in order to obtain the output classified version of our filtered fuzzy model, *Last of Maxima* method was used in this system. This method assumes the greatest value of $\overrightarrow{L_p'}$ vector corresponding to the maximal grade of membership values of pixel p to be the crisp class representative of fuzzy model. Therefore, the output image is a gray image with gray scales equal to the number of involved membership functions as shown in Figure 3.16, for vessel segmentation results as an example.

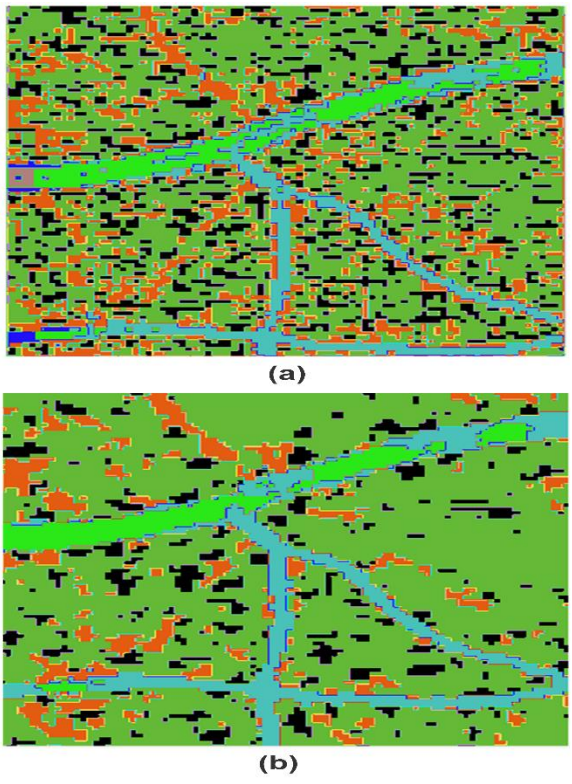

Figure 3.31 Comparison between fuzzy model and filtered fuzzy model outputs for case of vessels extraction (use seven membership functions). (a) Output of fuzzy model. (b) Output of aggregated (spatial filtered) fuzzy model.

3.3 Phase III: Image Post-Processing

The final phase of our proposed hybrid system is post-processing or soft segmentation, which comprises binarization, morphological post-processing and smoothing steps. The coarsely segmented output of stage II undergoes binarization through binary thresholding with empirical thresholds according to target anatomical structure, which yields the semi-final accurately segmented structure. The binarization step produces many isolated, misclassified, and artificial pixels. Thus, it is followed by morphological opening operations for sake of cleansing.

As with other morphological operators, the exact opening operators are determined by specifying a structuring element according to the target retinal anatomical structure. The morphological operator preserves the foreground pixels of the anatomical structure region that have a similar shape to the structure element while eliminating all other unwanted pixels (or artifacts). In the case of retinal vasculature extraction, the basic task of morphological opening is to remove a subset of the foreground (vessel) pixels from the edges of the foreground region, producing a smooth region (vessel) edge as shown in Figure 3.17.

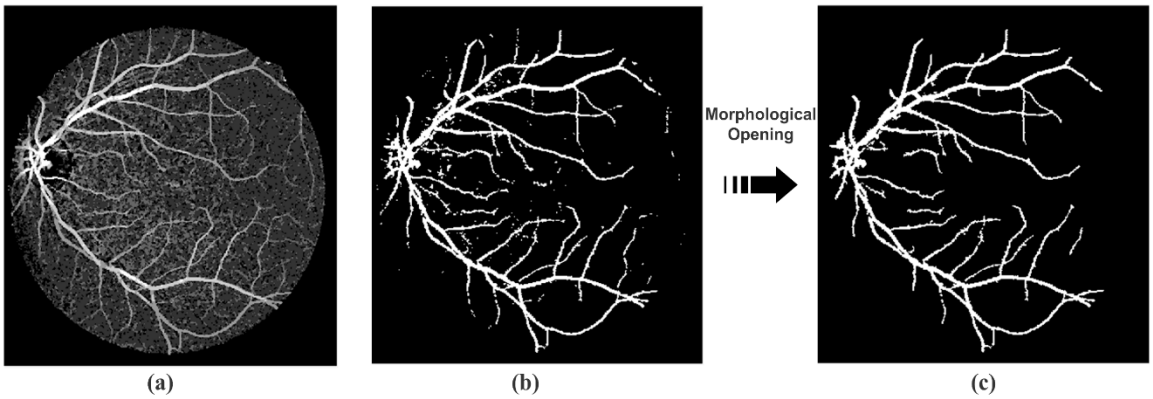

Figure 3.33 Post-processing steps involved in retinal vessels segmentation. (a) Output of processing stage. (b) Binarized output. (c) Morphological operations.

In the case of optic disc and exudate lesion extraction, further steps besides those used in the case of vasculature structure are needed: morphological dilation operations are followed by a convex hull transform to obtain the smooth round shape of the optic disc and the clean, smooth version of the exudate islands, as shown in Figure 3.18 and Figure 3.19, respectively.

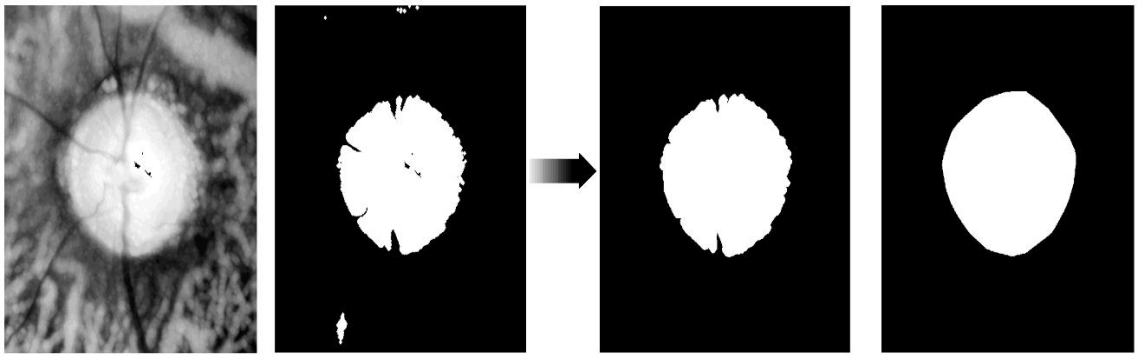

Figure 3.35 Post-processing steps involved in optic disc segmentation. (a) Output of processing stage. (b) Binarized output. (c) Morphological operations. (d) Convex-hull transform

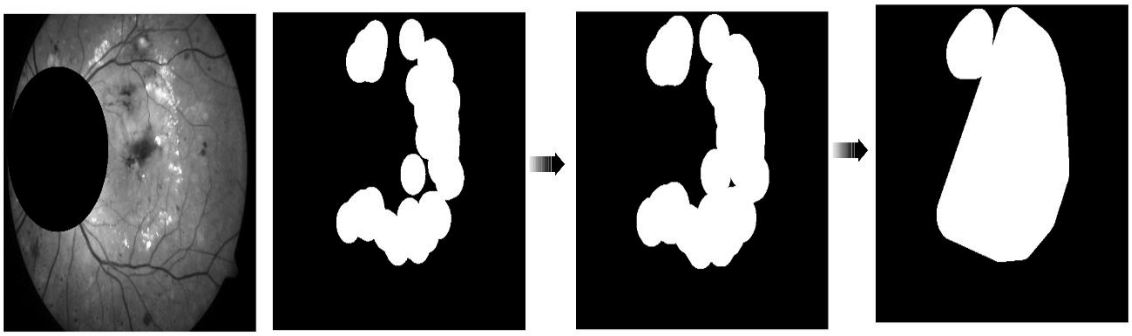

Figure 3.37 Post-processing steps involved in retinal exudates lesions detection. (a) Output of processing stage. (b) Binarized output. (c) Morphological operations.

CHAPTER 4: EXPERIMENTAL RESULTS

In this chapter, qualitative and quantitative results of the proposed hybrid system are presented to demonstrate the robustness of our proposed system in handling heterogenous anatomical structures with different features. As mentioned previously, our proposed system is inspired by open soft fuzzy segmentation methodology [126]. However, Aja-Fernández et. al. proposed and implemented that methodology for extracting wide regions such as the liver and bones depending only on fuzzy set theory. Our proposed system significantly modified the methodology into detection system for clinical purposes by combining mathematical morphology with the modified clustering fuzzy c-means and fuzzy set theory in order to equally accommodate thin and wide retinal anatomical structures based on stand-alone core algorithm.

In this chapter, our system results for each anatomical structure are compared to separate benchmark methods and systems. We report the results of experiments conducted using our proposed subsystems (vessel extraction, optic disc extraction, and exudate extraction subsystems) and compare them with existing up-to-date techniques and methodologies.

4.1 Retinal Vessels Segmentation Results

The ability of our system to extract retinal vasculature structures is evaluated in terms of three major metrics: average sensitivity, average specificity and average accuracy [128, 129]. Sensitivity reflects the ability of the system to detect vessel pixels, while specificity assesses the ability of the system to detect non-vessel pixels.

Sensitivity and specificity represent features of the system and are associated with accuracy as indicated in (4.1(4.3):

$$Sensitivity = T_p/(T_p + F_N) \quad (4.1)$$

$$\text{Specificity} = T_N/(T_N + F_p) \quad (4.2)$$

$$Accuracy = (T_p + T_N)/(T_p + F_N + F_N + T_N) \quad (4.3)$$

Where T_p (True Positives), F_p (False Positives), F_N (False Negatives), and T_N (True Negatives).

In the case of retinal vasculature structures, we have used the most popular datasets in this field: (1) Digital Retinal Images for Vessel Extraction (DRIVE) [31, 32] and (2) STructured Analysis of the Retina (STARE) [33]. Both datasets are well-regarded and popular in the field of retinal vessel segmentation, and almost every study involving vessel segmentation evaluates performance using these datasets.

The popularity of these datasets is due to the good resolution of the retinal fundus images and to the availability of manually labelled ground truth images prepared by two experts. The DRIVE dataset consists of 40 retinal images were evenly divided into a training set and a test set whereas the STARE dataset consists of 20 images, 10 of which are normal retinal images and the other 10 images are abnormal ones. Figure 4.1 shows a typical example of segmentation results.

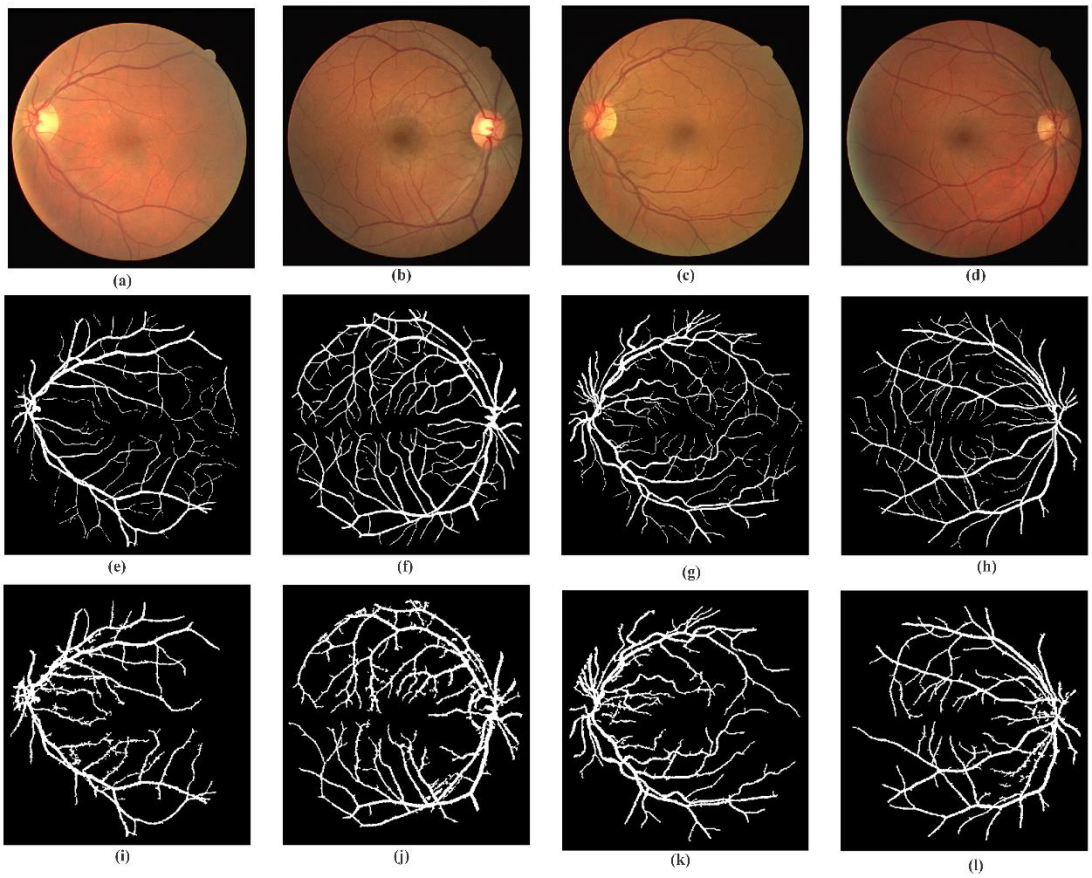

Figure 4.1 Illustration of proposed algorithm on the dataset DRIVE. (a) and (b) Original retina image from DRIVE training dataset. (c) and (d) Original retina images from DRIVE testing set. (e) and (f) Corresponding ground truth. (g) Corresponding 1st observer ground truth. (h) Corresponding 2nd observer ground truth. (i), (j) and (k) Vessels segmentation results of our system.

As shown in Figure 4.1, in addition to extracting wide veins and arteries (vessels with wide area or wide diameter), our proposed system successfully extracted the capillaries (tiny vessels) as well. Although our proposed system was not built on a supervised algorithm, in general, it is fuzzy logic-dependent and thus utilizes labeled images to create the membership function appropriate to the target anatomical structure. Therefore, the best method to examine the detection system's dependence on the training dataset is to use the testing subset of the DRIVE dataset to measure system performance; The detection performance is evaluated and summarized in Table 4.1.

Table 4.1 Performance of proposed vessel segmentation system on the DRIVE dataset.

Dataset	Sensitivity	Specificity	Accuracy
DRIVE / Training	0.7544	0.9714	0.9523
DRIVE / Testing 1st Observer	0.7822	0.9725	0.9556
DRIVE / Testing 2nd Observer	0.8065	0.9729	0.9588

As can be concluded from Table 4.1, our proposed system has achieved enhanced segmentation results against the first and second observers of the DRIVE testing dataset; these results reflect the robustness and reliability of the system for real-life diagnostic implementations.

For further quantitative validation of the proposed system in vessel extraction, the system is applied to the STARE dataset, which is considered a more challenging dataset than DRIVE due to pathological images that have. As in the case of the DRIVE dataset, the STARE dataset has two corresponding ground truths from expert ophthalmologists: one provided by Dr. Valentina Kouznetsova (1^{st} observer). The other ground truth is provided by Dr. Adam Hoover (2^{nd} observer). Figure 4.2 shows example pathological retinal images taken from the STARE dataset and processed by our proposed system

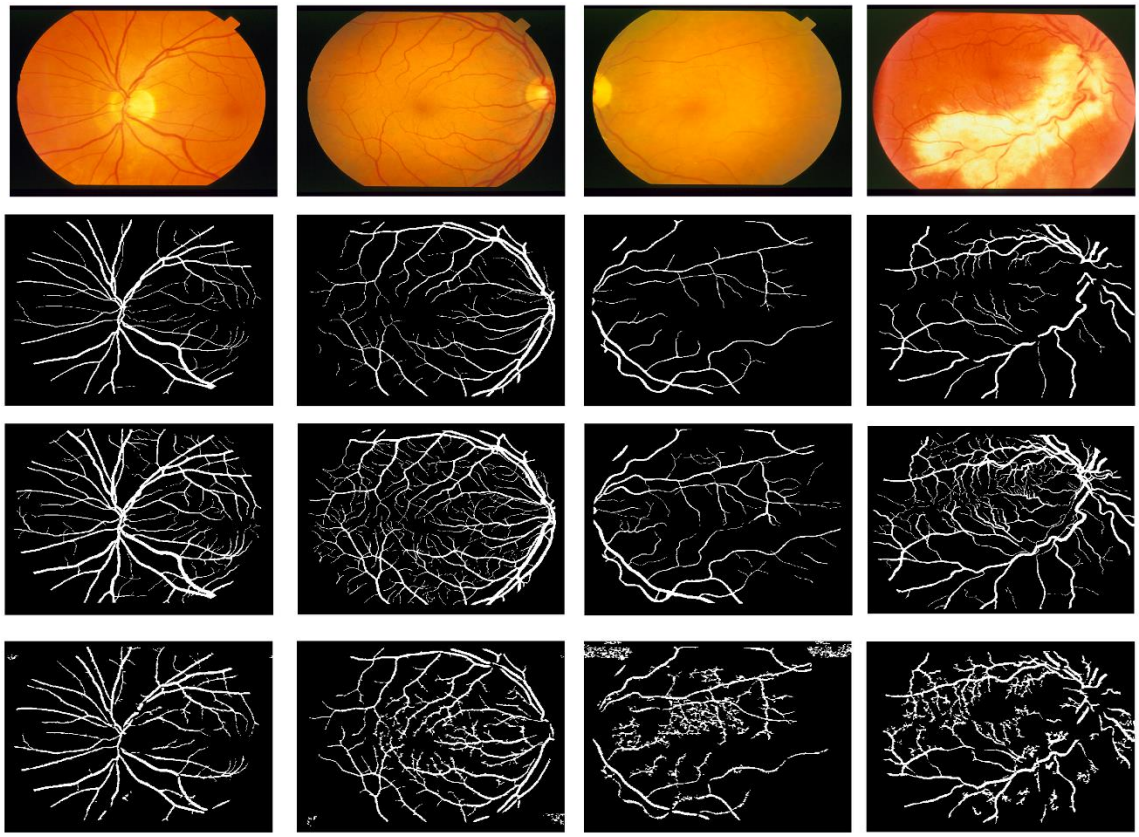

Figure 4.3 Vessels Segmentation results using STARE dataset. Row 1: Original abnormal retina images. Row 2: Corresponding ground truth images prepared by Dr. Valentina Kouznetsova (1st observer). Row 3: Corresponding ground truth images prepared by Dr. Adam Hoover (2nd Observer). Row 4: Corresponding vessel segmentation results of proposed system.

along with the corresponding segmentation results. Table 4.2 summarizes the resulting average accuracy, sensitivity and specificity of the proposed system against the 1st observer and 2nd observer ground truths of the STARE dataset.

Table 4.2 Performance of proposed vessel detection system on the STARE dataset.

Dataset	Sensitivity	Specificity	Accuracy
STARE / 1st Observer	0.6393	0.9646	0.9281
STARE/ 2nd Observer	0.7611	0.9551	0.9402

The high performance achieved on this dataset, as shown in Table 4.2 and Figure 4.2, reveals the proposed system's ability to deal with both normal and abnormal cases encountered in real world clinical applications.

To compare different retinal vessel segmentation techniques and other set of state-of-art methods, Table 4.3 and Table 4.4 and compares our proposed system with other methods [33, 42, 51, 67, 88, 115, 130-137] published based on both DRIVE and STARE datasets.

Table 4.3 Performance comparison of proposed vessel segmentation methods based on DRIVE dataset.

Method	Sensitivity	Specificity	Accuracy
Human Second Observer	0.7761	0.9725	0.9473
Zhang *et al.* (2010) [51]	0.7120	0.0276	0.9382
Dizdaro *et al.* (2012) [138]	0.7181	0.9743	0.9412
Akhavan *et al.* (2014) [115]	0.7252	0.9733	0.9513
Zhang *et al.* (2015) [130]	0.7508	0.9656	0.9521
Borges *et al.* (2015) [132]	-	-	0.9489
Zhang *et al.* (2015) [137]	0.7812	0.9668	0.9504
Singh *et al.* (2016) [42]	0.7594	0.0292	0.9522
Geetha Ramani *et al. (2016)* [131]	0.7079	0.9778	0.9536
Mapayi *et al.* (2016) [133]	0.7302	0.9651	0.9444
Jiang *et al.* (2017) [67]	0.9159	0.9559	0.9538
Proposed System	**0.8065**	**0.9729**	**0.9588**

Table 4.4 Performance comparison of proposed vessel segmentation methods based on STARE dataset.

Method	Sensitivity	Specificity	Accuracy
Hoover *et al.* (2000) [33]	0.6747	0.9565	0.9275
Kande *et al.* (2008) [134]	-	-	0.8976
Zhang *et al.* (2009) [135]	0.7373	0.0264	0.9087
Yin *et al.* (2015) [136]	0.8541	0.9419	0.9325
Singh *et al.* (2016) [42]	0.7939	0.0624	0.9270
Proposed System	**0.7611**	**0.9551**	**0.9402**

Measures in Table 4.3 and Table 4.4 show that our system outperforms most of the up-to-date vessel segmentation methods reported in these tables. The most competitive alternative to our proposed work is the morphology-based global thresholding algorithm developed by Jiang *et al.* [67], whose sensitivity is better than ours. Nonetheless, our proposed technique excels this work in terms of both specificity and accuracy. Additionally, our system is designed to be multitargeted, which further distinguishes its performance.

4.2 Optic Disc Segmentation Results

Optic disc segmentation is less challenging than retinal vessel segmentation because the area occupied by the optic disc is larger than the narrow-branched area occupied by vessels or nonuniform distributed islands occupied by exudate lesions. However, large vessels pass through the optic disc area and separate it into neighbor islands. Additionally, the existence of the cup region inside the optic disc region, the gradual decrease in pixel intensity from the center of the optic disc to the outer rim and its return to high intensity make accurate optic disc region extraction a challenging

segmentation task. For same reasons mentioned for using DRIVE and STARE datasets; optic disc subsystem is validated using the public DRISHTI-GS dataset [139], which contains retinal fundus images for 50 patients using a 30 degree field of view (FOV) at a resolution of 2896 x 1944 pixels. Each retinal image has corresponding manual markings prepared by four ophthalmologists with different levels of clinical experience (3, 5, 9, and 20 years) called a softmap.

To conduct performance evaluation, the gray-scale softmap image must first be converted into a binary image. The conversion process follows classic binary thresholding steps using thresholding levels called confidence levels, where each confidence level corresponds to one of the ophthalmologists involved.

In the following results, we show results based on a fusion of annotations using the normalized average approach, which is considered one of the most reliable approaches. The normalized average of the annotations provides a linear confidence scale in the range (0,1). The proposed system correctly identified the optic disc location with 100% accuracy.

Thus, it produces better accuracy in optic disc localization than other methods. For example, the method of [140] achieved an 89% success rate for localization of the optic disc, testing their methods on a different dataset.

For quantitative evaluation of optic disc segmentation, we have employed the same measures used by the dataset builders [139]: precision, recall, and the harmonic mean of the precision and recall, i.e., the F-score. These error metrics are given mathematically specified in (4.4 (4.6):

$$Precision = T_p/(T_p + F_p) \quad (4.4)$$

$$\text{Recall } = T_p/(T_p + F_N) \quad (4.5)$$

$$Fscore = (2 * Precision * Recall)/(Precision + Recall) \quad (4.6)$$

Where F-score range is between 0 and 1; as $Fscore$ value gets close to 1, the performance gets better.

Comparative analysis of optic disc detection results of the proposed system and other up-to-date techniques[141-144] are provided in Table 4.5 and a typical illustration of optic disc segmentation results for the proposed system is shown in Figure 4.3.

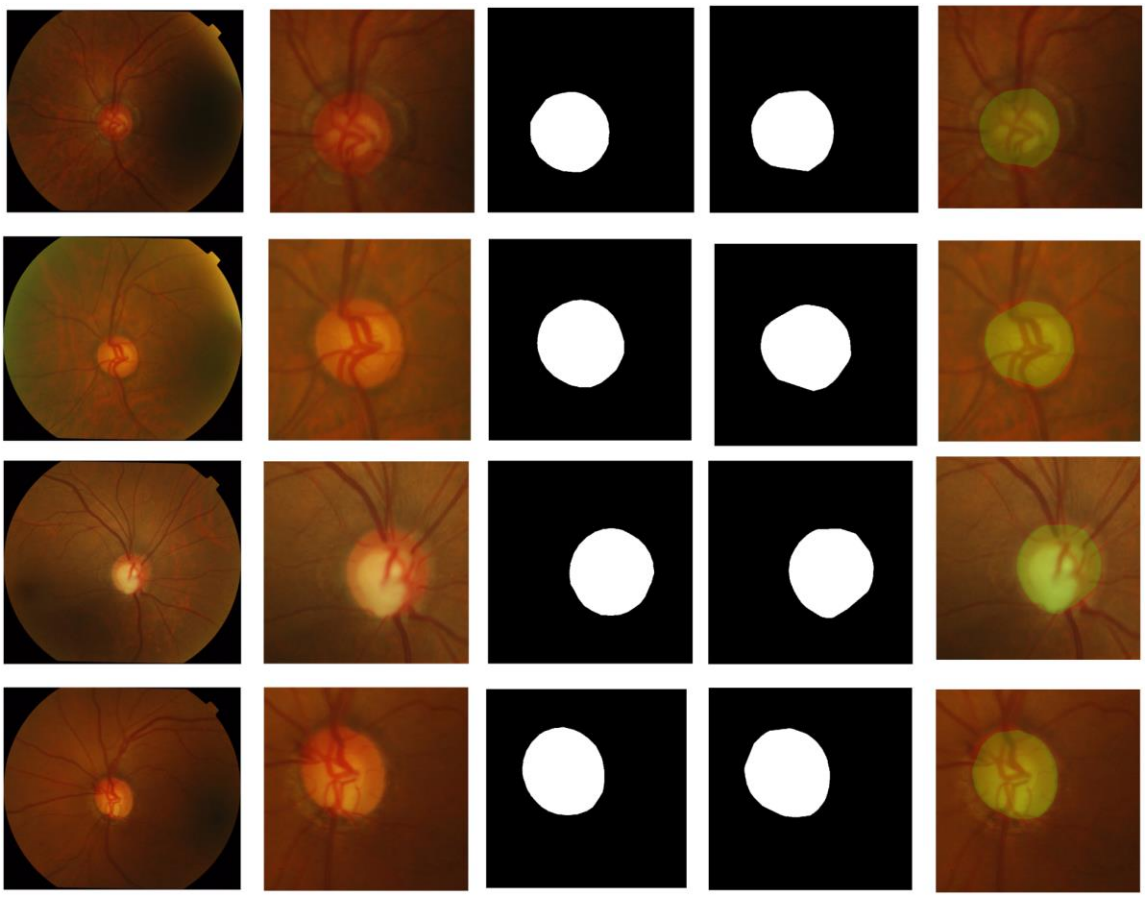

Figure 4.5 Optic disc segmentation results for the DRISHTI-DS dataset. Column 1: Original retinal images. Column 2: Region of interest. Column 3: Corresponding ground truths. Column 4: Optic disc segmentation results of our proposed system. Column 5: Superimposed

Table 4.5 Performance comparison of optic disc segmentation methods on DRISHTI-GS dataset.

Method†	F-Score
Wong *et al.* (2008) [143]	91.1%
Cheng *et al.* (2013) [141]	92.1%
Sedai *et al.* (2016) [142]	95.00%
Zilly *et al.* (2017) [144]	97.3%
Proposed System	**90.2%**

† The results of methods [143] and [141] are taken from the benchmark study [144].

further evaluation of the proposed system, we compare segmentation results for the proposed system with existing methods [134, 145-148] in terms of average specificity, sensitivity and Positive Predictive Value (PPV) as shown in Table 4.6, where sensitivity and specificity were defined in (4.1) and (4.2) and PPV value is represented mathematically as in (4.7):

$$\text{PPV} = T_p/(T_p + F_p) \qquad (4.7)$$

Table 4.6 Optic disc segmentation methods comparison.

Method†	Sensitivity	Specificity	PPV
Stapor *et al.* (2004) [148]	84.98%	99.64%	80.34%
Seo *et al.* (2004) [147]	61.03%	99.87%	88.78%
Lupascu *et al.* (2008) [146]	68.48%	99.69%	81.17%
Kande *et al.* (2008) [134]	88.08%	98.78%	54.48%
Bharkad *et al.* (2017) [145]	74.60%	99.61%	74.96%
Proposed System	**93.13%**	**97.09%**	**90.15%**

†The results of other methods are taken from the benchmark study [145].

‡ PPV: Positive predictive value.

In terms of optic disc segmentation, sensitivity indicates the portion of the real optic disc area that was segmented by the system. Higher values of sensitivity indicate better performance, whereas specificity indicates the portion of the non-optic disc area segmented by system. Higher values of specificity represent better performance. *PPV* indicates the portion of true optic disc area detected by the algorithm.

It is important to note here that not all of the systems listed in Table 4.6 were assessed on the same dataset; the purpose of including these comparisons is to show that the proposed system outperformed these techniques in terms of sensitivity and PPV value while achieving nearly identical specificity. In addition to the performance evaluations listed in Table 4.5 and Table 4.6 our proposed method has achieved an optic disc segmentation accuracy reached up to 96.42%.

4.3 Retinal exudates Segmentation Results

In this section, the success of our proposed compact system in identifying and extracting retinal exudate lesions is evaluated and compared with a set of up-to-date methods. For this purpose, we have used the DiaRetDB1 dataset [27] at the image level. This dataset consists of 89 color fundus images taken in Kuopio University Hospital, of which 84 pathological images contained different types of diabetic retinopathy abnormalities; other images were normal, according to four experts involved in the diagnostic process.

Our exudate segmentation result is evaluated against the expert ground truth of DiaRetDB1 dataset images. However, the expert ground truth is given as a 4-level grayscale image, one gray-level for each expert's markings.

Therefore, as in the case of the optic disc, we combined four experts' annotations in one binary image in a layered manner, as illustrated in Figure 4.4.

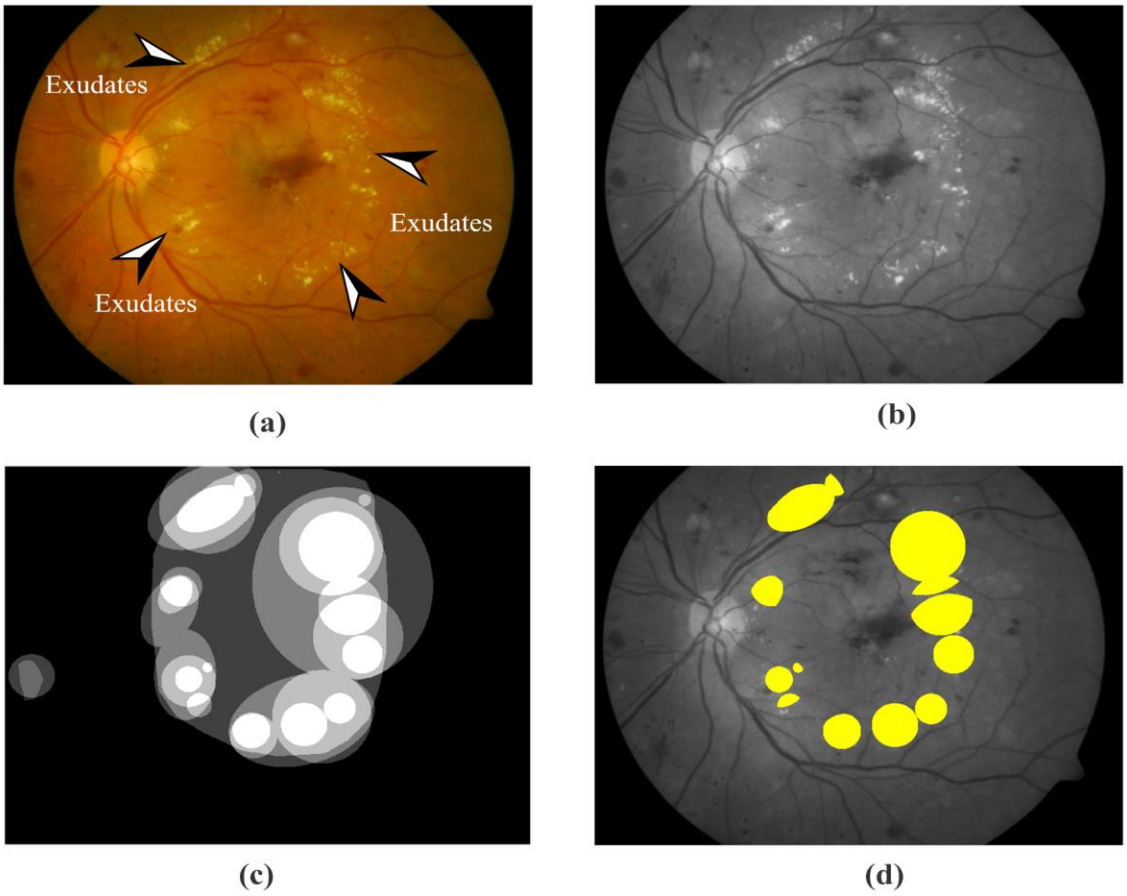

Figure 4.7 (a) Original abnormal retina image from DiaRetDB1 dataset. (b) Gray layer of retina image. (c) Corresponding ground truth; a gray level for each expert annotation. (d) Normalized average of annotations.

pathological images contained different types of diabetic retinopathy abnormalities; other images were normal, according to four experts involved in the diagnostic process. Our exudate segmentation result is evaluated against the expert ground truth of DiaRetDB1 dataset images. However, the expert ground truth is given as a 4-level grayscale image, one gray-level for each expert's markings.

Therefore, as in the case of the optic disc, we combined four experts' annotations in one binary image in a layered manner, as illustrated in Figure 4.4. A Typical example of segmentation results of exudates detection subsystem based on DiaRetDB1 dataset is shown in Figure 4.5.

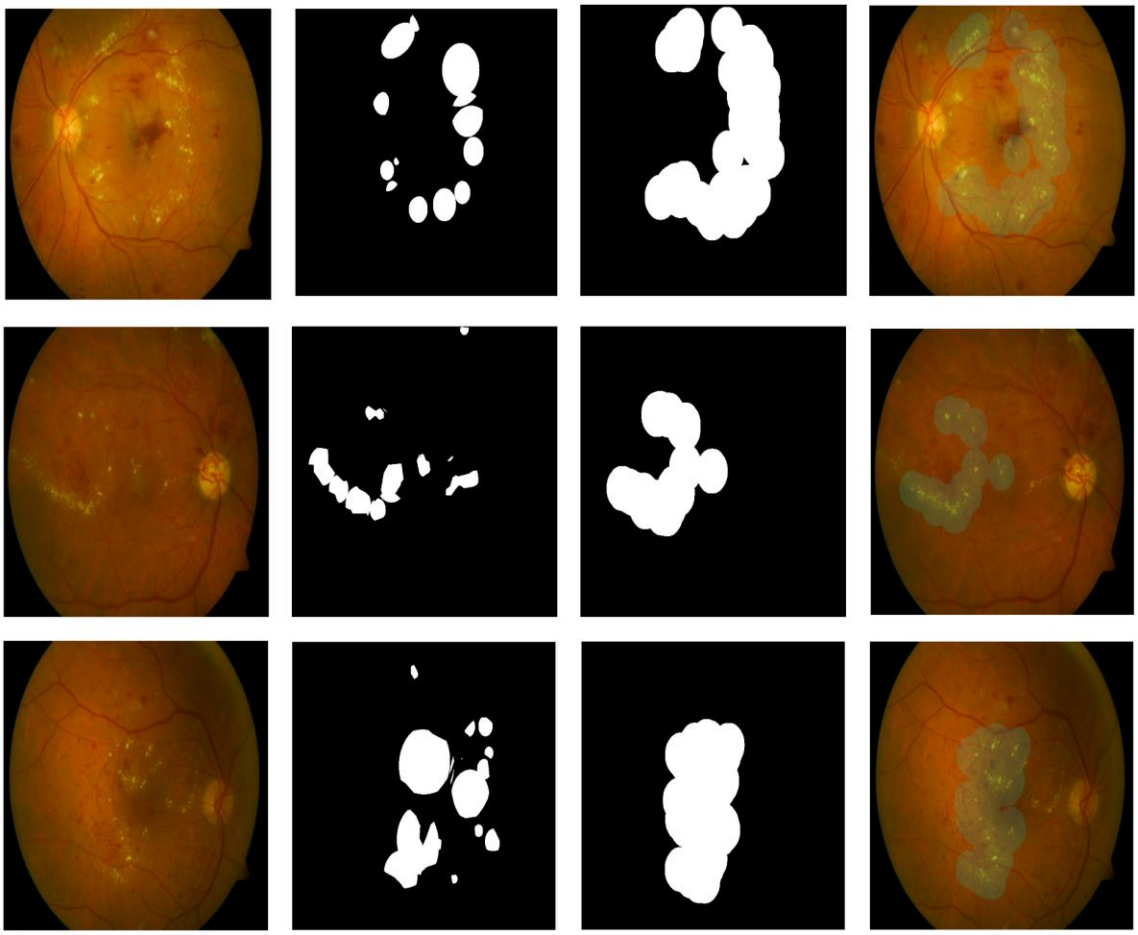

Figure 4.9 Typical sample of retinal exudates lesions segmentation results using DiaRetDB1 dataset. Column 1: Original retinal images. Column 2: Corresponding ground truths. Column 3: Exudates lesions segmentation results of our proposed system. Column 4: Superimposed.

The performance of exudates subsystem in extracting exudate lesions is evaluated using the same performance measures used in extraction of vasculature structures. Table 4.7 shows a comparative analysis of our proposed system with other existing schemes [35, 149-152]. All of these methods used the DiaRetDB1 dataset in their evaluations.

In case of exudates lesions segmentation, we use average sensitivity, average specificity and average accuracy as evaluation metrics, where we considered the extraction result as TP if the raw retina image contains exudate lesions according to both ground truth and our segmentation system.

we defined results as TN if the raw image does not contain exudates according to both the ground truth and our segmentation system. In contrast, a result was considered an FP if the raw image does not contain exudates according to the ground truth but our system extracts exudates from the image. The reverse case yielded FN results.

Table 4.7 Performance comparison of exudates lesions segmentation methods on pathological images of DIARETDB1 dataset

Method	Sensitivity	Specificity	Accuracy	PPV
†**Sopharak *et al* (2009) [151]**	97.2%	85.4%	85.6%	5.7%
Welfer *et al* (2010) [152]	70.48%	98.64%	-	21.32%
Harangi and Hajdu (2014) [150]	73%	-	-	69%
Liu *et al.* (2017) [35]	83%	75%	79%	-
Fraz *et al.* (2017) [149]	92.42%	81.25%	87.72%	87.14%
Proposed System	**75.80%**	**85.7%**	**83.4%**	**41.67%**

†This method used only 10 retinal images for sake of evaluation.

‡ PPV: Positive predictive value.

CHAPTER 5: CONCLUSIONS AND RECOMMENDATIONS

5.1 Conclusions

In this thesis, we have proposed a generic system for automatic detection, localization and extraction of three retinal anatomical structures using a hybrid of fuzzy set theory and morphological operations. From a clinical point of view, the extraction of retinal structures is the first step in the design and development of computer-assisted diagnostic systems for ophthalmic issues. The outputs of these proposed subsystems (vessels *detection subsystem*, *optic disc subsystem*, and *exudates lesions subsystem)* are integrated in a compact manner to capture the clinical information that they contain.

From a research point of view, our work makes two major contributions. First, our proposed system eliminates the need for designing a separate system for detecting each retinal anatomical structure; one compact novel system was used to extract three different anatomical structures with various features and textures. Building upon this system, a hybrid framework for performing detection and extraction tasks for other anatomical structures either inside the retina or other organs can be developed.

Second, the proposed system is highly robust and accurate as well, as it has been shown to perform better than the state-of-art on the public DRIVE, STARE, DRITSHTI-GS, and DiaRetDB1 retinal datasets. In addition, it performs well at extracting vessels and optic disc from pathological retinal images. Therefore, it can be considered ideal for real-life diagnosis applications.

Experimental results showed that for the same dataset used, our proposed system has achieved superior results in terms of specificity, sensitivity and accuracy. This is a clear indicator of the powerful system that can be yielded when a highly discriminative operator such as morphological operations combined in a hybrid manner with highly nondiscriminative ones such as fuzzy sets. This hybrid combination can be viewed as some sort of trade-off between the crisp world and the fuzzy one.

5.2 Future Work and Directions

There are improvements that can be done with regards to our proposed segmentation system. One is to investigate more retinal anatomical structures such as Fovea as normal one and other retinal anatomical structures such as Microaneuryms, Hemorrhage and soft exudate lesions as abnormal ones.

More investigation also can be added to the artificial intelligence part of our proposed system such as using Artificial Neural Networks (ANNs) to work in a scenario with tight time constraints. Although using parallel computing machines instead of using a single PC is one candidate solution for the issue of high needed computational time.

There are also directions of potential research that this thesis does not address. But it can be considered as a complementary part of a complete retinal computer aided system. This part is a content-based retinal retrieval system, where the outputs of this system integrates with the outputs of our system in such a way as to capture the complementary clinical information which they contain.

REFERENCES

[1] D. Purves, G. J. Augustine, D. Fitzpatrick, L. C. Katz, A.-S. LaMantia, J. O. McNamara, *et al.*, "Neuroscience," *Sunderland, MA: Sinauer Associates*, vol. 3, 2001.

[2] C. Wilkinson, F. L. Ferris, R. E. Klein, P. P. Lee, C. D. Agardh, M. Davis, *et al.*, "Proposed international clinical diabetic retinopathy and diabetic macular edema disease severity scales," *Ophthalmology*, vol. 110, pp. 1677-1682, 2003.

[3] J. B. Saaddine, A. A. Honeycutt, K. V. Narayan, X. Zhang, R. Klein, and J. P. Boyle, "Projection of diabetic retinopathy and other major eye diseases among people with diabetes mellitus: United States, 2005-2050," *Archives of ophthalmology*, vol. 126, pp. 1740-1747, 2008.

[4] P. H. Scanlon, C. Foy, R. Malhotra, and S. J. Aldington, "The influence of age, duration of diabetes, cataract, and pupil size on image quality in digital photographic retinal screening," *Diabetes Care*, vol. 28, pp. 2448-2453, 2005.

[5] M. S. Haleem, L. Han, J. van Hemert, B. Li, and A. Fleming, "Retinal area detector from Scanning Laser Ophthalmoscope (SLO) images for diagnosing retinal diseases," *IEEE journal of biomedical and health informatics*, vol. 19, pp. 1472-1482, 2015.

[6] N. Solouma, A.-B. M. Youssef, Y. Badr, and Y. M. Kadah, "Real-time retinal tracking for laser treatment planning and administration," in *Medical Imaging 2001*, 2001, pp. 1311-1321.

[7] Y. Wang and S. C. Lee, "A fast method for automated detection of blood vessels in retinal images," in *Signals, Systems & Computers, 1997. Conference Record of the Thirty-First Asilomar Conference on*, 1997, pp. 1700-1704.

[8] A. Can, H. Shen, J. N. Turner, H. L. Tanenbaum, and B. Roysam, "Rapid automated tracing and feature extraction from retinal fundus images using direct exploratory algorithms," *IEEE Transactions on information Technology in Biomedicine*, vol. 3, pp. 125-138, 1999.

[9] H. Li and O. Chutatape, "Fundus image features extraction," in *Engineering in Medicine and Biology Society, 2000. Proceedings of the 22nd Annual International Conference of the IEEE*, 2000, pp. 3071-3073.

[10] H. Kolb, "Simple Anatomy of the Retina," in *Webvision: The Organization of the Retina and Visual System*, H. Kolb, E. Fernandez, and R. Nelson, Eds., ed Salt Lake City (UT): University of Utah Health Sciences Center, 1995.

[11] M. D. Jonathan Trobe, University of Michigan Kellogg Eye Center, *http://kellogg.umich.edu/theeyeshaveit/optic-fundus/normal-disc.html*, 2009.

[12] M. Niemi and K. Winell, "Diabetes in Finland, prevalence and variation in quality of care," *Kirjapaino Hermes Oy, Tampre, Finland*, 2006.

[13] R. V. J. P. H. Kälviäinen and H. Uusitalo, "DIARETDB1 diabetic retinopathy database and evaluation protocol," *Medical Image Understanding and Analysis 2007*, p. 61, 2007.

[14] H. Kolb, "Simple anatomy of the retina," 2012.

[15] P. J. Saine and M. E. Tyler, *Ophthalmic photography: retinal photography, angiography, and electronic imaging* vol. 132: Butterworth-Heinemann Boston, 2002.

[16] *Ophthalmic Photographers' Society, Inc. Nixa, MO, USA [Online]. Available: https://www.opsweb.org/page/fundusimaging, Accessed on: Jun. 5, 2017.*

[17] E. Ng, U. R. Acharya, R. M. Rangayyan, and J. S. Suri, *Ophthalmological Imaging and Applications*: CRC Press, 2014.

[18] S. N. Patel, M. A. Klufas, M. C. Ryan, K. E. Jonas, S. Ostmo, M. A. Martinez-Castellanos, *et al.*, "Color Fundus Photography Versus Fluorescein Angiography in Identification of the Macular Center and Zone in Retinopathy of Prematurity," *American Journal of Ophthalmology*, vol. 159, pp. 950-957.e2, 2015.

[19] J. I. Orlando, E. Prokofyeva, and M. B. Blaschko, "A discriminatively trained fully connected conditional random field model for blood vessel segmentation in fundus images," *IEEE Transactions on Biomedical Engineering*, vol. 64, pp. 16-27, 2017.

[20] J. Zhang, B. Dashtbozorg, E. Bekkers, J. P. Pluim, R. Duits, and B. M. ter Haar Romeny, "Robust retinal vessel segmentation via locally adaptive derivative frames in orientation scores," *IEEE transactions on medical imaging*, vol. 35, pp. 2631-2644, 2016.

[21] S. Abbasi-Sureshjani, J. Zhang, R. Duits, and B. ter Haar Romeny, "Retrieving challenging vessel connections in retinal images by line co-occurrence statistics," *Biological Cybernetics*, pp. 1-11, 2017.

[22] S. Abbasi-Sureshjani, M. Favali, G. Citti, A. Sarti, and B. M. ter Haar Romeny, "Curvature integration in a 5D kernel for extracting vessel connections in retinal images," *IEEE Transactions on Image Processing*, vol. 27, pp. 606-621, 2018.

[23] L. Gu and L. Cheng, "Learning to boost filamentary structure segmentation," in *Proceedings of the IEEE International Conference on Computer Vision*, 2015, pp. 639-647.

[24] J. De, L. Cheng, X. Zhang, F. Lin, H. Li, K. H. Ong, *et al.*, "A graph-theoretical approach for tracing filamentary structures in neuronal and retinal images," *IEEE transactions on medical imaging*, vol. 35, pp. 257-272, 2016.

[25] K.-K. Maninis, J. Pont-Tuset, P. Arbeláez, and L. Van Gool, "Deep retinal image understanding," in *International Conference on Medical Image Computing and Computer-Assisted Intervention*, 2016, pp. 140-148.

[26] A. Sironi, V. Lepetit, and P. Fua, "Projection onto the manifold of elongated structures for accurate extraction," in *Proceedings of the IEEE International Conference on Computer Vision*, 2015, pp. 316-324.

[27] T. Kauppi, V. Kalesnykiene, J.-K. Kamarainen, L. Lensu, I. Sorri, A. Raninen, *et al.*, "The DIARETDB1 Diabetic Retinopathy Database and Evaluation Protocol," in *BMVC*, 2007, pp. 1-10.

[28] T. Walter, J.-C. Klein, P. Massin, and A. Erginay, "A contribution of image processing to the diagnosis of diabetic retinopathy-detection of exudates in color fundus images of the human retina," *IEEE transactions on medical imaging*, vol. 21, pp. 1236-1243, 2002.

[29] J. A. Hanley and B. J. McNeil, "The meaning and use of the area under a receiver operating characteristic (ROC) curve," *Radiology,* vol. 143, pp. 29-36, 1982.

[30] C. E. Metz, "Receiver operating characteristic analysis: a tool for the quantitative evaluation of observer performance and imaging systems," *Journal of the American College of Radiology,* vol. 3, pp. 413-422, 2006.

[31] J. Staal, M. D. Abràmoff, M. Niemeijer, M. A. Viergever, and B. Van Ginneken, "Ridge-based vessel segmentation in color images of the retina," *IEEE transactions on medical imaging,* vol. 23, pp. 501-509, 2004.

[32] M. Niemeijer, J. Staal, B. van Ginneken, M. Loog, and M. D. Abramoff, "Comparative study of retinal vessel segmentation methods on a new publicly available database," in *SPIE medical imaging*, 2004, pp. 648-656.

[33] A. Hoover, V. Kouznetsova, and M. Goldbaum, "Locating blood vessels in retinal images by piecewise threshold probing of a matched filter response," *IEEE Transactions on Medical imaging,* vol. 19, pp. 203-210, 2000.

[34] P. Bankhead, C. N. Scholfield, J. G. McGeown, and T. M. Curtis, "Fast retinal vessel detection and measurement using wavelets and edge location refinement, https://github.com/petebankhead/ARIA," *PloS one,* vol. 7, p. e32435, 2012.

[35] Q. Liu, B. Zou, J. Chen, W. Ke, K. Yue, Z. Chen, *et al.*, "A location-to-segmentation strategy for automatic exudate segmentation in colour retinal fundus images," *Computerized Medical Imaging and Graphics*, vol. 55, pp. 78-86, 2017.

[36] E. Decencière, X. Zhang, G. Cazuguel, B. Laÿ, B. Cochener, C. Trone, *et al.*, "Feedback on a publicly distributed image database: the Messidor database," *Image Analysis & Stereology,* vol. 33, pp. 231-234, 2014.

[37] J. Odstrcilik, R. Kolar, A. Budai, J. Hornegger, J. Jan, J. Gazarek, *et al.*, "Retinal vessel segmentation by improved matched filtering: evaluation on a new high-resolution fundus image database," *IET Image Processing*, vol. 7, pp. 373-383, 2013.

[38] L. Huiqi, W. Hsu, L. Mong Li, and W. Tien Yin, "Automatic grading of retinal vessel caliber," *IEEE Transactions on Biomedical Engineering*, vol. 52, pp. 1352-1355, 2005.

[39] H. Yu, S. Barriga, C. Agurto, S. Nemeth, W. Bauman, and P. Soliz, "Automated retinal vessel type classification in color fundus images," 2013, pp. 86700P-86700P-8.

[40] Z. Ma and H. Li, "Retinal vessel profiling based on four piecewise Gaussian model," in *2015 IEEE International Conference on Digital Signal Processing (DSP)*, 2015, pp. 1094-1097.

[41] S. Chaudhuri, S. Chatterjee, N. Katz, M. Nelson, and M. Goldbaum, "Detection of blood vessels in retinal images using two-dimensional matched filters," *IEEE Transactions on Medical Imaging*, vol. 8, pp. 263-269, 1989.

[42] N. P. Singh and R. Srivastava, "Retinal blood vessels segmentation by using Gumbel probability distribution function based matched filter," *Computer methods and programs in biomedicine*, vol. 129, pp. 40-50, 2016.

[43] N. P. Singh, R. Kumar, and R. Srivastava, "Local entropy thresholding based fast retinal vessels segmentation by modifying matched filter," in *International Conference on Computing, Communication & Automation*, 2015, pp. 1166-1170.

[44] T. Zhu and G. Schaefer, "Retinal vessel extraction using a piecewise Gaussian scaled model," in *2011 Annual International Conference of the IEEE Engineering in Medicine and Biology Society*, 2011, pp. 5008-5011.

[45] T. Zhu, "Fourier cross-sectional profile for vessel detection on retinal images," *Computerized Medical Imaging and Graphics*, vol. 34, pp. 203-212, 2010.

[46] F. M. Villalobos-Castaldi, E. M. Felipe-Riverón, and L. P. Sánchez-Fernández, "A fast, efficient and automated method to extract vessels from fundus images," *Journal of Visualization*, vol. 13, pp. 263-270, 2010.

[47] A. A. Lenskiy and J. S. Lee, "Rugged terrain segmentation based on salient features," in *ICCAS 2010*, 2010, pp. 1737-1740.

[48] T. Chanwimaluang and G. Fan, "An efficient algorithm for extraction of anatomical structures in retinal images," in *Proceedings 2003 International Conference on Image Processing (Cat. No.03CH37429)*, 2003, pp. I-1093-6 vol.1.

[49] M. Al-Rawi, M. Qutaishat, and M. Arrar, "An improved matched filter for blood vessel detection of digital retinal images," *Computers in Biology and Medicine*, vol. 37, pp. 262-267, 2007.

[50] J. Kaur and H. Sinha, "Automated detection of retinal blood vessels in diabetic retinopathy using Gabor filter," *International Journal of Computer Science and Network Security (IJCSNS)*, vol. 12, p. 109, 2012.

[51] B. Zhang, L. Zhang, L. Zhang, and F. Karray, "Retinal vessel extraction by matched filter with first-order derivative of Gaussian," *Computers in biology and medicine*, vol. 40, pp. 438-445, 2010.

[52] H. Zolfagharnasab and A. R. Naghsh-Nilchi, "Cauchy Based Matched Filter for Retinal Vessels Detection," *Journal of Medical Signals and Sensors*, vol. 4, pp. 1-9,10/23/2014.

[53] D. Kumar, A. Pramanik, S. S. Kar, and S. P. Maity, "Retinal blood vessel segmentation using matched filter and laplacian of gaussian," in *Signal Processing and Communications (SPCOM), 2016 International Conference on*, 2016, pp. 1-5.

[54] S. Roychowdhury, D. D. Koozekanani, S. N. Kuchinka, and K. K. Parhi, "Optic disc boundary and vessel origin segmentation of fundus images," *IEEE journal of biomedical and health informatics*, vol. 20, pp. 1562-1574, 2016.

[55] O. Chutatape, Z. Liu, and S. M. Krishnan, "Retinal blood vessel detection and tracking by matched Gaussian and Kalman filters," in *Proceedings of the 20th Annual International Conference of the IEEE Engineering in Medicine and Biology Society. Vol.20 Biomedical Engineering Towards the Year 2000 and Beyond (Cat. No.98CH36286)*, 1998, pp. 3144-3149 vol.6.

[56] H. Li, J. Zhang, Q. Nie, and L. Cheng, "A retinal vessel tracking method based on bayesian theory," in *Industrial Electronics and Applications (ICIEA), 2013 8th IEEE Conference on*, 2013, pp. 232-235.

[57] C. H. Wu, G. Agam, and P. Stanchev, "A general framework for vessel segmentation in retinal images," in *2007 International Symposium on Computational Intelligence in Robotics and Automation*, 2007, pp. 37-42.

[58] M. Sofka and C. V. Stewart, "Retinal Vessel Centerline Extraction Using Multiscale Matched Filters, Confidence and Edge Measures," *IEEE Transactions on Medical Imaging*, vol. 25, pp. 1531-1546, 2006.

[59] T. Yedidya and R. Hartley, "Tracking of Blood Vessels in Retinal Images Using Kalman Filter," in *2008 Digital Image Computing: Techniques and Applications*, 2008, pp. 52-58.

[60] Y. Yin, M. Adel, M. Guillaume, and S. Bourennane, "A probabilistic based method for tracking vessels in retinal images," in *2010 IEEE International Conference on Image Processing*, 2010, pp. 4081-4084.

[61] M. Adel, M. Rasigni, T. Gaidon, C. Fossati, and S. Bourennane, "Statistical-based linear vessel structure detection in medical images," in *2009 16th IEEE International Conference on Image Processing (ICIP)*, 2009, pp. 649-652.

[62] A. Kundu and R. K. Chatterjee, "Retinal vessel segmentation using Morphological Angular Scale-Space," in *2012 Third International Conference on Emerging Applications of Information Technology*, 2012, pp. 316-319.

[63] N. M. Salem and A. K. Nandi, "Unsupervised Segmentation of Retinal Blood Vessels Using a Single Parameter Vesselness Measure," in *2008 Sixth Indian Conference on Computer Vision, Graphics & Image Processing*, 2008, pp. 528-534.

[64] J. B. Roerdink and A. Meijster, "The watershed transform: Definitions, algorithms and parallelization strategies," *Fundamenta informaticae*, vol. 41, pp. 187-228, 2000.

[65] J. Serra, *Image analysis and mathematical morphology, v. 1*: Academic press, 1982.

[66] M. Frucci, D. Riccio, G. S. d. Baja, and L. Serino, "Using Contrast and Directional Information for Retinal Vessels Segmentation," in *2014 Tenth International Conference on Signal-Image Technology and Internet-Based Systems*, 2014, pp. 592-597.

[67] Z. Jiang, J. Yepez, S. An, and S. Ko, "Fast, accurate and robust retinal vessel segmentation system," *Biocybernetics and Biomedical Engineering,* vol. 37, pp. 412-421, 2017.

[68] T. Lindeberg, "Scale-space theory: A basic tool for analyzing structures at different scales," *Journal of applied statistics,* vol. 21, pp. 225-270, 1994.

[69] J. Babaud, A. P. Witkin, M. Baudin, and R. O. Duda, "Uniqueness of the Gaussian Kernel for Scale-Space Filtering," *IEEE Transactions on Pattern Analysis and Machine Intelligence,* vol. PAMI-8, pp. 26-33, 1986.

[70] T. Lindeberg, *Scale-space theory in computer vision* vol. 256: Springer Science & Business Media, 2013.

[71] P. Burt and E. Adelson, "The Laplacian Pyramid as a Compact Image Code," *IEEE Transactions on Communications,* vol. 31, pp. 532-540, 1983.

[72] J. L. Crowley and A. C. Parker, "A Representation for Shape Based on Peaks and Ridges in the Difference of Low-Pass Transform," *IEEE Transactions on Pattern Analysis and Machine Intelligence,* vol. PAMI-6, pp. 156-170, 1984.

[73] A. Klinger, "Patterns and search statistics," *Optimizing methods in statistics,* vol. 3, pp. 303-337, 1971.

[74] O. Tankyevych, H. Talbot, and P. Dokladal, "Curvilinear morpho-Hessian filter," in *2008 5th IEEE International Symposium on Biomedical Imaging: From Nano to Macro*, 2008, pp. 1011-1014.

[75] A. F. Frangi, W. J. Niessen, K. L. Vincken, and M. A. Viergever, "Multiscale vessel enhancement filtering," in *International Conference on Medical Image Computing and Computer-Assisted Intervention*, 1998, pp. 130-137.

[76] A. Budai, G. Michelson, and J. Hornegger, "Multiscale Blood Vessel Segmentation in Retinal Fundus Images," in *Bildverarbeitung für die Medizin*, 2010, pp. 261-265.

[77] M. B. Abdallah, J. Malek, K. Krissian, and R. Tourki, "An automated vessel segmentation of retinal images using multiscale vesselness," in *Eighth International Multi-Conference on Systems, Signals & Devices*, 2011, pp. 1-6.

[78] S. Rattathanapad, P. Mittrapiyanuruk, P. Kaewtrakulpong, B. Uyyanonvara, and C. Sinthanayothin, "Vessel extraction in retinal images using multilevel line detection," in *Proceedings of 2012 IEEE-EMBS International Conference on Biomedical and Health Informatics*, 2012, pp. 345-349.

[79] E. Moghimirad, S. H. Rezatofighi, and H. Soltanian-Zadeh, "Multi-scale approach for retinal vessel segmentation using medialness function," in *2010 IEEE International Symposium on Biomedical Imaging: From Nano to Macro*, 2010, pp. 29-32.

[80] T. Albrecht, M. Lüthi, and T. Vetter, "Deformable models," *Encyclopedia of Biometrics*, pp. 337-343, 2015.

[81] T. McInerney and D. Terzopoulos, "Deformable models in medical image analysis: a survey," *Medical Image Analysis*, vol. 1, pp. 91-108, 1996/06/01 1996.

[82] V. Caselles, R. Kimmel, and G. Sapiro, "Geodesic active contours," *International journal of computer vision*, vol. 22, pp. 61-79, 1997.

[83] Z. Jin, T. Zhaohui, G. Weihua, and L. Jinping, "Retinal vessel image segmentation based on correlational open active contours model," in *2015 Chinese Automation Congress (CAC)*, 2015, pp. 993-998.

[84] Y. Zhao, L. Rada, K. Chen, S. P. Harding, and Y. Zheng, "Automated Vessel Segmentation Using Infinite Perimeter Active Contour Model with Hybrid Region Information with Application to Retinal Images," *IEEE Transactions on Medical Imaging*, vol. 34, pp. 1797-1807, 2015.

[85] J. A. Sethian, "Analysis of flame propagation,"; Lawrence Berkeley Lab., CA (USA),PhD. Dissertation LBL-14125; Other: ON: DE82018582 United States Other: ON: DE82018582 NTIS, PC A07/MF A01. LBNL English, 1982.

[86] J. A. Sethian, "Curvature and the evolution of fronts," *Communications in Mathematical Physics*, vol. 101, pp. 487-499, 1985.

[87] H. Gongt, Y. Li, G. Liu, W. Wu, and G. Chen, "A level set method for retina image vessel segmentation based on the local cluster value via bias correction," in *2015 8th International Congress on Image and Signal Processing (CISP)*, 2015, pp. 413-417.

[88] B. Dizdaro, E. Ataer-Cansizoglu, J. Kalpathy-Cramer, K. Keck, M. F. Chiang, and D. Erdogmus, "Level sets for retinal vasculature segmentation using seeds from ridges and edges from phase maps," in *2012 IEEE International Workshop on Machine Learning for Signal Processing*, 2012, pp. 1-6.

[89] A. Christodoulidis, T. Hurtut, H. B. Tahar, and F. Cheriet, "A multi-scale tensor voting approach for small retinal vessel segmentation in high resolution fundus images," *Computerized Medical Imaging and Graphics*, vol. 52, pp. 28-43, 2016.

[90] M. Niemeijer, J. Staal, B. van Ginneken, M. Loog, and M. D. Abramoff, "Comparative study of retinal vessel segmentation methods on a new publicly available database," in *Medical Imaging 2004*, pp. 648-656.

[91] M. Foracchia, E. Grisan, and A. Ruggeri, "Luminosity and contrast normalization in retinal images," *Medical Image Analysis,* vol. 9, pp. 179-190, 2005.

[92] N. Kingsbury, "The dual-tree complex wavelet transform: A new efficient tool for image restoration and enhancement," in *9th European Signal Processing Conference (EUSIPCO 1998),* 1998, pp. 1-4.

[93] U. T. V. Nguyen, A. Bhuiyan, L. A. F. Park, and K. Ramamohanarao, "An effective retinal blood vessel segmentation method using multi-scale line detection," *Pattern Recognition,* vol. 46, pp. 703-715, 2013.

[94] G. van Antwerpen, P. Verbeek, and F. Groen, "Automatic counting of asbestos fibres," *Signal Processing III: theories and applications,* pp. 891-896, 1986.

[95] G. Medioni, M.-S. Lee, and C.-K. Tang, *A computational framework for segmentation and grouping*: Elsevier, 2000.

[96] G. Medioni and S. B. Kang, *Emerging topics in computer vision*: Prentice Hall PTR, 2004.

[97] M. U. Akram, A. Tariq, and S. A. Khan, "Retinal image blood vessel segmentation," in *2009 International Conference on Information and Communication Technologies,* 2009, pp. 181-192.

[98] A. Arneodo, N. Decoster, and S. Roux, "A wavelet-based method for multifractal image analysis. I. Methodology and test applications on isotropic and anisotropic random rough surfaces," *The European Physical Journal B-Condensed Matter and Complex Systems,* vol. 15, pp. 567-600, 2000.

[99] X. Jiang and D. Mojon, "Adaptive local thresholding by verification-based multithreshold probing with application to vessel detection in retinal images," *IEEE*

Transactions on Pattern Analysis and Machine Intelligence, vol. 25, pp. 131-137, 2003.

[100] A. Sharma, M. Agrawal, and B. Lall, "Optic Disc Detection Using Vessel Characteristics and Disc Features," in *Communications (NCC), 2017 Twenty-third National Conference on*, 2017, pp. 1-6.

[101] C. M. Bishop, *Pattern Recognition and Machine Learning (Information Science and Statistics)*: Springer-Verlag New York, Inc., 2006.

[102] J. Liu, J. Sun, and S. Wang, "Pattern recognition: An overview," *IJCSNS International Journal of Computer Science and Network Security,* vol. 6, pp. 57-61, 2006.

[103] G. Skolidis, "Transfer learning with Gaussian processes," *PhD Dissertation,The University of Edinburgh,* 2012.

[104] M. J. Kochenderfer, "Adaptive Modelling and Planning for Learning Intelligent Behaviour," *PhD Dissertation,The University of Edinburgh,* 2006.

[105] R. Nekovei and S. Ying, "Back-propagation network and its configuration for blood vessel detection in angiograms," *IEEE Transactions on Neural Networks,* vol. 6, pp. 64-72, 1995.

[106] S. J. Pan and Q. Yang, "A Survey on Transfer Learning," *IEEE Transactions on Knowledge and Data Engineering,* vol. 22, pp. 1345-1359, 2010.

[107] A. G. Roy and D. Sheet, "DASA: Domain Adaptation in Stacked Autoencoders using Systematic Dropout," *arXiv preprint arXiv:1603.06060,* 2016.

[108] D. Maji, A. Santara, S. Ghosh, D. Sheet, and P. Mitra, "Deep neural network and random forest hybrid architecture for learning to detect retinal vessels in fundus

images," in *2015 37th Annual International Conference of the IEEE Engineering in Medicine and Biology Society (EMBC)*, 2015, pp. 3029-3032.

[109] A. Lahiri, A. G. Roy, D. Sheet, and P. K. Biswas, "Deep neural ensemble for retinal vessel segmentation in fundus images towards achieving label-free angiography," in *2016 38th Annual International Conference of the IEEE Engineering in Medicine and Biology Society (EMBC)*, 2016, pp. 1340-1343.

[110] D. Maji, A. Santara, P. Mitra, and D. Sheet, "Ensemble of deep convolutional neural networks for learning to detect retinal vessels in fundus images," *arXiv preprint arXiv:1603.04833*, 2016.

[111] P. Liskowski and K. Krawiec, "Segmenting Retinal Blood Vessels With Deep Neural Networks," *IEEE Transactions on Medical Imaging*, vol. 35, pp. 2369-2380, 2016.

[112] A. Dasgupta and S. Singh, "A Fully Convolutional Neural Network based Structured Prediction Approach Towards the Retinal Vessel Segmentation," *arXiv preprint arXiv:1611.02064*, 2016.

[113] S. A. Salem, N. M. Salem, and A. K. Nandi, "Segmentation of retinal blood vessels using a novel clustering algorithm," in *Signal Processing Conference, 2006 14th European*, 2006, pp. 1-5.

[114] S. Sharma and E. V. Wasson, "Retinal Blood Vessel Segmentation Using Fuzzy Logic," *Journal of Network Communications and Emerging Technologies (JNCET) www. jncet. org*, vol. 4, 2015.

[115] R. Akhavan and K. Faez, "A Novel Retinal Blood Vessel Segmentation Algorithm using Fuzzy segmentation," *International Journal of Electrical and Computer Engineering,* vol. 4, p. 561, 2014.

[116] S. Xie and H. Nie, "Retinal vascular image segmentation using genetic algorithm Plus FCM clustering," in *Intelligent System Design and Engineering Applications (ISDEA), 2013 Third International Conference on*, 2013, pp. 1225-1228.

[117] E. Emary, H. M. Zawbaa, A. E. Hassanien, G. Schaefer, and A. T. Azar, "Retinal vessel segmentation based on possibilistic fuzzy c-means clustering optimised with cuckoo search," in *Neural Networks (IJCNN), 2014 International Joint Conference on*, 2014, pp. 1792-1796.

[118] R. Krishnapuram and J. M. Keller, "A possibilistic approach to clustering," *IEEE transactions on fuzzy systems,* vol. 1, pp. 98-110, 1993.

[119] N. R. Pal, K. Pal, J. M. Keller, and J. C. Bezdek, "A possibilistic fuzzy c-means clustering algorithm," *IEEE transactions on fuzzy systems,* vol. 13, pp. 517-530, 2005.

[120] V. R. Bhargavi, R. K. Senapati, G. Methra, and S. Kandanulu, "Research Article Bright Lesion Detection in Color Fundus Images Based on Texture Features," 2016.

[121] M. Sezgin, "Survey over image thresholding techniques and quantitative performance evaluation," *Journal of Electronic imaging,* vol. 13, pp. 146-168, 2004.

[122] F. Zana and J.-C. Klein, "A multimodal registration algorithm of eye fundus images using vessels detection and Hough transform," *IEEE transactions on Medical Imaging,* vol. 18, pp. 419-428, 1999.

[123] C. Heneghan, J. Flynn, M. O'Keefe, and M. Cahill, "Characterization of changes in blood vessel width and tortuosity in retinopathy of prematurity using image analysis," *Medical image analysis,* vol. 6, pp. 407-429, 2002.

[124] E. J. Carmona, M. Rincón, J. García-Feijoó, and J. M. Martínez-de-la-Casa, "Identification of the optic nerve head with genetic algorithms," *Artificial Intelligence in Medicine,* vol. 43, pp. 243-259, 2008.

[125] J. B. Jonas, W. M. Budde, and S. Panda-Jonas, "Ophthalmoscopic evaluation of the optic nerve head," *Survey of ophthalmology,* vol. 43, pp. 293-320, 1999.

[126] S. Aja-Fernández, A. H. Curiale, and G. Vegas-Sánchez-Ferrero, "A local fuzzy thresholding methodology for multiregion image segmentation," *Knowledge-Based Systems,* vol. 83, pp. 1-12, 2015.

[127] L. Szilagyi, Z. Benyo, S. M. Szilágyi, and H. Adam, "MR brain image segmentation using an enhanced fuzzy c-means algorithm," in *Engineering in Medicine and Biology Society, 2003. Proceedings of the 25th Annual International Conference of the IEEE*, 2003, pp. 724-726.

[128] A.-M. Šimundić, "Measures of diagnostic accuracy: basic definitions," *EJIFCC,* vol. 19, p. 203, 2009.

[129] W. Zhu, N. Zeng, and N. Wang, "Sensitivity, specificity, accuracy, associated confidence interval and ROC analysis with practical SAS implementations," *NESUG proceedings: health care and life sciences, Baltimore, Maryland,* vol. 19, 2010.

[130] J. Zhang, Z. Tang, W. Gui, and J. Liu, "Retinal vessel image segmentation based on correlational open active contours model," in *Chinese Automation Congress (CAC), 2015*, 2015, pp. 993-998.

[131] R. GeethaRamani and L. Balasubramanian, "Retinal blood vessel segmentation employing image processing and data mining techniques for computerized retinal image analysis," *Biocybernetics and Biomedical Engineering*, vol. 36, pp. 102-118, 2016.

[132] V. R. P. Borges, D. J. d. Santos, B. Popovic, and D. F. Cordeiro, "Segmentation of Blood Vessels in Retinal Images Based on Nonlinear Filtering," in *2015 IEEE 28th International Symposium on Computer-Based Medical Systems*, 2015, pp. 95-96.

[133] T. Mapayi and J.-R. Tapamo, "Difference image and fuzzy c-means for detection of retinal vessels," in *Image Analysis and Interpretation (SSIAI), 2016 IEEE Southwest Symposium on*, 2016, pp. 169-172.

[134] G. B. Kande, P. V. Subbaiah, and T. S. Savithri, "Segmentation of exudates and optic disk in retinal images," in *Computer Vision, Graphics & Image Processing, 2008. ICVGIP'08. Sixth Indian Conference on*, 2008, pp. 535-542.

[135] Y. Zhang, W. Hsu, and M. L. Lee, "Detection of retinal blood vessels based on nonlinear projections," *Journal of Signal Processing Systems*, vol. 55, pp. 103-112, 2009.

[136] B. Yin, H. Li, B. Sheng, X. Hou, Y. Chen, W. Wu, *et al.*, "Vessel extraction from non-fluorescein fundus images using orientation-aware detector," *Medical image analysis*, vol. 26, pp. 232-242, 2015.

[137] L. Zhang, M. Fisher, and W. Wang, "Retinal vessel segmentation using multi-scale textons derived from keypoints," *Computerized Medical Imaging and Graphics*, vol. 45, pp. 47-56, 2015.

[138] B. Dizdaro, E. Ataer-Cansizoglu, J. Kalpathy-Cramer, K. Keck, M. F. Chiang, and D. Erdogmus, "Level sets for retinal vasculature segmentation using seeds from ridges and edges from phase maps," in *Machine Learning for Signal Processing (MLSP), 2012 IEEE International Workshop on*, 2012, pp. 1-6.

[139] J. Sivaswamy, S. Krishnadas, G. D. Joshi, M. Jain, and A. U. S. Tabish, "Drishti-gs: Retinal image dataset for optic nerve head (onh) segmentation," in *Biomedical Imaging (ISBI), 2014 IEEE 11th International Symposium on*, 2014, pp. 53-56.

[140] A. Hoover and M. Goldbaum, "Locating the optic nerve in a retinal image using the fuzzy convergence of the blood vessels," *IEEE transactions on medical imaging*, vol. 22, pp. 951-958, 2003.

[141] J. Cheng, J. Liu, Y. Xu, F. Yin, D. W. K. Wong, N.-M. Tan, *et al.*, "Superpixel classification based optic disc and optic cup segmentation for glaucoma screening," *IEEE Transactions on Medical Imaging*, vol. 32, pp. 1019-1032, 2013.

[142] S. Sedai, P. K. Roy, D. Mahapatra, and R. Garnavi, "Segmentation of optic disc and optic cup in retinal fundus images using shape regression," in *Engineering in Medicine and Biology Society (EMBC), 2016 IEEE 38th Annual International Conference of the*, 2016, pp. 3260-3264.

[143] D. Wong, J. Liu, J. Lim, X. Jia, F. Yin, H. Li, *et al.*, "Level-set based automatic cup-to-disc ratio determination using retinal fundus images in ARGALI," in *Engineering in Medicine and Biology Society, 2008. EMBS 2008. 30th Annual International Conference of the IEEE*, 2008, pp. 2266-2269.

[144] J. Zilly, J. M. Buhmann, and D. Mahapatra, " Glaucoma detection using entropy sampling and ensemble learning for automatic optic cup and

disc segmentation," *Computerized Medical Imaging and Graphics,* vol. 55, pp. 28-41, 2017.

[145] S. Bharkad, "Automatic segmentation of optic disk in retinal images," *Biomedical Signal Processing and Control,* vol. 31, pp. 483-498, 2017.

[146] C. A. Lupascu, D. Tegolo, and L. Di Rosa, "Automated detection of optic disc location in retinal images," in *Computer-Based Medical Systems, 2008. CBMS'08. 21st IEEE International Symposium on*, 2008, pp. 17-22.

[147] J. Seo, K. Kim, J. Kim, K. Park, and H. Chung, "Measurement of ocular torsion using digital fundus image," in *Engineering in Medicine and Biology Society, 2004. IEMBS'04. 26th Annual International Conference of the IEEE*, 2004, pp. 1711-1713.

[148] K. Stapor, A. Świtonski, R. Chrastek, and G. Michelson, "Segmentation of fundus eye images using methods of mathematical morphology for glaucoma diagnosis," *Computational Science-ICCS 2004,* pp. 41-48, 2004.

[149] M. M. Fraz, W. Jahangir, S. Zahid, M. M. Hamayun, and S. A. Barman, "Multiscale segmentation of exudates in retinal images using contextual cues and ensemble classification," *Biomedical Signal Processing and Control,* vol. 35, pp. 50-62, 2017.

[150] B. Harangi and A. Hajdu, "Automatic exudate detection by fusing multiple active contours and regionwise classification," *Computers in biology and medicine,* vol. 54, pp. 156-171, 2014.

[151] A. Sopharak, B. Uyyanonvara, and S. Barman, "Automatic exudate detection from non-dilated diabetic retinopathy retinal images using fuzzy c-means clustering," *Sensors,* vol. 9, pp. 2148-2161, 2009.

[152] D. Welfer, J. Scharcanski, and D. R. Marinho, "A coarse-to-fine strategy for automatically detecting exudates in color eye fundus images," *Computerized Medical Imaging and Graphics*, vol. 34, pp. 228-235, 2010.